Supporting Information

A Comprehensive Experimental and Simulation Study of Ignition Delay Time Characteristics of Single Fuel C_1–C_2 Hydrocarbons Over a Wide Range of Temperature, Pressure, Equivalence ratio, and Dilution

Mohammadreza Baigmohammadi[a,*], Vaibhav Patel[a], Sergio Martinez[a], Snehasish Panigaphy[a], Ajoy Ramalingam[b], Ultan Burke[a], Kieran P. Somers[a], Karl A. Heufer[b], Andrzej Pekalski[c], Henry J. Curran[a]

[a] Combustion Chemistry Centre, School of Chemistry, Ryan Institute, National University of Ireland Galway, University Road, Galway, H91 TK33, Ireland

[b] Physico-Chemical Fundamentals of Combustion, RWTH Aachen University, Germany

[c] Shell Research Limited, Shell Centre London, London SE1 7NA, United Kingdom

**** Corresponding author: mohammadreza.baigmohammadi@nuigalway.ie***

Table of Contents

Supporting Information

Table of Figures

Table of Tables

1 Motivation for taking new experimental data

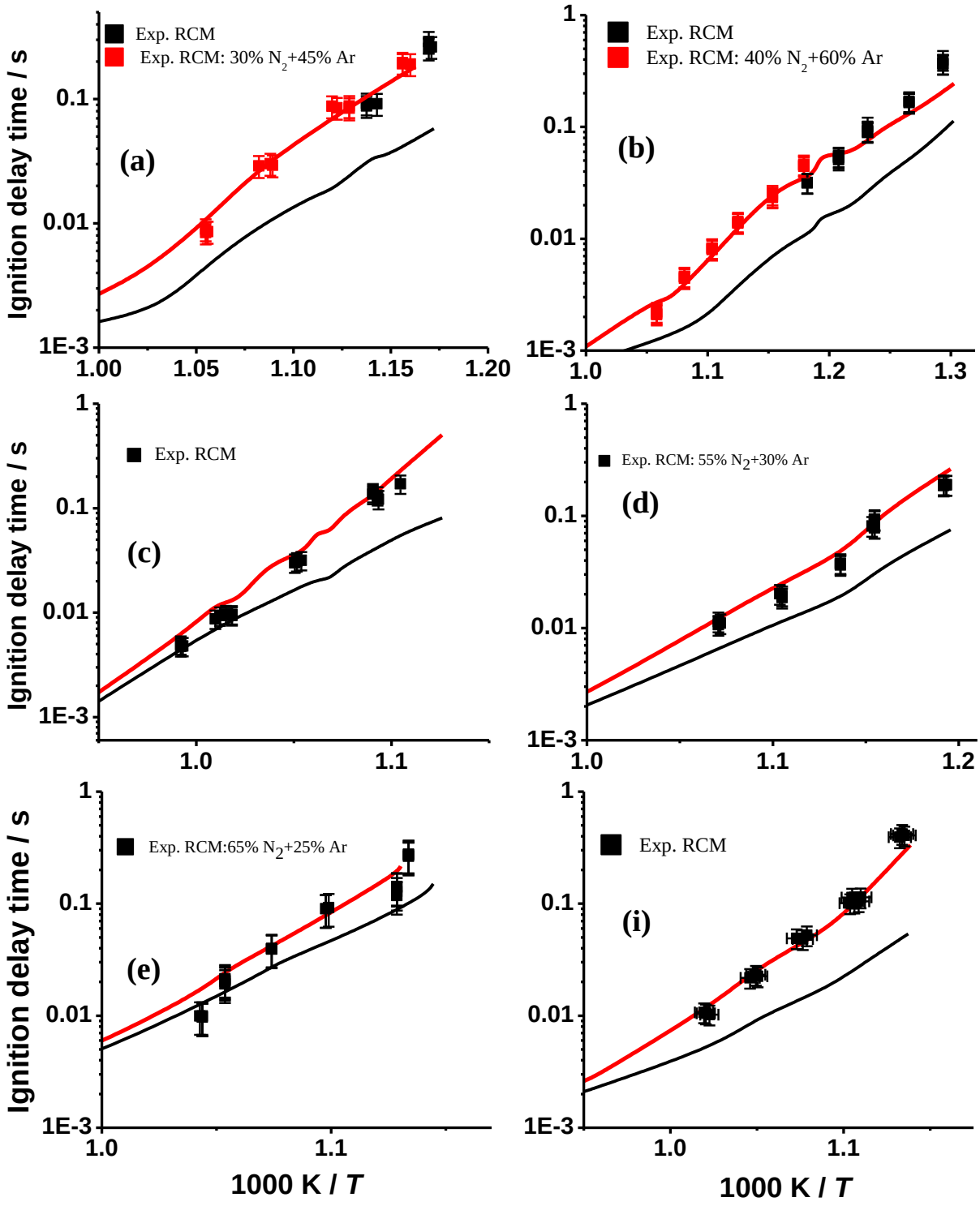

Figure S1. Experimental and simulated data of ethylene's IDT values at: (a) 6.25% C_2H_4, 18.75% O_2, (φ = 1.0) and 75.0% N_2, $\bar{p}_c$ = 20 bar; (b) 10% C_2H_4, 15% O_2, (φ = 2.0) and 75.0% N_2, $\bar{p}_c$ = 40 bar; (c) 2.142% C_2H_4, 12.857% O_2, (φ = 0.5) in 37% Ar + 48.0% N_2, $\bar{p}_c$ = 20 bar; (d) 3.75% C_2H_4, 11.25% O_2, (φ = 1.0) in 10% Ar + 75.0% N_2, $\bar{p}_c$ = 40 bar; (e) 1.43% C_2H_4, 8.57% O_2, (φ = 0.5) in 15% Ar + 75.0% N_2, $\bar{p}_c$ = 40 bar; (f) 4% C_2H_4, 6% O_2, (φ = 2.0) in 45% Ar + 45% N_2, $\bar{p}_c$ = 20 bar; the red lines: NUIGMech0.9, the black line: AramcoMech 3.0.

2 Performance of the other kinetic models

Table S1. Applied chemical mechanisms in the study.

No	*Mechanism*	*Number of reactions*	*Number of species*	*Comments*
1	AramcoMech 3.0 [1]	3037	581	Released at 2018
2	AramcoMech 2.0 [2-8]	2716	493	Released at 2016
3	AramcoMech 1.3 [7]	1542	253	Released at 2013
4	CRECK[9]	1941	114	Released at 2020
5	UCSD [10]	268	57	Released at 2016
6	GRI 3.0 [11]	325	53	Released at 2000
7	FFCM–1 (C1–C2) [12]	291	38	C_1–C_2; Low temperature reactions are not included; released at 2016

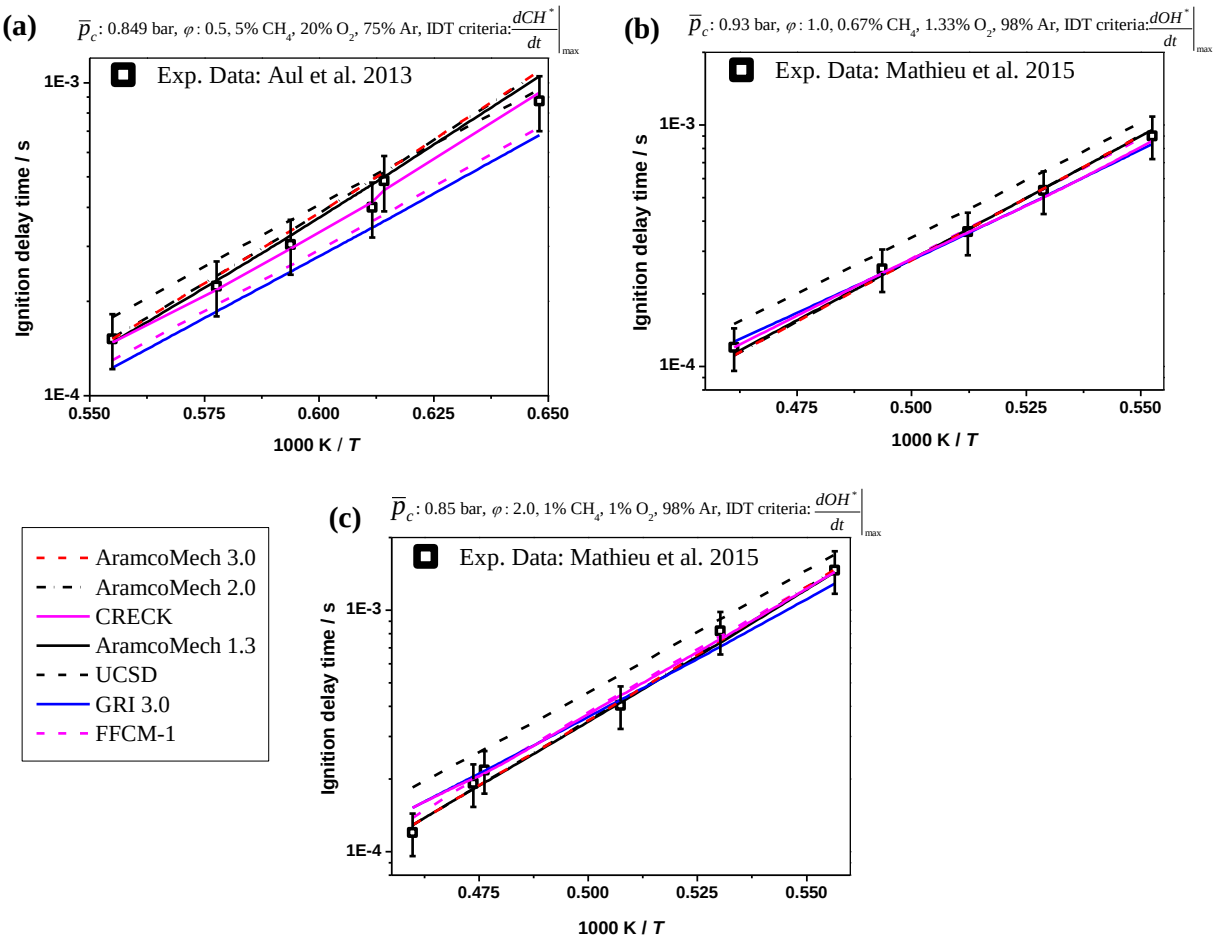

Figure S2. Available experimental and simulation data of methane's IDT values for average compressed reactive mixture pressure (p_c): (a) P1C1; (b) P1C8; (c) P1C6. The CH* species is not included in CRECK, UCSD, and GRI 3.0 mechanisms, CH results are presented instead of CH*.

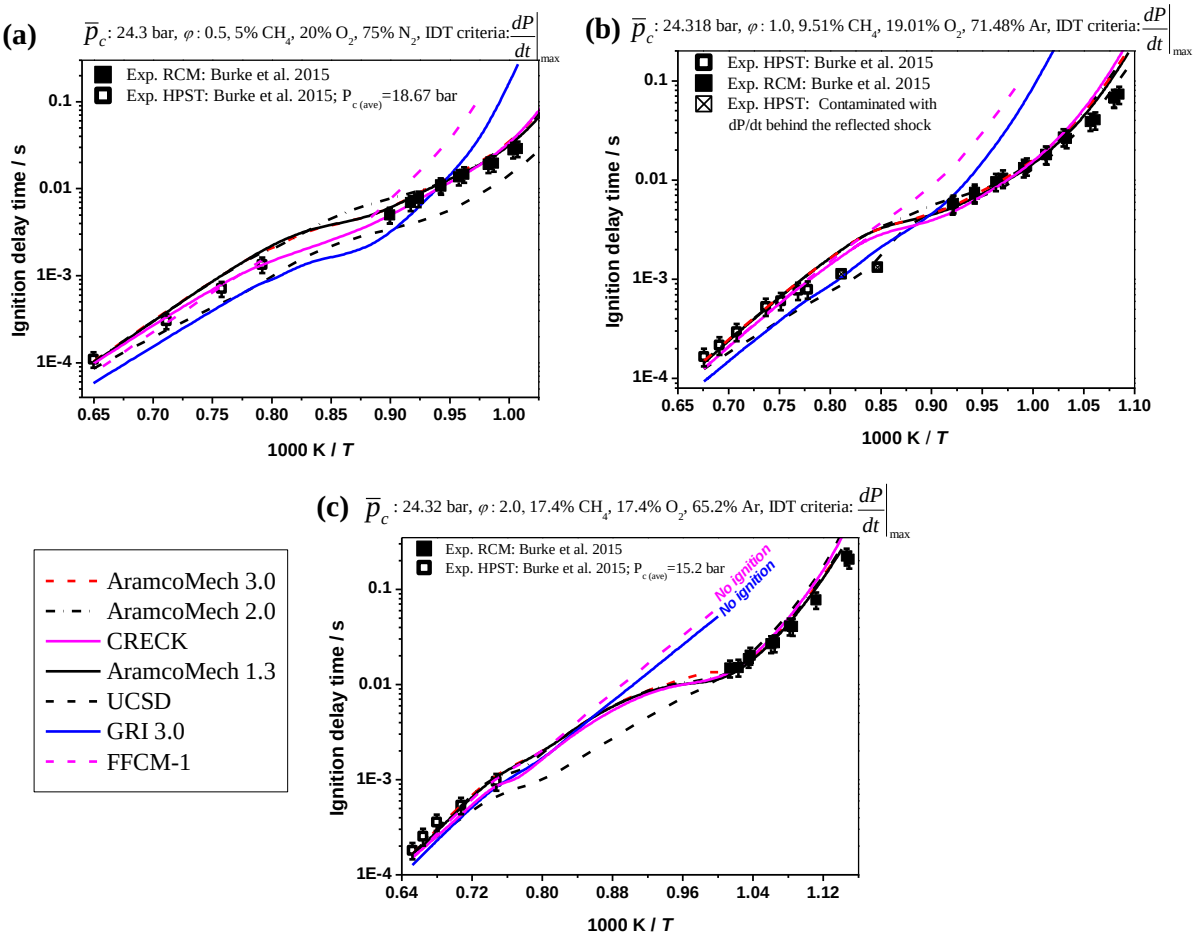

Figure S3. Experimental and simulation data of methane's IDT values for average compressed reactive mixture pressure (p_c): (a) P1C4; (b) P1C2; (c) P1C9.

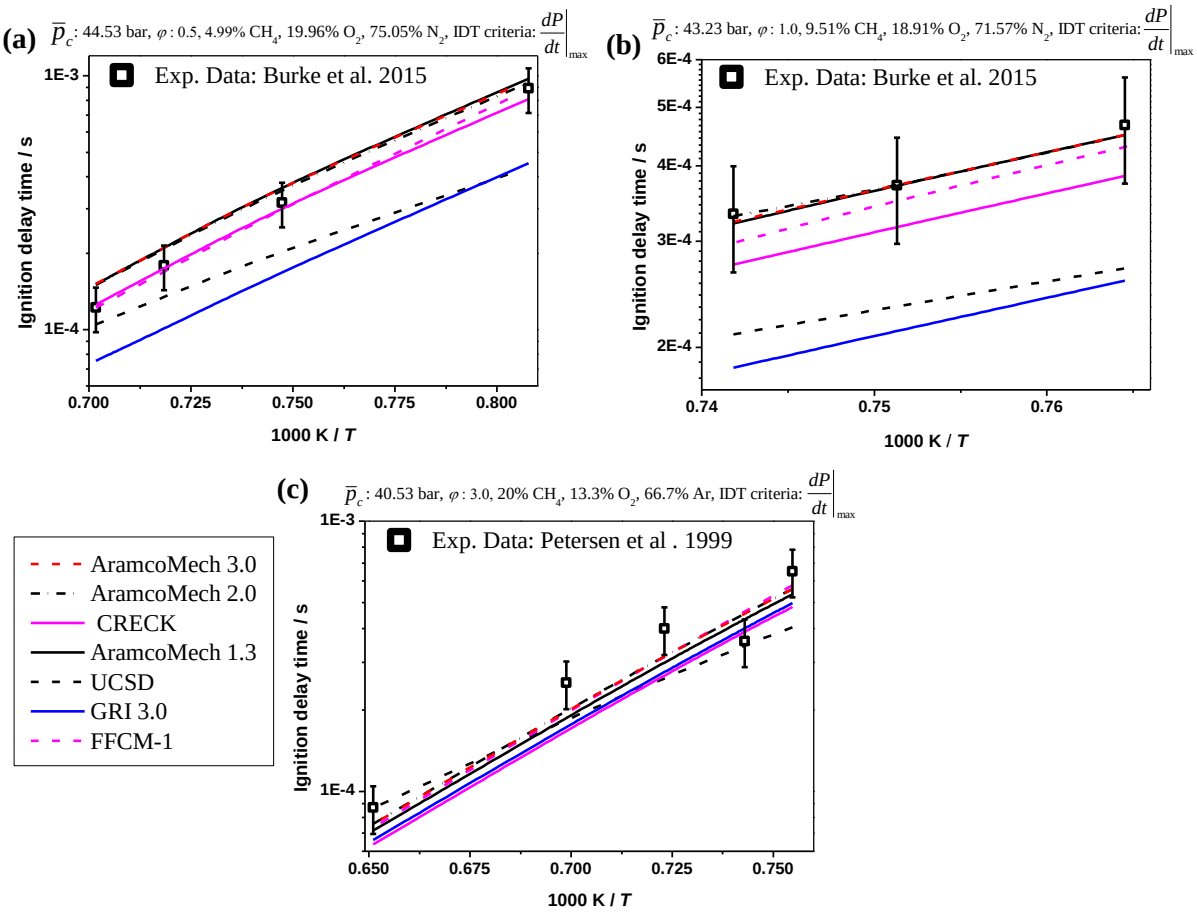

Figure S4. Experimental and simulation data of methane's IDT values for average compressed reactive mixture pressure (p_c): (a) P1C7; (b) P1C5; (c) P1C3.

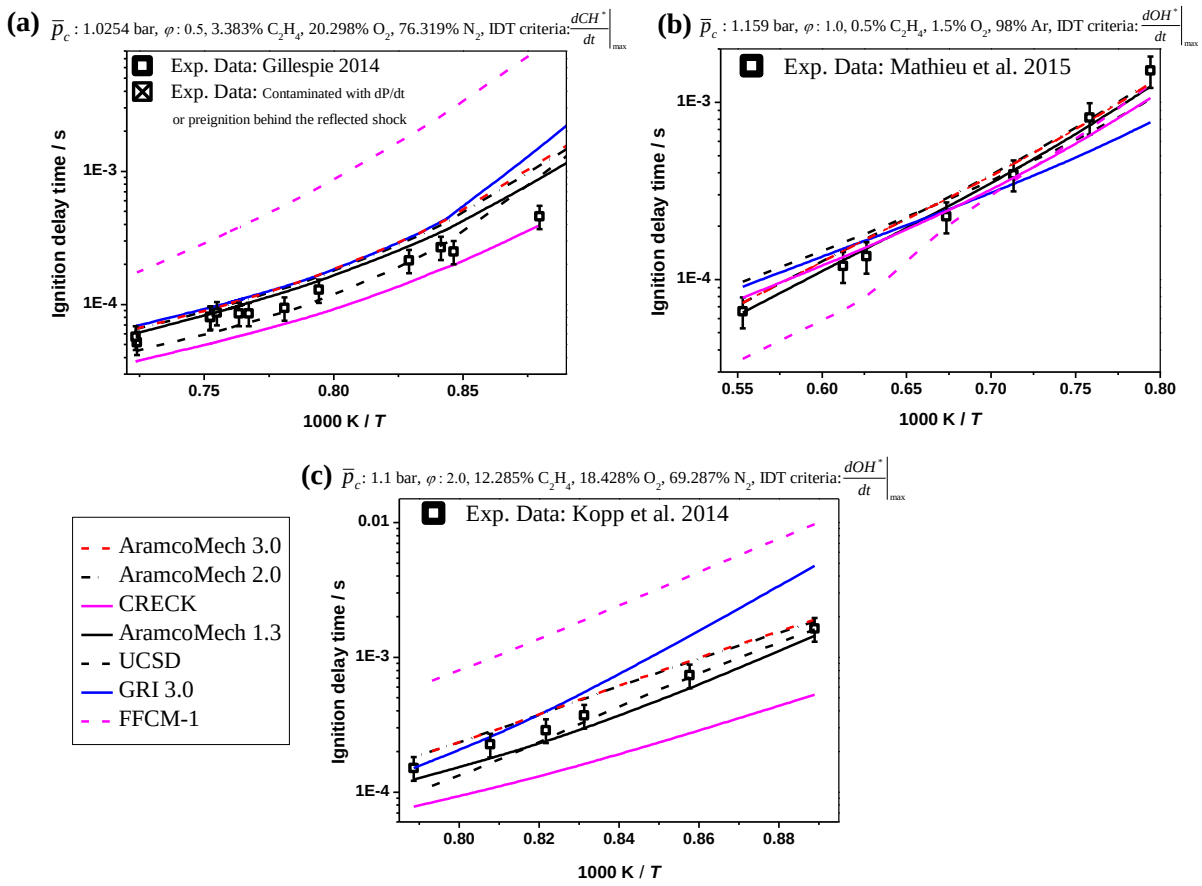

Figure S5. Available experimental and simulated data of ethylene's IDT values for average compressed reactive mixture pressure (p_c): (a) P2C1; (b) P2C8; (c) P2C6.

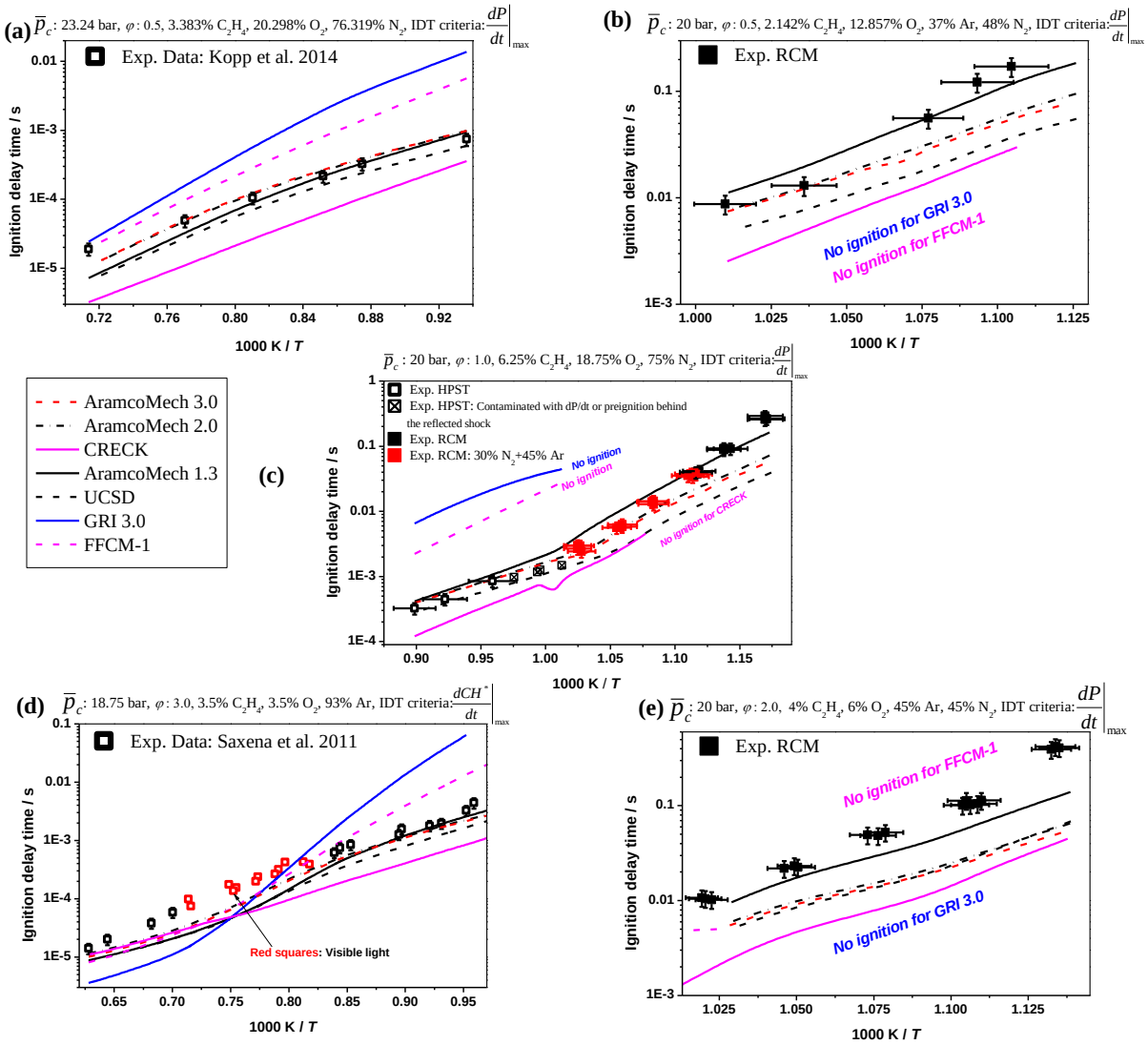

Figure S6. Available experimental and simulated data of ethylene's IDT values for average compressed reactive mixture (p_c): (a) P2C4; (b) P2C4; (c) P2C2; (d) P2C9; (e) P2C9.

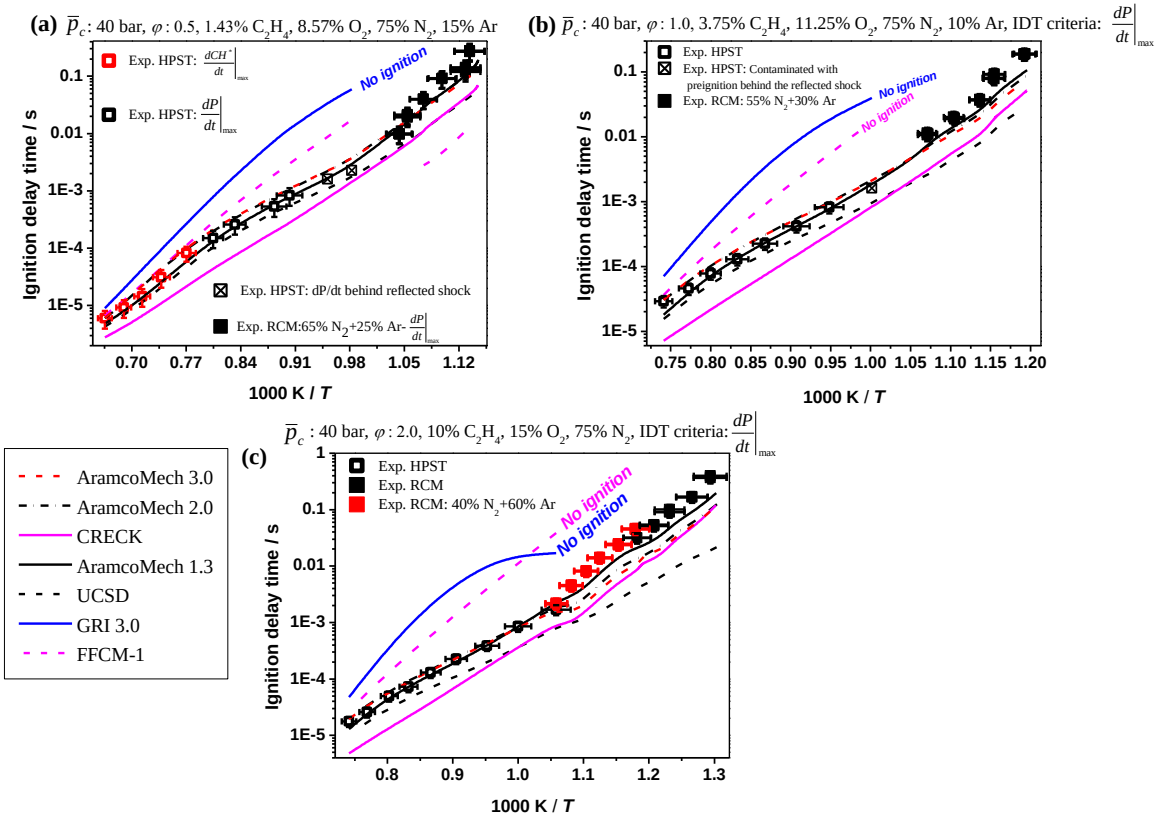

Figure S7. Experimental and simulated data of ethylene's IDT values for average compressed reactive mixture pressure (p_c): (a) P2C7; (b) P2C5; (c) P2C3.

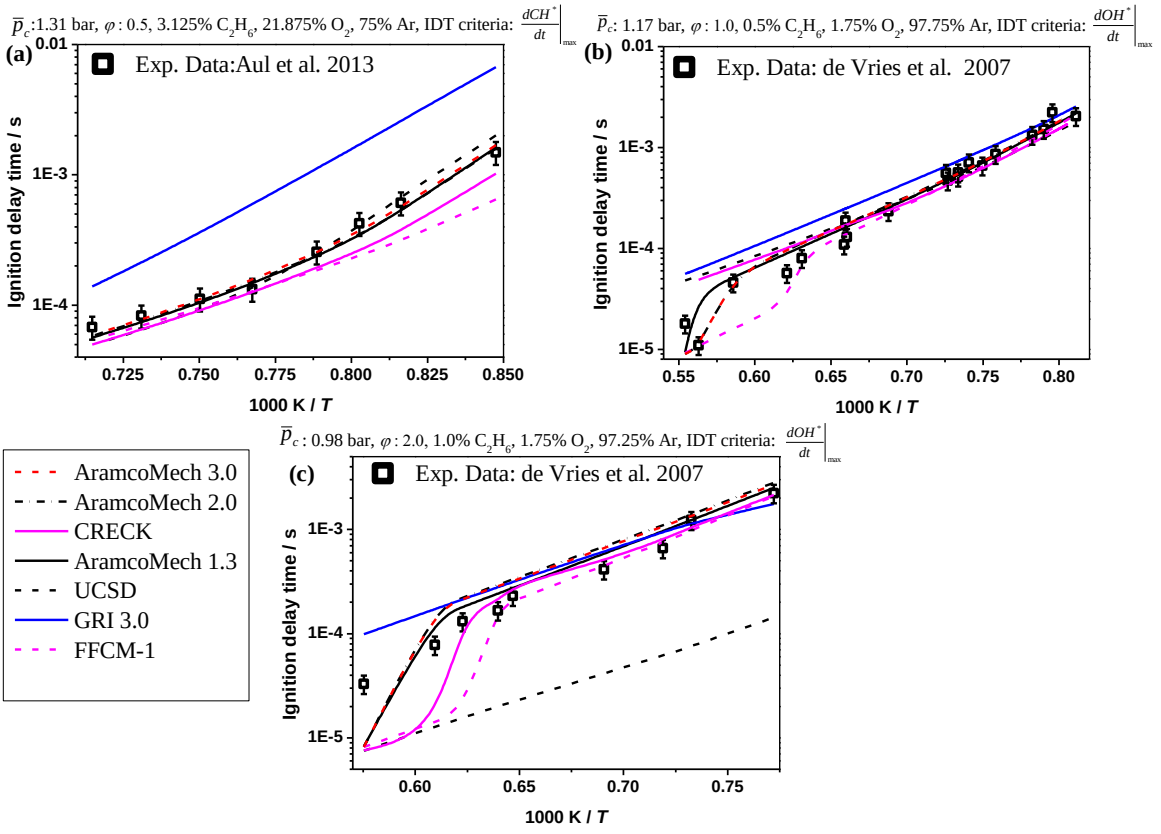

Figure S8. Available experimental and constant volume simulation data of ethane's IDT values for average compressed reactive mixture pressure (p_c): (a) P3C1; (b) P3C8; (c) P3C6. Although, OH* species is not included in UCSD and GRI 3.0 mechanisms, OH results have been presented instead of OH*.

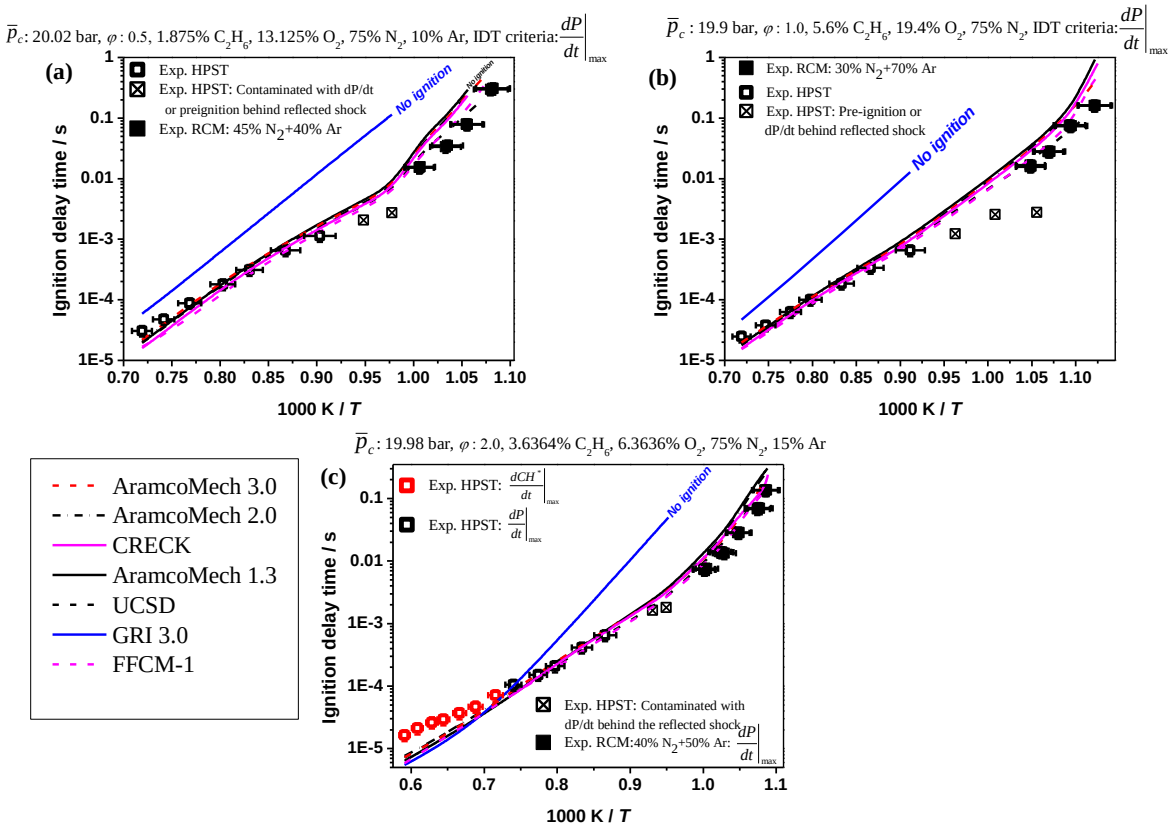

Figure S9. Experimental and simulation data of ethane's IDT values for average compressed reactive mixture pressure (p_c): (a) P3C4; (b) P3C2; (c) P3C9.

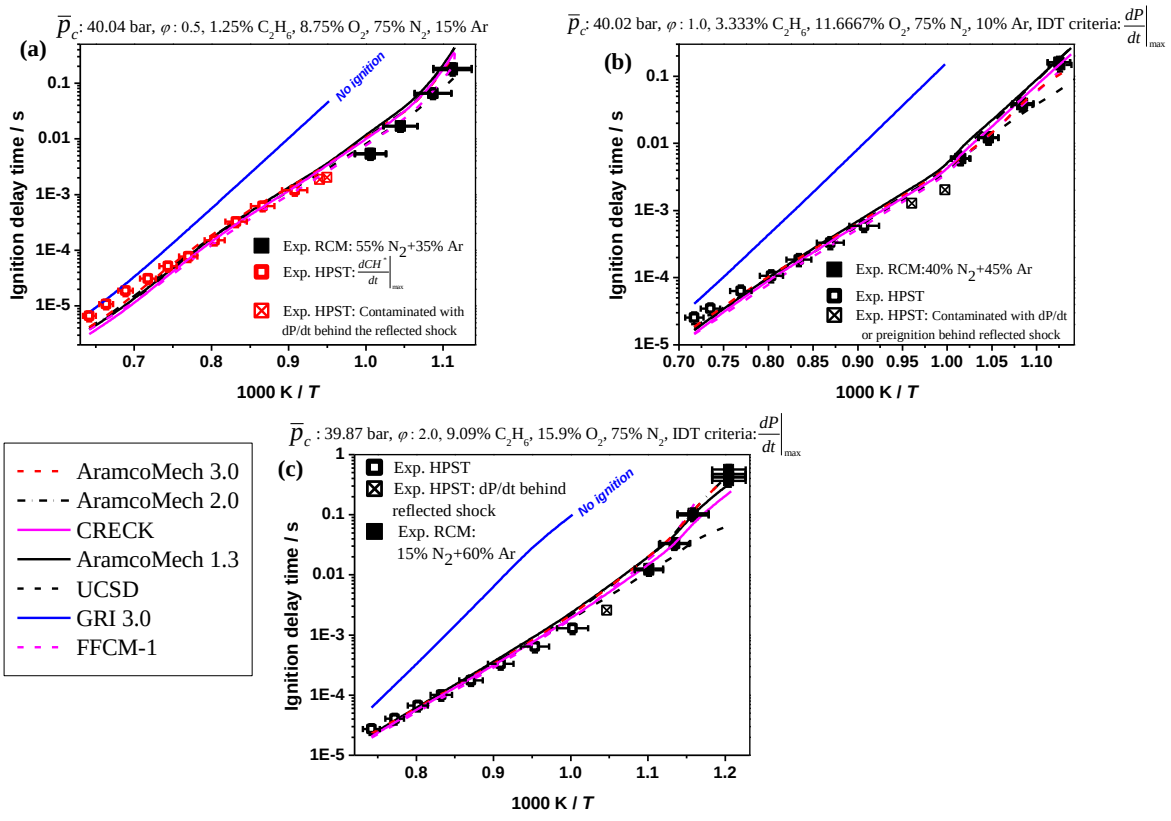

Figure S10. Experimental and simulation data of ethane's IDT values for average compressed reactive mixture pressure (p_c): (a) P3C7; (b) P3C5; (c) P3C3.

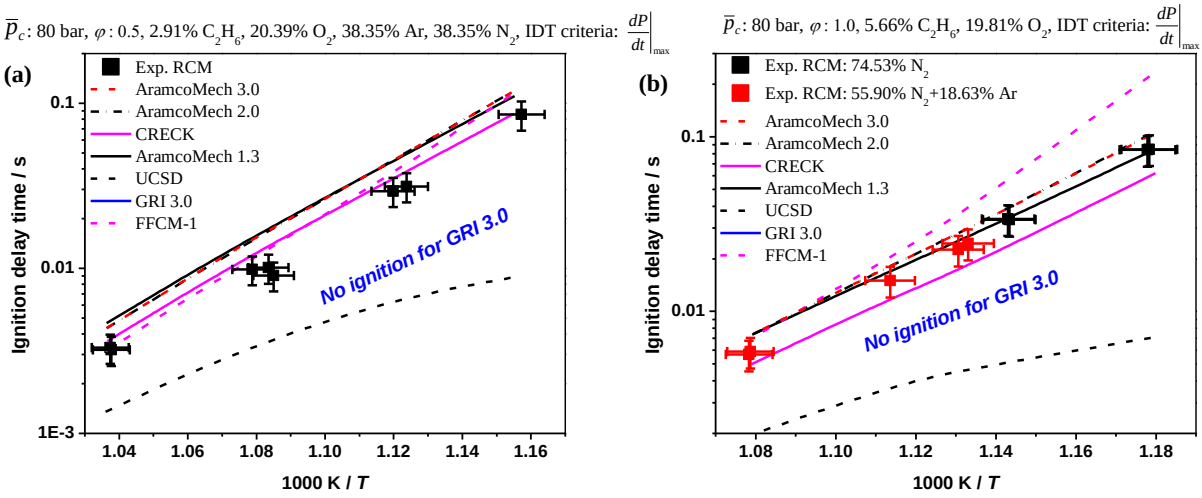

Figure S11. Experiemntal and simulated data of ethane's IDT values for average compressed reactive mixture (p_c): (a) P3C10; (b) P3C11.

3 Design of experiments

According to complexity of classical approaches for designing experiments, the Taguchi method is a robust approach for designing complex experimental researches through reducing the experimental tests. This methodology would be prominent when many experiments should be carried–out in accordance to increasing numbers of variables. Hence, for handling experimental studies with many experiments (in the current study, 81 datasets), the Taguchi approach can tackle the issue using a specific design of orthogonal arrays which allows to conduct a comprehensive investigation by doing minimized experimental tests. In this regard, the minimum number of experiments is determined as follows:

$$N_{Taguchi} = 1 + NF\,(L - 1) \quad (1)$$

Where, $N_{Taguchi}$, NF, and L are the number of experiments, number of factors, and number of levels, respectively. According to the Taguchi approach, its performance would be optimal when there are limited interactions between desired variables. Therefore, in the current research, it was supposed that the interactions between the various factors and variables are negligible. In order to use the Taguchi method, it is essential to define the controlling factors and levels. According to the factors and levels, several design of experiments (DOE) matrixes will be available. For instance, as seen in Table S2, if there are three or four factors (e.g. fuel composition; A, dilution level; B, equivalence ratio; C, and pressure; D) and 3 levels for each parameter (e.g. three pressure levels, 1, 20, and 40 bar) L_9 orthogonal array could be employed for designing the required experiments. According to Equation 1 and Table S2, one can easily determine $N_{Taguchi}$ based on the number of factors and levels, which is 9. Therefore, it is required to use an L_9 DOE matrix to cover such test numbers. Here, it should be noted that although the first column in Table S2 is identical in the current study, it will be changed to three levels in the upcoming studies of the authors for blended C_1–C_3 fuels. Thus, it was preferred to use an identical style

of the Taguchi matrix (L_9) for designing the whole sets of experiments which were required to complete the developed database.

Table S2. Applied factors/variables and levels for designing the current experiments using the Taguchi method.

Factors / ***Levels***	***Fuel composition (A)***	***Dilution (B)***	***Equivalence ratio (C)***	***Pressure (bar) (D)***
1	100% C_2H_4	75%	0.5	1.0
2	100% C_2H_4	85%	1.0	20.0
3	100% C_2H_4	90%	2.0	40.0

A sample form of an L_9 Taguchi array is shown in the following:

$$\begin{bmatrix} A & B & C & D \\ 1 & 1 & 1 & 1 \\ 1 & 2 & 2 & 2 \\ 1 & 3 & 3 & 3 \\ 2 & 1 & 2 & 3 \\ 2 & 2 & 3 & 1 \\ 2 & 3 & 1 & 2 \\ 3 & 1 & 3 & 2 \\ 3 & 2 & 1 & 3 \\ 3 & 3 & 2 & 1 \end{bmatrix} \rightarrow \begin{bmatrix} A & B & C & D \\ 100 & 75 & 0.5 & 1.0 \\ 100 & 85 & 1.0 & 20.0 \\ 100 & 90 & 2.0 & 40.0 \\ 100 & 75 & 1.0 & 40.0 \\ 100 & 85 & 2.0 & 1.0 \\ 100 & 90 & 0.5 & 20.0 \\ 100 & 75 & 2.0 & 20.0 \\ 100 & 85 & 0.5 & 40.0 \\ 100 & 90 & 1.0 & 1.0 \end{bmatrix}$$

As mentioned before, the selection of proper DOE Taguchi matrix is only based on the number of desired parameters (here, fuel composition, pressure, equivalence ratio, and dilution percent) and their variation levels (here, three levels have been chosen (e.g. 0.5, 1.0, and 2.0 for equivalence ratio). In accordance to the selected parameters and their respective levels, the proper Taguchi matrix will give the least number of experiments which are required to get accurate results using the best configuration of the experiments with the desired levels [13]. However, it should be noted that according to the statistical mathematics fundamentals which the Taguchi matrixes are derived based on, unnecessary increasing the selected parameters and their respective levels (for example: increasing the parameters from 4 to 5 and the levels from 3 to 4) will significantly increase the number of tests (from L_9 with 9 configurations to L_{16} with 16 configurations) and consequently required time for completing the experimental tests. Therefore, regarding the available data in the literature, it was decided to select main parameters of fuel composition, pressure, equivalence ratio, and dilution percent as study parameters with three levels to satisfy the requirements of the study.

4 Applied gases for making the mixtures

As mentioned in the design of experiments' section of the paper, in the current study, the ignition delay time characteristics of ethane (C_2H_6) and ethylene (C_2H_4) have been investigated individually over a wide range of temperature, pressure, equivalence ratio, and dilution. For those experiments

performed at the combustion chemistry centre (C^3) of National University of Ireland, the studied alkane/alkene fuels with purity of 99.5% (Grade: 2.5) have been supplied through high pressure bottles which were provided from Air liquide UK. The other applied gases such as oxygen, argon, nitrogen, and helium in the experiments have been provided by BOC Ireland with purities of O_2 (99.99%), N_2 (99.99%), Ar (99.99%), and He (99.96%). However, for those experiments performed at the Physico–Chemical Fundamentals of Combustion (PCFC) of RWTH Aachen University, the studied C_2H_6 with purity of 99.95% (Grade: 3.5) was provided by Westfalen AG. Also, the other applied gases such as oxygen, argon, and nitrogen, in the experiments have been provided by Westfalen AG and Praxair with purities of O_2 (($\geq$99.995%), N_2 (($\geq$99.95%), and Ar ($\geq$99.996%).

5 High–pressure shock–tube

As known, shock–tube is a robust facility for getting the ignition delay time data under high pressure–high temperature ($\geq$ 1000 K) regime and IDTs $\leq$ 2 ms. Thus, the NUIG–HPST has been used for getting the IDT data under these operating conditions. As already mentioned, the applied NUIG–HPST has been previously documented and explained in details [14] and ,here, only general information of the facility is presented in Table S3. In the current study, helium was used as the primary driver gas for doing the experiments unless there was a need to reduce the incident shock velocity through adding nitrogen to helium for the tailored cases.

Table S3. Specifications of the applied high–pressure shock tube.

Total length	9.1 m	
Section	Length (m)	Diameter (mm)
Driver	3.0	63.5
Middle	0.04	63.5
Driven	5.7	63.5
Material	Stainless–steel (1.4571/316Ti and 1.4462/F51)	
Controlling system	Double–diaphragm type	
Diaphragm's material	Aluminium (1050 H14)	
Diaphragm's thickness	0.8~2 mm; according to target pressure	
Pre-scoring the diaphragms	0.2~1.1 mm; according to target pressure and the diaphragms' thickness	

Further, as presented in Table S4, the incident shock velocity has been measured using six piezoelectric pressure transducers located on the driven section of the HPST and then the shock velocity at the end–wall was extrapolated through a fitted line to the collected shock velocities over these pressure transducers. All of conditions such as the compressed gas temperature (T_5) and pressure (p_5) behind the reflected shock were calculated using the shock velocity at the end–wall through "Gaseq" software [15]. Also, the ignition delay times of the studied normal mixtures (pressure–time profiles) with diluent concentration of $\leq$ 85% were recorded using a Kistler 603B transducer mounted on the end–wall, while for the mixtures with 90% dilution, the ignition delay times were measured using photodiode

array detector (PDA) or photomultiplier (PMT) systems equipped with CH^* filter (CWL: 430 nm ± 10 FWHM; Thorlabs) installed on the side wall of the shock tube's endcap due to very weak signals of the Kistler pressure transducer. Also, it is demonstrated in Figure S12 that the ignition delay time is defined as a maximum gradient in pressure ($\frac{dP}{dt}\Big|_{max}$) or CH^* ($\frac{dCH^*}{dt}\Big|_{max}$) behind the reflected shock. Further, for increasing the accuracy of experiments and reducing the scattered points, all measured pressures behind the reflected shocks have been forced to be restricted to ±0.5 bar of the target pressures (20 and 40 bar). Moreover, all the experimental results have been divided into two main categories of the acceptable and the affected by facility, so that the affected results have been marked using "☒" symbol. Thus, these data wouldn't be reliable to be applied for evaluating the performance of a chemical mechanism. In this regard, all pressure versus time data including oscilloscope files (software is accessible through https://www.tiepie.com/en/oscilloscope-software) and the experimentalist spreadsheets related to the current studied conditions in NUIG–HPST are provided as supplementary files.

Table S4. Number of installed PCB sensors on the driven section of the shock–tube and their distances from the end–wall

Sensors	Distance from the end wall (m)
PCB#1	0.01
PCB#2	0.15
PCB#3	0.29
PCB#4	0.57
PCB#5	0.85
PCB#6	1.165

(a)

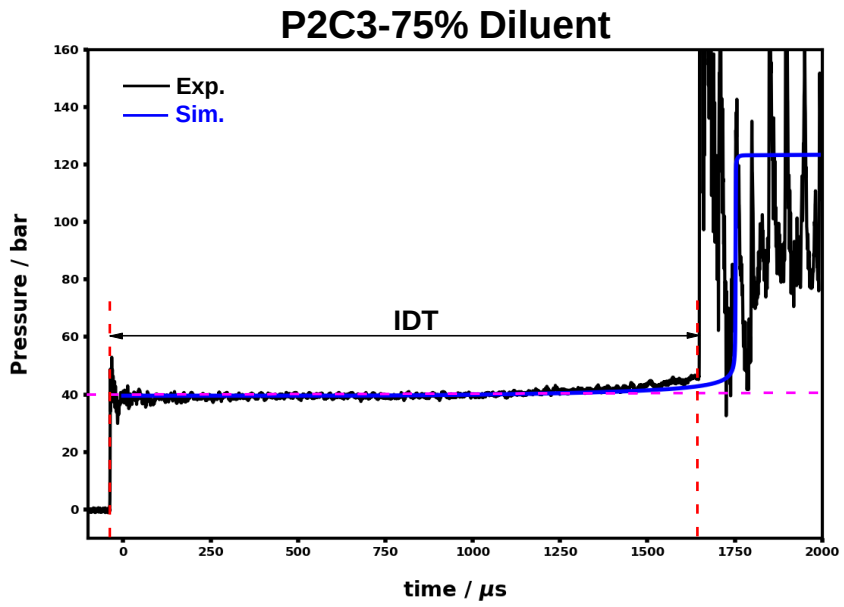

(b)

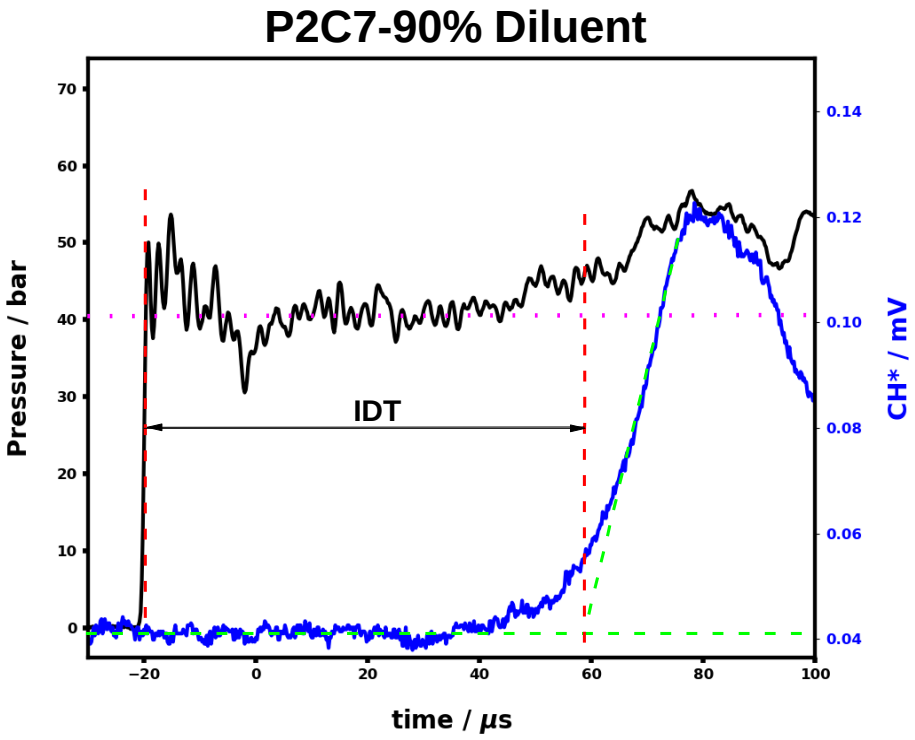

Figure S12. Applied definition for measuring IDT in the NUIG-shock tube: (a) using Kistler pressure trace mounted on the end-wall of the endcap; (b) using PDA–CH^* trace mounted on the side wall of the end–cap.

6 Rapid compression machine

The rapid compression machine is a common facility for getting the ignition delay time data under high pressure and low–to–moderate temperature regime (<1000 K). In the current study, the experiments related to the compressed mixture pressure $p_c \leq 40$ bar and $p_c > 40$ bar have been taken using

NUIG–RCM and PCFC–RCM, respectively. According to the previous studies [16, 17], the experimental IDTs have been modelled using the adiabatic core assumption in which the non–adiabatic condition can be compensated by imposing the volume–time profiles of the same non–reactive mixtures to calculations. Thus, general information about each facility have been presented in the following subsections.

6.1 NUIG–RCM

The general specifications of NUIG–RCM have been presented in Table S5. The details of the facility has been already documented and explained in details by the authors [7, 14, 16, 18-20]. In this facility, the ignition delay time of the normal studied mixtures (diluent concentration = 75%) and the pressure–time histories of their relevant non–reactive mixtures were recorded using a Kistler 6045A/B transducer mounted on the reaction chamber. However, the ignition delay times of the mixtures with 85% and 90% dilution percent and the post–compression pressures of 20 and 40 bar, were reordered using both the Kistler and a photomultiplier (PMT) equipped with CH^* filter (CWL: 430 nm ± 10 FWHM; Thorlabs) due to vague signal of the Kistler pressure transducer under these conditions. Also, as shown in Figure S13, the ignition delay time is defined as a maximum gradient in pressure ($\frac{dP}{dt}\Big|_{max}$) or CH^* ($\frac{dCH^*}{dt}\Big|_{max}$) after compressing the studied mixtures. Subsequently, the post compression temperatures (T_c) were calculated by assuming isentropic compression condition using Gaseq software [15]. Similar to the applied procedure in NUIG–HPST, all of measured post compression pressures (p_c) have been forced to be restricted to ±0.5 bar of the target pressures due to increasing the accuracy of the experiments and also reducing scattered points. Moreover, unlike the standard operating procedure in NUIG–HPST, all of the experimental results have been repeated at least three times and the repeatability of all reported IDTs was ≥ 90%. In this regard, all pressure versus time data including pressure/volume profiles and the experimentalist spreadsheets related to the studied conditions in NUIG–RCM have been provided as supplementary files.

Table S5. Specifications of NUIG–RCM.

Parameter	Value
Bore size of the reaction chamber (m)	0.03820
Volume of the reaction chamber (m^3)	3.3191×10^{-5}
Piston's velocity (U_p) (m/s)	9.34 ~ 12.94
Pistons' stroke length (m)	0.16817
Piston's type	Flat head with the crevice
Type	Twin–counter pistons

(a)

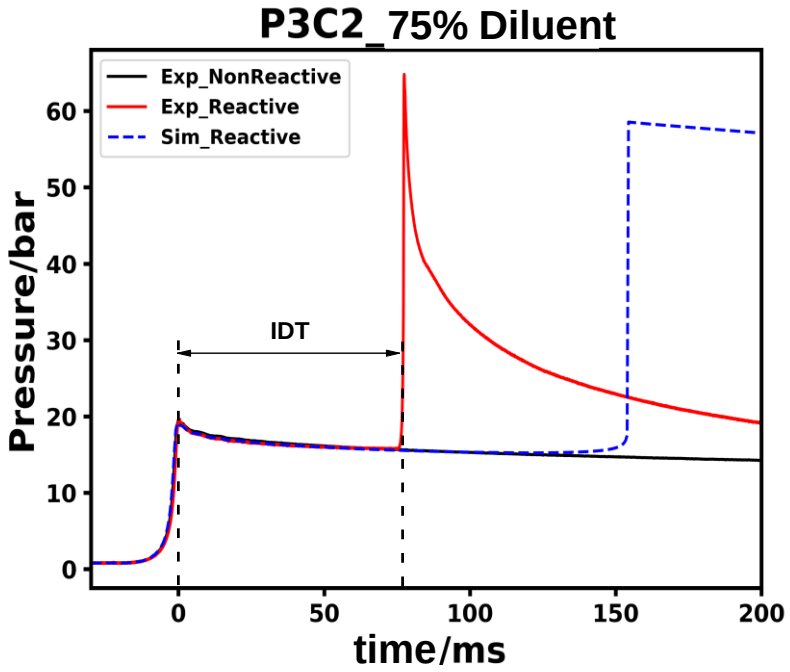

(b)

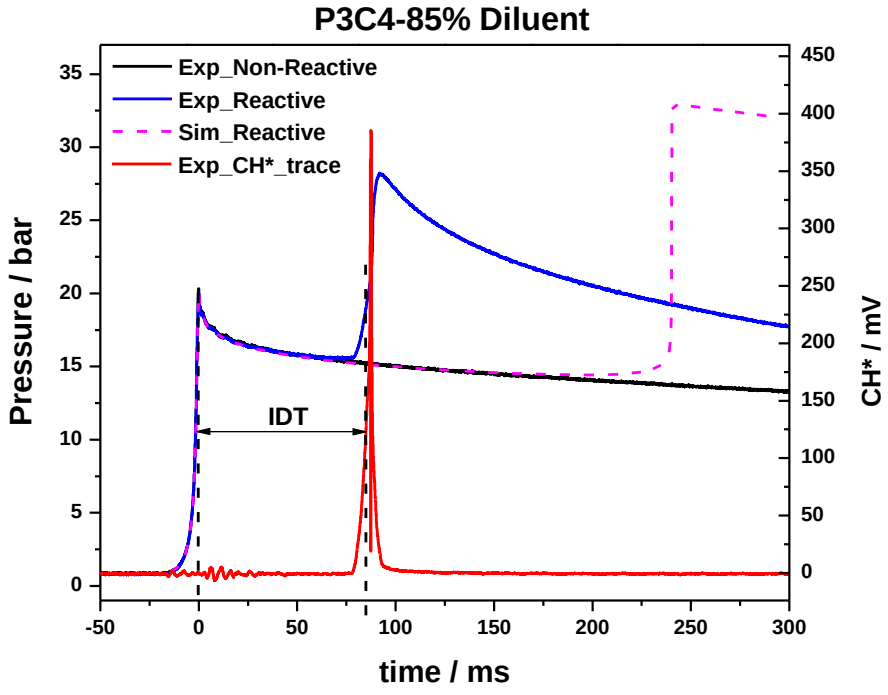

Figure S13. Applied definition for measuring IDT in the NUIG–RCM: (a) using Kistler pressure trace; (b) using both pressure and PMT–CH^* trace mounted on the side wall of the reaction chamber.

6.2 PCFC–RCM

The PCFC–RCM is a well–known facility which has been already introduced properly in literature. As mentioned above, all of the experimental tests related to the compressed pressures (p_c) of higher than 40 bar and within low–to–moderate temperature rage, have been performed in RCM facility of the Physico–Chemical Fundamentals of Combustion (PCFC) of RWTH Aachen University. As presented

in Table S5, this facility is constructed from a single–piston mechanism which is driven pneumatically and stopped hydraulically at the end of compression. Similar to the applied piston in NUIG–RCM, the crevice piston design has been applied in the PCFC–RCM. In the facility, the pressure–time profile during the compression and post–compression processes and the initial temperature in the reaction chamber were monitored and controlled using a Kistler 6125C pressure transducer and type 'T' thermocouple, respectively. In this regard, the detail information about the construction, measurement procedure, and the applied sensors in the study have been already presented in [21]. As the same process explained in section 6.1, the compressed mixture's temperature (T_5) was calculated using the isentropic compression formulation of Gaseq software [15]. According to the procedure explained by Ramalingam et al. [17], the reproducibility of evaluated IDTs and also the experimental uncertainty of the compressed mixture's temperature for the measured conditions in the study were within 15% and ±5 K, respectively. In this regard, the related experimental data to PCFC–RCM facility and the volume–time profiles are reported in supplementary files.

Table S6. Specifications of PCFC–RCM.

Parameter	Value
Bore size of the reaction chamber (m)	0.05
Volume of the reaction chamber (m^3)	5.06×10^{-4} – 5.51×10^{-4}
Piston's velocity (U_p) (m/s)	16.67
Pistons' stroke length (m)	0.25
Piston's type	Flat head with the crevice
Type	Single piston

7 Data acquisition system

As shown in Table S7, in the current study, many sensors have been used in the three applied facilities at C^3–NUIG and PCFC–RWTH Aachen University to measure the required parameters. In this regard, all installed sensors in NUIG–HPST which had been used for measuring the incident shock velocities and the ignition delay times, were synchronized and connected to two TiePie Handyscope HS4 oscilloscopes [22]. Also, all generated signals from the installed sensors on NUIG–RCM including the Kistler pressure transducer, the position sensors, and the photomultiplier were synchronized and collected using a PicoScope 5443B [23].

Table S7. Applied sensors and detectors for measuring during the current study (NUIG–HPST/RCM and PCFC–RCM).

Sensor	Company	Model	Accuracy	Resolution
Pressure sensor transducer	Kistler	603B	≤±1.0 % FSO; linearity	NA
Pressure sensor transducer	Kistler	6045A	≤±0.4 % /FSO; linearity	NA
Pressure sensor transducer	Kistler	6125C	≤±0.4 % /FSO; linearity	NA
Piezoelectric pressure sensor	PCB	113B24	≤±1.0 % FS; Non-linearity	±0.035 KPa

Digital Absolut pressure transmitter	MKS	Baratron 121AA-0100D	0.5% of reading	±0.01 Torr
Digital Absolut pressure transmitter	MKS	Baratron 121AA-01000D	0.5% of reading	±0.1 Torr
Digital Absolut pressure transmitter	MKS	Baratron 121AA-05000B	0.5% of reading	±0.5 Torr
Analog vacuum pressure gauge	Edwards	Pirani-PRE10K	NA	±2 of reading scale
Thermocouples and Controller	Radionics	T-type	±1.0 ˚C	±0.1 ˚C
Photodetector	Thorlabs	PDA36A/PDA55	NA	NA
Photomultiplier	EMI Electronics	9924P	NA	NA

8 Uncertainty analysis

For getting a detailed understanding about the uncertainty of the experimental tests of the current study, the following subsections have been presented. In fact, these subsections try to analytically explain the effect of some important factors including pressure, temperature, and equivalence ratio on the total uncertainty of the experimental results. It seems that the output of the section could provide a good clue for better analysing and evaluating the quality of the experimental data.

8.1 Equivalence ratio

In the following lines, it is tried to somehow evaluate probable uncertainties which may be included in equivalence ratios of the applied mixtures of the current study.

Making a mixture:

Fuel: $F = p_F = \sum_{i=1}^{n} p_i \rightarrow \sigma_F = \sqrt{\sum_{i=1}^{n} {\sigma_i}^2}$ (2)

Where, p_i and σ_i are absolute pressure of i–th component in the fuel mixture and uncertainty of each absolute pressure of i–th component in the fuel mixture, respectively. Because, in the current study, only single fuel mixtures have been studied, thus: Fuel: $F=p_F \pm \sigma_F$ and Oxygen: $O=p_{O2} \pm \sigma_{O2}$.

Equivalence ratio: $\varphi = \frac{\left(\frac{F}{O}\right)_{real}}{\left(\frac{F}{O}\right)_{Stoi}} \rightarrow \left(\frac{O}{F}\right)_{Stoi} = Cte \rightarrow \varphi = Cte\left(\frac{F}{O}\right)_{real} \rightarrow \sigma_\varphi = \left(\frac{\partial \varphi}{\partial F}\right)\sigma_F + \left(\frac{\partial \varphi}{\partial O}\right)\sigma_O$ (3)

$$\frac{\partial \varphi}{\partial F}\cdot\sigma_F = \frac{\partial \varphi}{\partial p_1}\cdot\frac{\partial p_1}{\partial F}\cdot\sigma_1 + \frac{\partial \varphi}{\partial p_2}\cdot\frac{\partial p_2}{\partial F}\cdot\sigma_2 + \frac{\partial \varphi}{\partial p_3}\cdot\frac{\partial p_3}{\partial F}\cdot\sigma_3 + \cdots + \frac{\partial \varphi}{\partial p_n}\cdot\frac{\partial p_n}{\partial F}\cdot\sigma_n \rightarrow \frac{\partial p_n}{\partial F} = 1 \rightarrow \frac{\partial \varphi}{\partial F}\cdot\sigma_F = \frac{\partial \varphi}{\partial p_1}\cdot\sigma_1 + \frac{\partial \varphi}{\partial p_2}\cdot\sigma_2 + \frac{\partial \varphi}{\partial p_3}\cdot\sigma_3 + \cdots + \frac{\partial \varphi}{\partial p_n}\cdot\sigma_n \rightarrow \varphi = Cte\left(\frac{\sum_{i=1}^{n} p_i}{O}\right)_{real} \rightarrow \frac{\partial \varphi}{\partial p_n} = \frac{1}{O} \rightarrow \frac{\partial \varphi}{\partial O} = -\frac{\sum_{i=1}^{n} p_i}{O^2}$$

$$\sigma_\varphi = \frac{\partial \varphi}{\partial p_1}\cdot\sigma_1 + \frac{\partial \varphi}{\partial p_2}\cdot\sigma_2 + \frac{\partial \varphi}{\partial p_3}\cdot\sigma_3 + \cdots + \frac{\partial \varphi}{\partial p_n}\cdot\sigma_n + \left(-\frac{\sum_{i=1}^{n} p_i}{O^2}\right)\sigma_O$$

If we assume that there is no correlation between measurements of $\sigma_i \sigma_j = 0$

$${\sigma_\varphi}^2 = \left(\frac{\partial \varphi}{\partial p_1}\cdot\sigma_1\right)^2 + \left(\frac{\partial \varphi}{\partial p_2}\cdot\sigma_2\right)^2 + \left(\frac{\partial \varphi}{\partial p_3}\cdot\sigma_3\right)^2 + \cdots + \left(\frac{\partial \varphi}{\partial p_n}\cdot\sigma_n\right)^2 + \left(\left(-\frac{\sum_{i=1}^{n} p_i}{O^2}\right)\sigma_O\right)^2$$

$$\sigma_\varphi = \sqrt{\left(\frac{1}{p_{O_2}}\cdot\sigma_1\right)^2 + \left(\frac{1}{p_{O_2}}\cdot\sigma_2\right)^2 + \left(\frac{1}{p_{O_2}}\cdot\sigma_3\right)^2 + \cdots + \left(\frac{1}{p_{O_2}}\cdot\sigma_n\right)^2 + \left(\left(-\frac{\sum_{i=1}^{n} p_i}{{p_{O_2}}^2}\right)\sigma_O\right)^2}$$

$$\sigma_\varphi = \sqrt{\left(\frac{\sum_{i=1}^{n}{\sigma_i}^2}{{p_{O_2}}^2}\right) + \left(\left(-\frac{p_F}{{p_{O_2}}^2}\right)\sigma_O\right)^2} = \sqrt{\left(\frac{\sigma_F}{p_{O_2}}\right)^2 + \left(\left(-\frac{p_F}{{p_{O_2}}^2}\right)\sigma_O\right)^2} = \frac{Cte}{p_{O_2}^2}\sqrt{p_{O_2}^2\sigma_F^2 + p_F^2\sigma_O^2} \quad (4)$$

Based on the above analysis, the uncertainties of all made mixtures in the current study are presented individually in Table S8 as follows:

Table S8. Uncertainty analysis of equivalence ratio for all made mixtures.

Code	Facility	$\left(\frac{O}{F}\right)_{Stoi}$	P_F (mbar)	$\pm\sigma_f$ (mbar)	P_O (mbar)	$\pm\sigma_O$ (mbar)	$\pm\sigma_\varphi$
P2C2	HPST	3	333.3	1.7	999.9	6.7	8.4211E–03
	RCM		125	0.6	375	2.5	8.2149E–03
P2C3	HPST	1.5	533.3	2.7	799.9	6.7	9.7879E–03
	RCM		200	1.0	300	2.5	9.7182E–03
P2C4	RCM	6	42.84	0.21	257.1	1.5	7.6185E–03
P2C5	HPST	3	200.0	1.0	599.9	4.0	8.3356E–03
	RCM		75	0.38	225	1.5	8.3735E–03
P2C7	HPST	6	76.26	0.38	457.0	2.7	7.7383E–03
	RCM		28.6	0.14	171.4	1.0	7.6247E–03
P2C9	RCM	1.5	80.00	0.40	120.0	1.0	9.7183E–03
P3C2	HPST	3.5	298.6	1.5	1034.6	6.7	8.2791E–03
	RCM		112	0.6	388	2.5	8.4658E–03
P3C3	HPST	1.75	484.8	2.4	848.0	6.7	9.3281E–03
	RCM		181.8	0.9	318.0	2.5	9.2948E–03
P3C4	HPST	7	99.99	0.50	699.9	4.0	7.5942E–03
	RCM		37.5	0.19	262.5	1.5	7.6370E–03
P3C5	HPST	3.5	177.7	0.9	622.2	4.0	8.1809E–03
	RCM		66.66	0.33	233.3	1.5	8.1149E–03

P3C7	HPST	7	66.66	0.33	466.6	2.7	7.6155E–03
	RCM		25	0.13	175	0.9	7.3136E–03
P3C9	HPST	1.75	193.9	1.0	339.4	2.7	9.4786E–03
	RCM		72.73	0.36	127.3	1.0	9.2832E–03

8.2 Diluent concentration

For determining the uncertainty of diluent concentration in the studied mixtures the following formulations are presented:

$$[D] = \frac{p_i}{RT_i} \tag{5}$$

$$\sigma_{[D]} = \frac{\partial [D]}{\partial p_i}\sigma_{p_i} \tag{6}$$

$$\frac{\partial [D]}{\partial p_i} = \frac{1}{RT_i} \tag{7}$$

Because, in the study, all mixtures have been prepared under 303 K, so the Equation 7 would be as follows:

$$\frac{\partial [D]}{\partial p_i} = 3.96961 \times 10^{-4}$$

Therefore, the worst uncertainty in diluent concentration in the studied mixtures is related to cases with 90% diluent in a mixture with total pressure of 4000 Torr which yields $\sigma_{[D]} = \pm 1.05848\ \frac{mol}{m^3} = \pm 1.05848 \times 10^{-5}\ \frac{mol}{10^5.m^3} \approx \pm 0.56\%\ [D]$. For calculating the uncertainty in concentration of each species under the compressed conditions, the following formulations are presented:

$$[D] = \frac{p_{c,[D]}}{RT_c} \tag{8}$$

$$\sigma_{[D]} = \sqrt{\left(\frac{\partial [D]}{\partial p_{c,[D]}}\sigma_{p_{c,[D]}}\right)^2 + \left(\frac{\partial [D]}{\partial T_c}\sigma_{T_c}\right)^2} \tag{9}$$

$$\sigma_{[D]} = \sqrt{\left(\frac{1}{RT_c}\sigma_{p_{c,[D]}}\right)^2 + \left(-\frac{p_{c,[D]}}{RT_c^2}\sigma_{T_c}\right)^2} = \frac{1}{8.314 \times T_c^2}\sqrt{\left(T_c\sigma_{p_{c,[D]}}\right)^2 + \left(p_{c,[D]}\sigma_{T_c}\right)^2} \tag{10}$$

8.3 IDTs in Shock–tube

If the following equations, for determining total uncertainty of the measured ignition delay times in NUIG–HPST, it is assumed:

$$p_c = P(p_1, V_s, \varphi, T_1);\ T_c = T(T_1, V_s, \varphi)$$

As shown by Petersen et al. [24], one could assume that:

$$T_C = \frac{T_1\left[2(\gamma_1-1)M^2+(3-\gamma_1)\right]\left[(3\gamma_1-1)M^2-2(\gamma_1-1)\right]}{(\gamma_1+1)^2M^2};\ M = \frac{V_s}{\sqrt{\gamma_1 RT_1}};\ V_s = \frac{\Delta z}{\Delta t} \tag{11}$$

$$\sigma_{V_s} = \sqrt{\left(\frac{\partial V_s}{\partial(\Delta z)}\sigma_{\Delta z}\right)^2 + \left(\frac{\partial V_s}{\partial(\Delta t)}\sigma_{\Delta t}\right)^2} = \sqrt{\left(\frac{1}{\Delta t}\sigma_{\Delta z}\right)^2 + \left(-\frac{\Delta z}{(\Delta t)^2}\sigma_{\Delta t}\right)^2} \tag{12}$$

$$\sigma_{T_c} = \sigma_T = \frac{\partial T_c}{\partial M}\sigma_M = \left(T_1\left[\left(\frac{4\left(3\gamma_1^2-4\gamma_1+1\right)}{(\gamma_1+1)^2}\right)M + \left(\frac{4(\gamma_1-1)(3-\gamma_1)}{(\gamma_1+1)^2}\right)M^{-3}\right]\right)\frac{\sigma_{V_s}}{\sqrt{\gamma_1 RT_1}} \tag{13}$$

$$p_c = \frac{P_1\left[2\gamma_1M^2-(\gamma_1-1)\right]\left[(3\gamma_1-1)M^2-2(\gamma_1-1)\right]}{2(\gamma_1+1)+M^2\left(\gamma_1^2-1\right)};\ \sigma_{p_c} = \sigma_p = \frac{\partial p_c}{\partial M}\sigma_M =$$
$$\left(p_1\left[\frac{12M^5\gamma^4-4M^5\gamma^3+48M^3\gamma^3+32M^3\gamma^2-12M^5\gamma^2+4M^5\gamma-16M^3\gamma-20M\gamma^3+4M\gamma^2+20M\gamma-4M\gamma^4}{(M^2\gamma^2-M^2+2\gamma+2)^2}\right]\right)\frac{\sigma_{V_s}}{\sqrt{\gamma_1 RT_1}} \tag{14}$$

Here, it was supposed that the effect of changing in equivalence ratio on γ is negligible. Here, it is supposed that the maximum $\sigma_{\Delta t}$ which is related to TiePie Handyscope HS4 Oscilloscope is ±1 μs, and, $\sigma_{\Delta z}$ is ±0.001 m. Now, if it could be assumed the defined ignition delay time (IDT) could be correlated as follows, then:

$$\tau_{IDT} \cong A\cdot exp\left(\frac{B}{T}\right)p^m\varphi^n[D]^q \rightarrow \partial\tau = \frac{\partial\tau}{\partial T}\cdot\partial T + \frac{\partial\tau}{\partial p}\cdot\partial p + \frac{\partial\tau}{\partial\varphi}\cdot\partial\varphi + \frac{\partial\tau}{\partial[D]}\cdot\partial[D] \rightarrow (\sigma_\tau)^2 = \left(\frac{\partial\tau}{\partial T}\cdot\partial T\right)^2 + \left(\frac{\partial\tau}{\partial p}\cdot\partial p\right)^2 + \left(\frac{\partial\tau}{\partial\varphi}\cdot\partial\varphi\right)^2 + \left(\frac{\partial\tau}{\partial[D]}\cdot\partial[D]\right)^2 + 2\left(\frac{\partial\tau}{\partial T}\cdot\frac{\partial\tau}{\partial p}\cdot\partial T\partial p\right) + 2\left(\frac{\partial\tau}{\partial T}\cdot\frac{\partial\tau}{\partial\varphi}\cdot\partial T\partial\varphi\right) + 2\left(\frac{\partial\tau}{\partial\varphi}\cdot\frac{\partial\tau}{\partial p}\cdot\partial\varphi\partial p\right) + 2\left(\frac{\partial\tau}{\partial T}\cdot\frac{\partial\tau}{\partial[D]}\cdot\partial T\partial[D]\right) + 2\left(\frac{\partial\tau}{\partial p}\cdot\frac{\partial\tau}{\partial[D]}\cdot\partial p\partial[D]\right) + 2\left(\frac{\partial\tau}{\partial\varphi}\cdot\frac{\partial\tau}{\partial[D]}\cdot\partial\varphi\partial[D]\right) \tag{15}$$

Now, one assumes that there is no correlation between measurements of (p, T, and φ), so the above equation would be followed by:

$$(\sigma_{\tau,i})^2 = \left(\frac{\partial\tau}{\partial T}\cdot\partial T\right)^2 + \left(\frac{\partial\tau}{\partial p}\cdot\partial p\right)^2 + \left(\frac{\partial\tau}{\partial\varphi}\cdot\partial\varphi\right)^2 + \left(\frac{\partial\tau}{\partial[D]}\cdot\partial[D]\right)^2 + 2\left(\underbrace{\frac{\partial\tau}{\partial T}\cdot\frac{\partial\tau}{\partial p}\cdot\partial T\partial p}_{=0}\right) + 2\underbrace{\left(\frac{\partial\tau}{\partial T}\cdot\frac{\partial\tau}{\partial\varphi}\cdot\partial T\partial\varphi\right)}_{=0} + 2\left(\underbrace{\frac{\partial\tau}{\partial\varphi}\cdot\frac{\partial\tau}{\partial p}\cdot\partial\varphi\partial p}_{=0}\right) + 2\left(\underbrace{\frac{\partial\tau}{\partial T}\cdot\frac{\partial\tau}{\partial[D]}\cdot\partial T\partial[D]}_{\neq 0}\right) + 2\left(\underbrace{\frac{\partial\tau}{\partial p}\cdot\frac{\partial\tau}{\partial[D]}\cdot\partial p\partial[D]}_{\neq 0}\right) + 2\underbrace{\left(\frac{\partial\tau}{\partial\varphi}\cdot\frac{\partial\tau}{\partial[D]}\cdot\partial\varphi\partial[D]\right)}_{=0} \tag{16}$$

One could re–write the above equation as follows:

$$(\sigma_{\tau,i})^2 = \left(\frac{\partial\tau}{\partial T}\cdot\sigma_T\right)^2 + \left(\frac{\partial\tau}{\partial p}\cdot\sigma_p\right)^2 + \left(\frac{\partial\tau}{\partial\varphi}\cdot\sigma_\varphi\right)^2 + \left(\frac{\partial\tau}{\partial[D]}\cdot\sigma_{[D]}\right)^2 + 2\left(\frac{\partial\tau}{\partial T}\cdot\frac{\partial\tau}{\partial[D]}\cdot\sigma_T\sigma_{[D]}\right) + 2\left(\frac{\partial\tau}{\partial p}\cdot\frac{\partial\tau}{\partial[D]}\cdot\sigma_p\sigma_{[D]}\right) \tag{17}$$

$$\frac{\partial \tau}{\partial T} = A \cdot \left(-\frac{B}{T^2} \cdot \exp\left(\frac{B}{T}\right) p^m \varphi^n [D]^q\right) \quad (18)$$

$$\frac{\partial \tau}{\partial P} = A \cdot \left(m \cdot \exp\left(\frac{B}{T}\right) p^{m-1} \varphi^n [D]^q\right) \quad (19)$$

$$\frac{\partial \tau}{\partial \varphi} = A \cdot \left(n \cdot \exp\left(\frac{B}{T}\right) p^m \varphi^{n-1} [D]^q\right) \quad (20)$$

$$\frac{\partial \tau}{\partial [D]} = A \cdot \left(q \cdot \exp\left(\frac{B}{T}\right) p^m \varphi^n [D]^{q-1}\right) \quad (21)$$

$$\left(\sigma_{\tau,i}\right)^2 = A^2 \cdot \left(\left(-\frac{B}{T^2} \cdot \exp\left(\frac{B}{T}\right) p^m \varphi^n [D]^q\right) \cdot \sigma_T\right)^2 + A^2 \cdot \left(\left(m \cdot \exp\left(\frac{B}{T}\right) p^{m-1} \varphi^n [D]^q\right) \cdot \sigma_p\right)^2 + A^2 \cdot \left(\left(n \cdot \exp\left(\frac{B}{T}\right) p^m \varphi^{n-1} [D]^q\right) \cdot \sigma_\varphi\right)^2 + A^2 \cdot \left(\left(q \cdot \exp\left(\frac{B}{T}\right) p^m \varphi^n [D]^{q-1}\right) \cdot \sigma_{[D]}\right)^2 - 2A^2 \left(\frac{Bq}{T^2} \cdot \exp\left(\frac{2B}{T}\right) p^{2m} \varphi^{2n} [D]^{2q-1}\right) \cdot \rho_{T[D]} \sigma_T \sigma_{[D]} + 2A^2 \left(qm \cdot exp\left(\frac{2B}{T}\right) p^{2m-1} \varphi^{2n} [D]^{2q-1}\right) \cdot \rho_{p[D]} \sigma_p \sigma_{[D]} \quad (22)$$

$$\sigma_{\tau,i} \cong A \cdot \sqrt{\begin{array}{l}\left(\left(-\frac{B}{T^2} \cdot \exp\left(\frac{B}{T}\right) p^m \varphi^n [D]^q\right) \cdot \sigma_T\right)^2 + \left(\left(m \cdot \exp\left(\frac{B}{T}\right) p^{m-1} \varphi^n [D]^q\right) \cdot \sigma_p\right)^2 + \left(\left(n \cdot \exp\left(\frac{B}{T}\right) p^m \varphi^{n-1} [D]^q\right) \cdot \sigma_\varphi\right)^2 + \\ \left(\left(q \cdot \exp\left(\frac{B}{T}\right) p^m \varphi^n [D]^{q-1}\right) \cdot \sigma_{[D]}\right)^2 - 2\left(\frac{Bq}{T^2} \cdot exp\left(\frac{2B}{T}\right) p^{2m} \varphi^{2n} [D]^{2q-1}\right) \cdot \rho_{T[D]} \sigma_T \sigma_{[D]} + 2\left(qm \cdot exp\left(\frac{2B}{T}\right) p^{2m-1} \varphi^{2n} [D]^{2q-1}\right) \cdot \rho_{p[D]} \sigma_p \sigma_{[D]}\end{array}} \quad (23)$$

$$\rho_{ij} \sigma_i \sigma_j = \sigma_{ij} = \sum_{ij} f(i,j)(x_i - \bar{x_\iota})(x_j - \bar{x_J}) \quad (24)$$

The uncertainty of the measured ignition delay time in shock–tube could be acceptably estimated using the above equation. As seen in the above expression, the uncertainty parameter is changing by changing in the compressed temperature and pressure, equivalence ratio, and also diluent concentration, so that it is not a constant parameter during experimental tests. Thus, it should be calculated specifically for each case. Therefore, regarding Equation 23 and Table S9 , specific uncertainty for each data–point according to its specific temperature, pressure, equivalence ratio, and diluent concentration could be calculated as shown in Table S10 to Table S19.

Table S9. Correlation variables of the studied experimental datasets for different fuels.

$\tau_{IDT} = 10^A \cdot exp\left(\frac{B}{T}\right) p^m \varphi^n [D]^q$							
Fuel	A	B	m	n	q	R^2	Adj R^2
C_2H_4	24.42832	4173.61647	–7.45375	0.04535	7.13584	0.9709	0.96927
C_2H_6	13.35269	9724.30442	–5.42291	0.11308	4.81091	0.9085	0.90408

Table S10. Estimated uncertainties for all measured IDTs of P2C2 dataset in shock–tube.

T_5 (K)	φ	$\pm\sigma_\varphi$	p_5 (bar)	$\pm\sigma_p$ (bar)	$\pm\sigma_T$ (K)	[D] $\frac{mol}{10^5 \cdot m^3}$	$\pm\sigma_{[D]}$ $\frac{mol}{10^5 \cdot m^3}$	IDT (μs)	$\pm\sigma_{IDT}$ (μs)	$\pm\sigma_{IDT}$ (%)

1112.8	1.0	8.4E-03	20.75	0.3934	14.06	1.68E-3	3.83E-5	325	60.90	18.7
1084.3	1.0	8.4E-03	19.64	0.3736	13.49	1.63E-3	3.71E-5	447	81.71	18.3
1042.8	1.0	8.4E-03	19.71	0.3801	12.57	1.71E-3	3.88E-5	847.40	130.86	15.4

Table S11. Estimated uncertainties for all measured IDTs of P2C3 dataset in shock tube.

T_5 (K)	φ	$\pm\sigma_\varphi$	p_5 (bar)	$\pm\sigma_p$ (bar)	$\pm\sigma_T$ (K)	[D] $\frac{mol}{10^5 \cdot m^3}$	$\pm\sigma_{[D]}$ $\frac{mol}{10^5 \cdot m^3}$	IDT (μs)	$\pm\sigma_{IDT}$ (μs)	$\pm\sigma_{IDT}$ (%)
1245.9	2.0	9.8E-03	39.73	0.7673	17.87	2.88E-3	6.92E-5	49.6	16.69	33.6
1201.6	2.0	9.8E-03	40.12	0.7774	16.76	3.01E-3	7.19E-5	72.4	24.03	33.2
1154.4	2.0	9.8E-03	40.34	0.7831	15.58	3.15E-3	7.45E-5	130.6	36.68	28.1
1104.5	2.0	9.8E-03	40.38	0.7839	14.37	3.3E-3	7.71E-5	227.6	59.44	26.1
1050	2.0	9.8E-03	40.01	0.7872	13.33	3.44E-3	8.05E-5	389.2	105.14	27
1000.2	2.0	9.8E-03	40.04	0.8308	12.88	3.61E-3	8.82E-5	855.8	188.33	22
945.2	0.2	9.8E-03	39.55	0.7727	10.96	3.77E-3	8.58E-5	1686	338.42	20.1

Table S12. Estimated uncertainties for all measured IDTs of P2C5 dataset in shock–tube.

T_5 (K)	φ	$\pm\sigma_\varphi$	p_5 (bar)	$\pm\sigma_p$ (bar)	$\pm\sigma_T$ (K)	[D] $\frac{mol}{10^5 \cdot m^3}$	$\pm\sigma_{[D]}$ $\frac{mol}{10^5 \cdot m^3}$	IDT (μs)	$\pm\sigma_{IDT}$ (μs)	$\pm\sigma_{IDT}$ (%)
1152.1	1.0	8.3E-03	40.16	0.7848	14.35	3.56E-3	8.26E-5	225.8	87.18	38.6
1102.4	1.0	8.3E-03	40.20	0.7811	13.30	3.73E-3	8.53E-5	418.6	141.16	33.7
1054.6	1.0	8.3E-03	40.39	0.7859	12.35	3.91E-3	8.89E-5	816.2	226.50	27.8

Table S13. Estimated uncertainties for all measured IDTs of P2C7 dataset in shock–tube.

T_5 (K)	φ	$\pm\sigma_\varphi$	p_5 (bar)	$\pm\sigma_p$ (bar)	$\pm\sigma_T$ (K)	[D] $\frac{mol}{10^5 \cdot m^3}$	$\pm\sigma_{[D]}$ $\frac{mol}{10^5 \cdot m^3}$	IDT (μs)	$\pm\sigma_{IDT}$ (μs)	$\pm\sigma_{IDT}$ (%)
1201.5	0.5	7.74E-03	40.10	0.8022	15.24	3.61E-3	8.56E-5	260	84.99	32.7
1132.7	0.5	7.74E-03	38.81	0.8194	14.58	3.71E-3	9.17E-5	535	171.29	32.0

1107.9	0.5	7.74E-03	40.95	0.8534	14.01	4E-3	9.75E-5	827.68	210.51	25.4

Table S14. Estimated uncertainties for all measured IDTs of P3C2 dataset in shock–tube.

T_5 (K)	φ	$\pm\sigma_\varphi$	p_5 (bar)	$\pm\sigma_p$ (bar)	$\pm\sigma_T$ (K)	[D] $\frac{mol}{10^5 \cdot m^3}$	$\pm\sigma_{[D]}$ $\frac{mol}{10^5 \cdot m^3}$	IDT (μs)	$\pm\sigma_{IDT}$ (μs)	$\pm\sigma_{IDT}$ (%)
1390.4	1.0	8.28E-03	19.73	0.3843	21.07	1.28E-3	3.16E-5	24.8	5.49	22.1
1339	1.0	8.28E-03	19.67	0.382	19.69	1.33E-3	3.23E-5	37.8	8.72	23.1
1290.6	1.0	8.28E-03	19.71	0.3671	17.89	1.38E-3	3.20E-5	63	13.08	20.8
1253.4	1.0	8.28E-03	20.11	0.3914	17.54	1.45E-3	3.47E-5	100.4	19.28	19.2
1200.4	1.0	8.28E-03	20.02	0.3899	16.28	1.50E-3	3.57E-5	184.8	32.90	17.8
1154.5	1.0	8.28E-03	20.17	0.396	15.12	1.58E-3	3.72E-5	337	55.94	16.6
1097.2	1.0	8.28E-03	19.89	0.392	13.89	1.64E-3	3.83E-5	657.4	112.54	17.1

Table S15. Estimated uncertainties for all measured IDTs of P3C3 dataset in shock–tube.

T_5 (K)	φ	$\pm\sigma_\varphi$	p_5 (bar)	$\pm\sigma_p$ (bar)	$\pm\sigma_T$ (K)	[D] $\frac{mol}{10^5 \cdot m^3}$	$\pm\sigma_{[D]}$ $\frac{mol}{10^5 \cdot m^3}$	IDT (μs)	$\pm\sigma_{IDT}$ (μs)	$\pm\sigma_{IDT}$ (%)
1348.2	2.0	9.3E-03	39.89	0.767	21.05	2.67E-3	6.61E-5	27.4	5.88	21.5
1295.4	2.0	9.3E-03	39.70	0.7644	19.66	2.76E-3	6.78E-5	40.6	9.51	23.4
1247.0	2.0	9.3E-03	39.80	0.7630	18.19	2.88E-3	6.94E-5	67.2	15.33	22.8
1201.2	2.0	9.3E-03	40.09	0.7711	17.16	3.01E-3	7.21E-5	100.6	24.68	24.5
1148.5	2.0	9.3E-03	39.88	0.7732	15.77	3.13E-3	7.44E-5	177	44.54	25.2
1099.7	2.0	9.3E-03	39.98	0.7715	14.57	3.28E-3	7.68E-5	330.4	80.08	24.2
1048.7	2.0	9.3E-03	39.89	0.7746	13.38	3.43E-3	7.97E-5	640.2	155.30	24.6
997.5	2.0	9.3E-03	39.77	0.7678	12.17	3.6E-3	8.21E-5	1290	319.95	24.8

Table S16. Estimated uncertainties for all measured IDTs of P3C4 dataset in shock–tube.

T_5 (K)	φ	$\pm\sigma_\varphi$	p_5 (bar)	$\pm\sigma_p$ (bar)	$\pm\sigma_T$ (K)	[D] $\frac{mol}{10^5 \cdot m^3}$	$\pm\sigma_{[D]}$ $\frac{mol}{10^5 \cdot m^3}$	IDT (μs)	$\pm\sigma_{IDT}$ (μs)	$\pm\sigma_{IDT}$ (%)
1390.1	0.5	7.6E-03	19.75	0.3843	19.24	1.45E-3	3.47E-5	30.8	8.86	28.8
1348.7	0.5	7.6E-03	19.97	0.3952	18.33	1.51E-3	3.63E-5	47.8	12.78	26.7
1301.4	0.5	7.6E-03	20.05	0.3884	17.26	1.58E-3	3.70E-5	88.2	19.94	22.6
1245.9	0.5	7.6E-03	19.87	0.3834	16.04	1.63E-3	3.78E-5	180	33.90	18.8
1204.5	0.5	7.6E-03	20.14	0.3933	15.19	1.71E-3	3.97E-5	310.6	52.41	16.9
1152.6	0.5	7.6E-03	20.09	0.3904	14.08	1.78E-3	4.09E-5	653.2	92.54	14.2
1107.2	0.5	7.6E-03	20.27	0.3957	13.18	1.87E-3	4.28E-5	1130	158.84	14.1

Table S17. Estimated uncertainties for all measured IDTs of P3C5 dataset in shock–tube.

T_5 (K)	φ	$\pm\sigma_\varphi$	p_5 (bar)	$\pm\sigma_p$ (bar)	$\pm\sigma_T$ (K)	[D] $\frac{mol}{10^5 \cdot m^3}$	$\pm\sigma_{[D]}$ $\frac{mol}{10^5 \cdot m^3}$	IDT (μs)	$\pm\sigma_{IDT}$ (μs)	$\pm\sigma_{IDT}$ (%)
1394.6	1.0	8.2E-03	39.70	0.7711	19.86	2.91E-3	7.01E-5	25.4	6.13	24.1
1360.3	1.0	8.2E-03	40.60	0.7919	19.05	3.05E-3	7.33E-5	34.6	8.15	23.6
1300.1	1.0	8.2E-03	40.01	0.7762	17.63	3.15E-3	7.45E-5	63.6	14.29	22.5
1244.8	1.0	8.2E-03	39.67	0.771	16.42	3.26E-3	7.65E-5	107	24.68	23.1
1199.2	1.0	8.2E-03	39.95	0.775	15.36	3.41E-3	7.92E-5	186.4	39.66	21.3
1150.4	1.0	8.2E-03	40.05	0.7779	14.32	3.56E-3	8.21E-5	333	68.09	20.5
1102.4	1.0	8.2E-03	40.19	0.7796	13.33	3.73E-3	8.52E-5	596	120.86	20.3

Table S18. Estimated uncertainties for all measured IDTs of P3C7 dataset in shock–tube.

T_5 (K)	φ	$\pm\sigma_\varphi$	p_5 (bar)	$\pm\sigma_p$ (bar)	$\pm\sigma_T$ (K)	[D] $\frac{mol}{10^5 \cdot m^3}$	$\pm\sigma_{[D]}$ $\frac{mol}{10^5 \cdot m^3}$	IDT (μs)	$\pm\sigma_{IDT}$ (μs)	$\pm\sigma_{IDT}$ (%)
1558	0.5	7.6E-03	40.41	0.8625	24.56	2.81E-3	7.45E-5	6.64	2.27	34.2
1506.9	0.5	7.6E-03	40.34	0.8503	23.25	2.9E-3	7.57E-5	10.80	3.28	30.4
1452.3	0.5	7.6E-03	40.12	0.8438	21.91	2.99E-3	7.74E-5	18.69	4.99	26.7

1393.7	0.5	7.6E-03	39.67	0.8382	20.49	3.08E-3	7.93E-5	30.98	8.14	26.3
1344.6	0.5	7.6E-03	39.71	0.8369	19.33	3.20E-3	8.16E-5	51.7	12.56	24.3
1298.6	0.5	7.6E-03	39.92	0.8405	18.21	3.33E-3	8.42E-5	77.31	19.11	24.7
1243.8	0.5	7.6E-03	39.62	0.8416	17.06	3.45E-3	8.72E-5	151.84	33.15	21.8
1202	0.5	7.6E-03	40.14	0.8452	16.09	3.61E-3	9.02E-5	324.29	50.29	15.5
1154.3	0.5	7.6E-03	40.31	0.8484	15.01	3.78E-3	9.35E-5	622.14	85.79	13.8
1101.6	0.5	7.6E-03	40.13	0.8464	13.93	3.94E-3	9.70E-5	1189	161.54	13.6

Table S19. Estimated uncertainties for all measured IDTs of P3C9 dataset in shock–tube.

T_5 (K)	φ	$\pm\sigma_\varphi$	p_5 (bar)	$\pm\sigma_p$ (bar)	$\pm\sigma_T$ (K)	[D] $\frac{mol}{10^5 \cdot m^3}$	$\pm\sigma_{[D]}$ $\frac{mol}{10^5 \cdot m^3}$	IDT (μs)	$\pm\sigma_{IDT}$ (μs)	$\pm\sigma_{IDT}$ (%)
1692.6	2.0	9.5E-03	19.84	0.4075	29.81	1.27E-3	3.43E-5	16.46	1.7	10.3
1643.4	2.0	9.5E-03	19.85	0.4154	28.27	1.31E-3	3.54E-5	21.12	2.34	11.1
1591.6	2.0	9.5E-03	19.81	0.4234	26.76	1.35E-3	3.66E-5	26.25	3.36	12.8
1552.7	2.0	9.5E-03	20.06	0.4194	25.66	1.4E-3	3.73E-5	29.29	4.30	14.7
1501.0	2.0	9.5E-03	20.03	0.4228	24.26	1.44E-3	3.84E-5	36.80	6.21	16.9
1453.4	2.0	9.5E-03	20.09	0.4242	22.94	1.5E-3	3.94E-5	46.97	9.19	19.6
1397.7	2.0	9.5E-03	19.94	0.4187	21.48	1.54E-3	4.02E-5	71.24	14.19	19.9
1351.7	2.0	9.5E-03	20.05	0.4169	20.34	1.61E-3	4.12E-5	105.6	21.50	20.4
1292.2	2.0	9.5E-03	19.76	0.4143	18.86	1.66E-3	4.22E-5	151.67	37.76	24.9
1254.6	2.0	9.5E-03	20.15	0.4212	17.93	1.74E-3	4.40E-5	207.49	53.42	25.7
1199.1	2.0	9.5E-03	19.97	0.4212	16.58	1.8E-3	4.55E-5	413.04	95.19	23.0
1155.1	2.0	9.5E-03	20.19	0.4179	15.31	1.89E-3	4.65E-5	650.03	152.33	23.4

8.4 Rapid compression machine

As shown in the previous section, the uncertainty of each experimental point is changing by varying temperature, pressure, and mixture composition, so that it is not identical during IDT measurement experimental tests. Therefore, for doing the uncertainty analysis for the studied RCM regimes, P2C7

dataset has been chosen as one of the worst cases with high uncertainty. As already mentioned by Weber et al [25], using Monte Carlo analysis or independent parameters methodology doesn't led to significant change in the calculated uncertainties. Therefore, like the performed uncertainty analysis for NUIG–HPST, it is supposed that there is no correlation between parameters which can affect measured ignition delay time in the rapid compression machine. In this regard, the average temperature of dataset in RCM regime is calculated as representative of the studied temperature range, and then the uncertainty analysis has been done for the test point. The average temperature for P2C7 dataset is 918.4 K. Here, it should be noted that according to the Taguchi DOE method, it is not possible to consider the effect of individual parameters such as pressure, equivalence ratio, and dilution percent on the measured ignition delay time, so that the physical and chemical conditions of each dataset is completely different and it is not comparable with another one in terms of the effect of individual parameter on the measured ignition delay times. Thus, for covering the lack of information in this part, adiabatic constant volume IDT simulations have been done at the average temperature over the studied range of equivalence ratio and dilution percent, individually, using AramcoMech 3.0 chemical mechanism due to its better compatibility with the experimental results of P2C7 dataset. As shown in Figure S14, the effect of temperature on the measured ignition delay time has been correlated through fitting an exponential equation to the experimental IDT data, and then the individual effect of pressure on the measured ignition delay time has been estimated using the applied approach by Weber et al [25]. Also, the effect of each individual parameter such as equivalence ratio (0.5–2.0) and dilution (75%–90%) on the simulated ignition delay times has been correlated using fitted power equations (Figure S15 and Figure S16) to the simulated ignition delay times. Therefore, the following formulations could be proposed to estimate available uncertainties in the measured independent parameters and consequently the measured ignition delay times:

$$\tau_{IDT}(T_c) = 6 \times 10^{13} \exp(-0.038T_c) \rightarrow \frac{\partial \tau_{IDT}}{\partial T_c} = -2.28 \times 10^{12} exp(-0.038T_c) \quad (25)$$

$$\tau_{IDT}(\varphi) = 0.0119x^{-0.68} \rightarrow \frac{\partial \tau_{IDT}}{\partial \varphi} = -8.092 \times 10^{-3} x^{-1.68} \quad (26)$$

$$\tau_{IDT}([D]) = 1 \times 10^{9} x^{4.6821} \rightarrow \frac{\partial \tau_{IDT}}{\partial [D]} = 4.6821 \times 10^{9} x^{3.6821} \quad (27)$$

$$\frac{\partial T_c}{\partial p_c} = \frac{W\left(\frac{b}{a} exp\left[\frac{bT_0}{a}\right] T_0 \left[\frac{p_c}{p_0}\right]^{\frac{1}{a}}\right)}{bp_c\left(W\left(\frac{b}{a} exp\left[\frac{bT_0}{a}\right] T_0 \left[\frac{p_c}{p_0}\right]^{\frac{1}{a}}\right)+1\right)} \quad (28)$$

Where, W, T_0, and p_0 are Lambert's W function, initial temperature, and initial pressure in the reaction chamber, respectively. In Equation 28, "a", "b", and $\frac{\partial T_c}{\partial P_c}$ were calculated using a Python code developed by Weber et al [25].

$$\frac{\partial \tau_{IDT}}{\partial p_c} = \frac{\partial \tau_{IDT}}{\partial T_c} \cdot \frac{\partial T_c}{\partial p_c} = \left(-2.28 \times 10^{12} exp(-0.038 T_c)\right) \cdot \frac{W\left(\frac{b}{a} exp\left[\frac{bT_0}{a}\right] T_0 \left[\frac{p_c}{p_0}\right]^{\frac{1}{a}}\right)}{bP_c\left(W\left(\frac{b}{a} exp\left[\frac{bT_0}{a}\right] T_0 \left[\frac{p_c}{p_0}\right]^{\frac{1}{a}}\right)+1\right)} \quad (29)$$

$$\tau_{IDT} = f(T_c, p_c, \varphi, [D]) \rightarrow \sigma_{\tau_{IDT}} = \sqrt{\left(\frac{\partial \tau_{IDT}}{\partial T_c} \cdot \sigma_{T_c}\right)^2 + \left(\frac{\partial \tau_{IDT}}{\partial p_c} \cdot \sigma_{p_c}\right)^2 + \left(\frac{\partial \tau_{IDT}}{\partial \varphi} \cdot \sigma_{\varphi}\right)^2 + \left(\frac{\partial \tau_{IDT}}{\partial [D]} \cdot \sigma_{[D]}\right)^2} \quad (30)$$

By substituting Equations 25–29 into Equation 30 and using average values for $\bar{\sigma}_{T_c} \approx \sigma_{\bar{T}_c}$ and $\overline{\frac{\partial T_c}{\partial p_c}} \approx \left.\frac{\partial T_c}{\partial p_c}\right|_{\bar{T}_c}$, the average uncertainty ($\bar{\sigma}_{IDT}$) of the measured ignition delay times in RCM regime for P2C7 dataset (as one of the studied cases with high uncertainty) at $\bar{T}_c = 918.4\ K$ would be calculated based on a Python code developed by Weber et al [25] as follows:

$\bar{\sigma}_{T_c} = 3.55\ K$

$$\bar{\sigma}_{\tau_{IDT}} = \sqrt{\begin{matrix}(-5.652628405 \times 10^{-3})^2 + (-2.572172296 \times 10^{-4})^2 \\ +(-2.193803353 \times 10^{-4})^2 + (3.354450762 \times 10^{-4})^2\end{matrix}} = \sqrt{3.217901972 \times 10^{-5}} = \pm 5.673\ ms \approx \pm 11\%$$

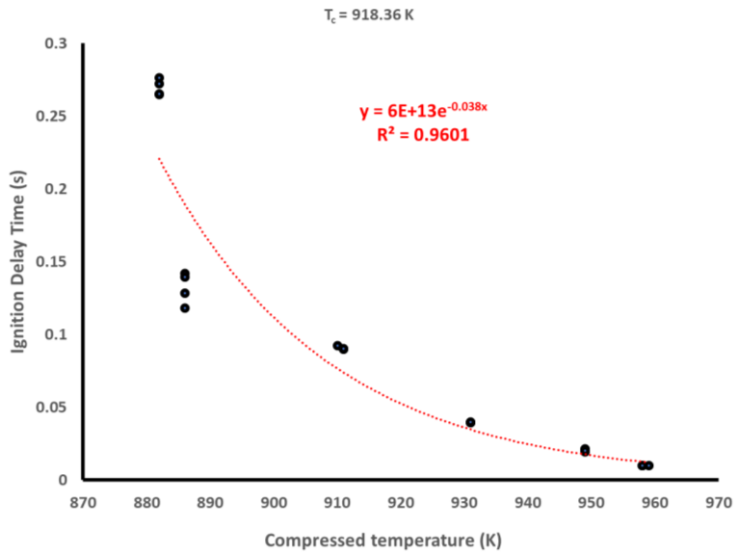

Figure S14. Correlating ignition delay time versus compressed temperature data using an exponential expression.

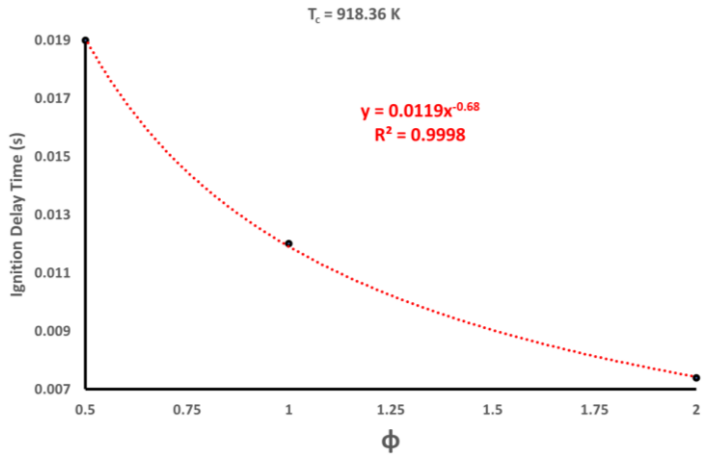

Figure S15. Correlating ignition delay time versus equivalence ratio at $\bar{T}_c = 918.36\ K$ using a power expression.

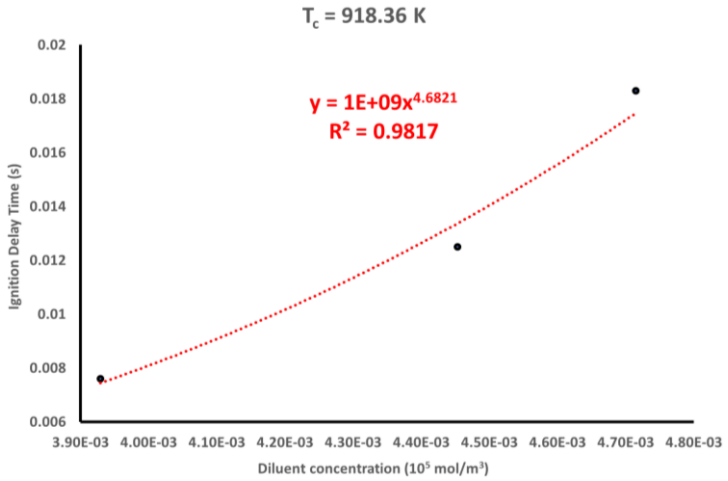

Figure S16. Correlating ignition delay time versus diluent concentration at $\bar{T}_c = 918.36\ K$ using a power expression.

9 NUIG Rapid Compression Machine Traces

In this section, the pressure histories of all tested reactive and non–reactive mixtures in NUIG–RCM alongside with their corresponding simulation's profile have been demonstrated in Figure S17 to Figure S79. All the simulations (sim_Reactive) have been carried out using AramcoMech 3.0 chemical mechanism, otherwise, it is mentioned in the caption or legend of each profile. Also, for covering the studied temperature range, the reaction chamber of NUIG–RCM has been heated–up from 30~110 ˚C for a specific test mixture. Otherwise, the diluent contents of the test mixtures have been changed (adding argon instead of nitrogen as a diluent to the test mixture) to achieve higher compressed temperatures.

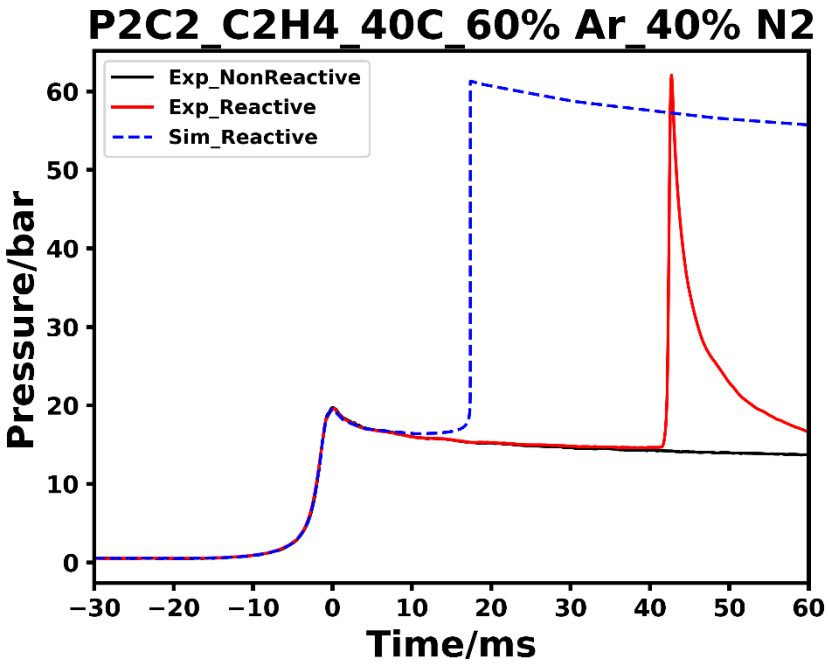

Figure S17. Pressure history of tested reactive and non–reactive mixtures of P2C2 case alongside the simulation's profile for initial temperature of 313 K.

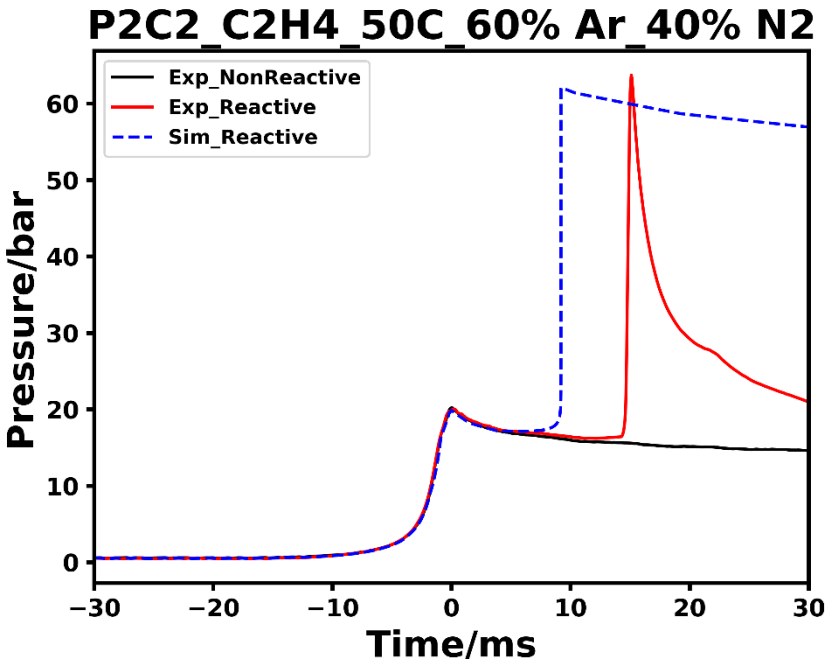

Figure S18. Pressure history of tested reactive and non–reactive mixtures of P2C2 case alongside the simulation's profile for initial temperature of 323 K.

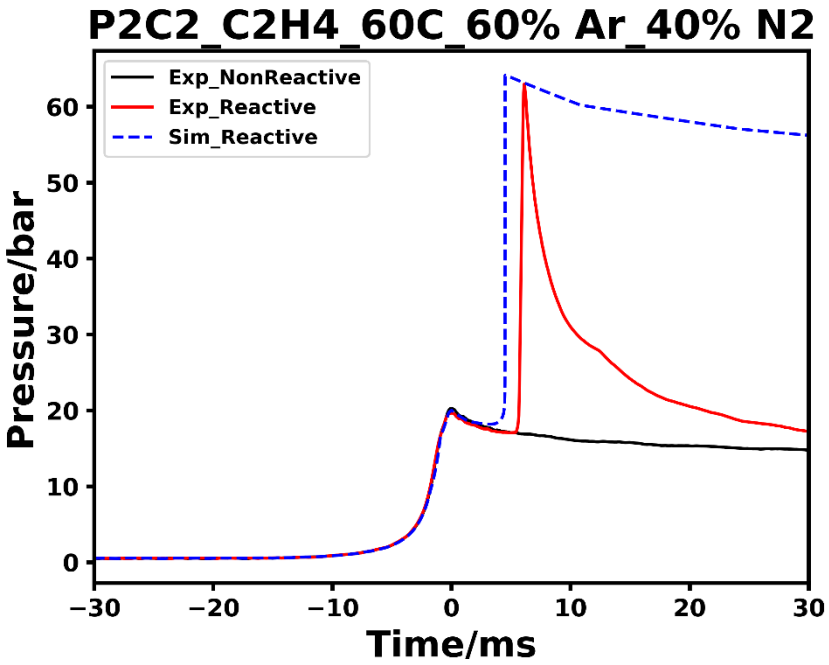

Figure S19. Pressure history of tested reactive and non–reactive mixtures of P2C2 case alongside the simulation's profile for initial temperature of 333 K.

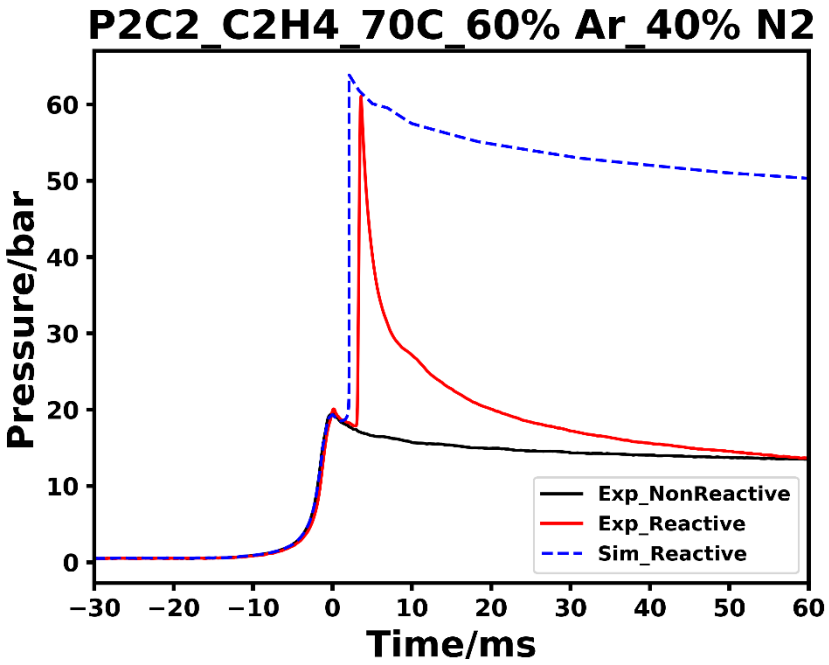

Figure S20. Pressure history of tested reactive and non–reactive mixtures of P2C2 case alongside the simulation's profile for initial temperature of 343 K.

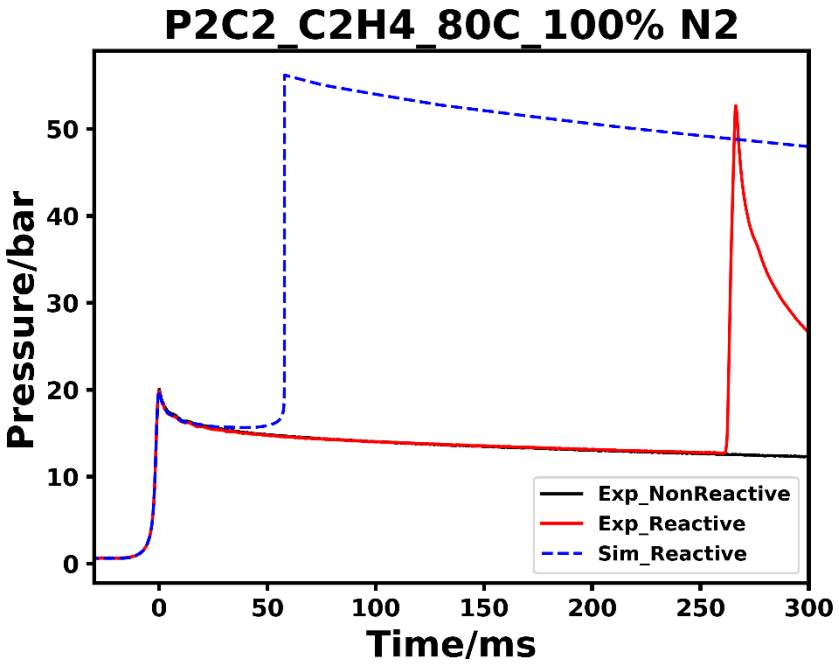

Figure S21. Pressure history of tested reactive and non–reactive mixtures of P2C2 case alongside the simulation's profile for initial temperature of 353 K.

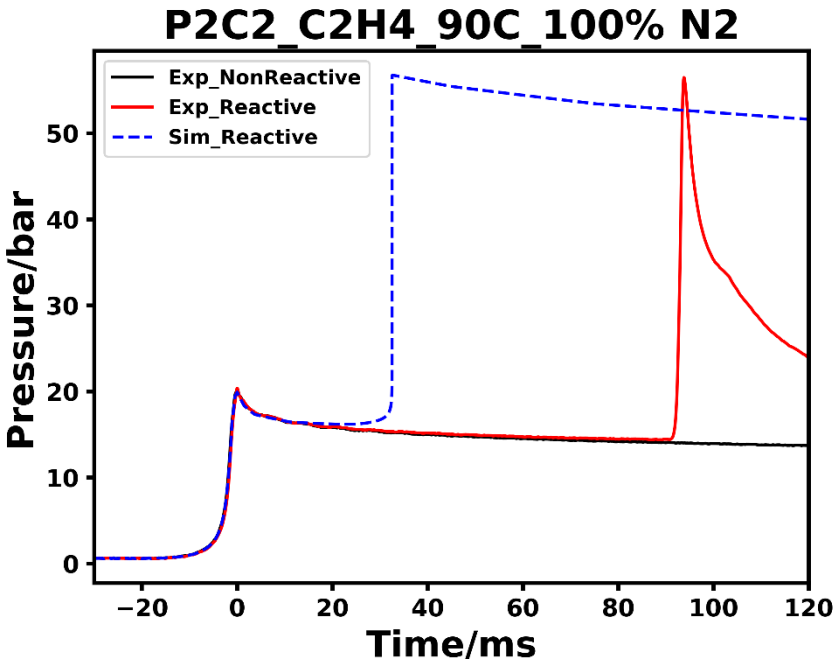

Figure S22. Pressure history of tested reactive and non–reactive mixtures of P2C2 case alongside the simulation's profile for initial temperature of 363 K.

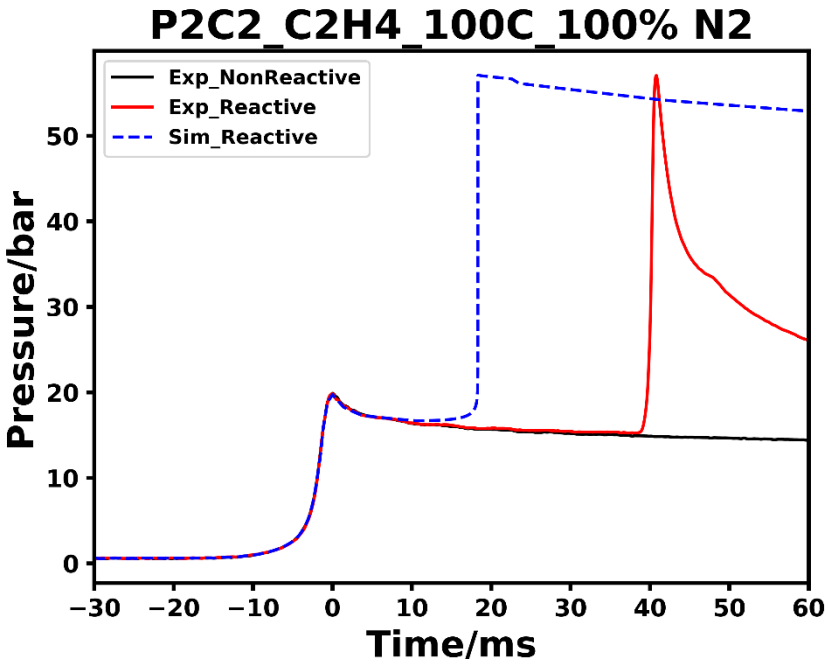

Figure S23. Pressure history of tested reactive and non–reactive mixtures of P2C2 case alongside the simulation's profile for initial temperature of 383 K.

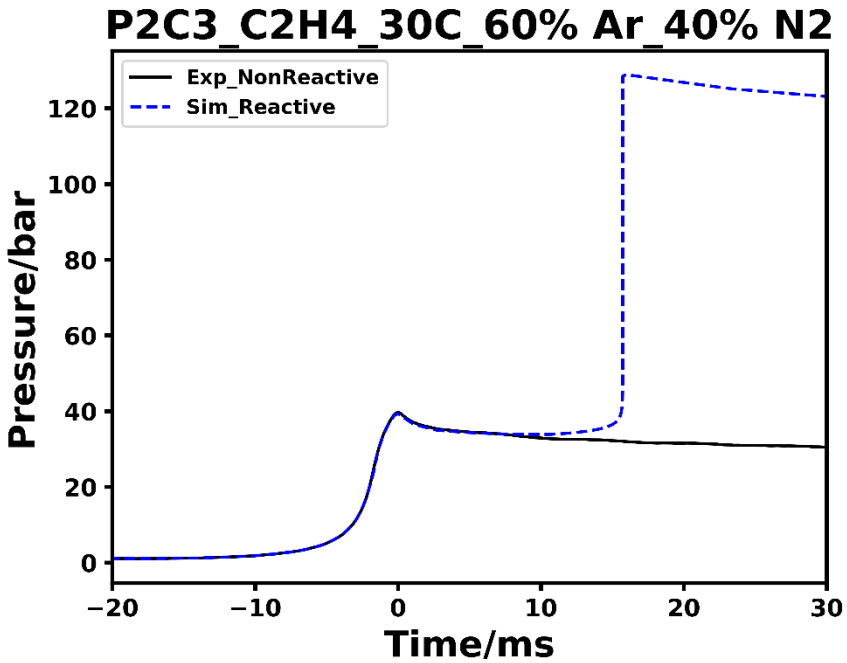

Figure S24. Pressure history of tested reactive and non–reactive mixtures of P2C3 case alongside the simulation's profile for initial temperature of 303 K.

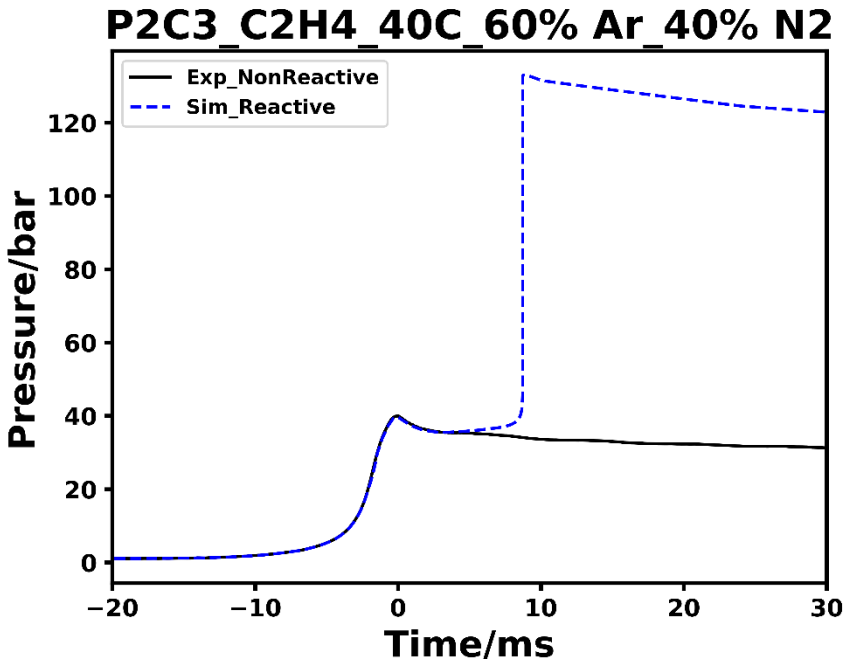

Figure S25. Pressure history of tested reactive and non–reactive mixtures of P2C3 case alongside the simulation's profile for initial temperature of 313 K.

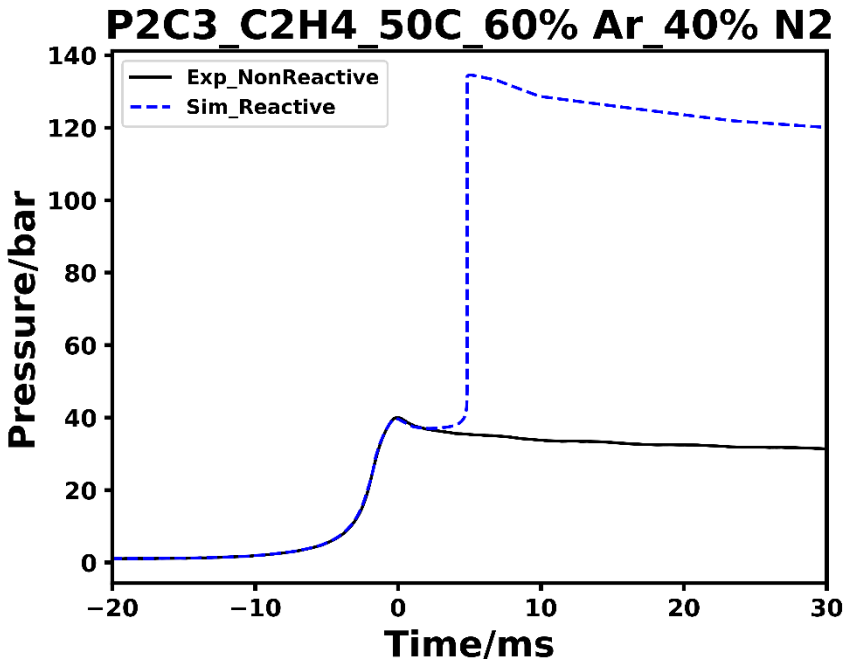

Figure S26. Pressure history of tested reactive and non–reactive mixtures of P2C3 case alongside the simulation's profile for initial temperature of 323 K.

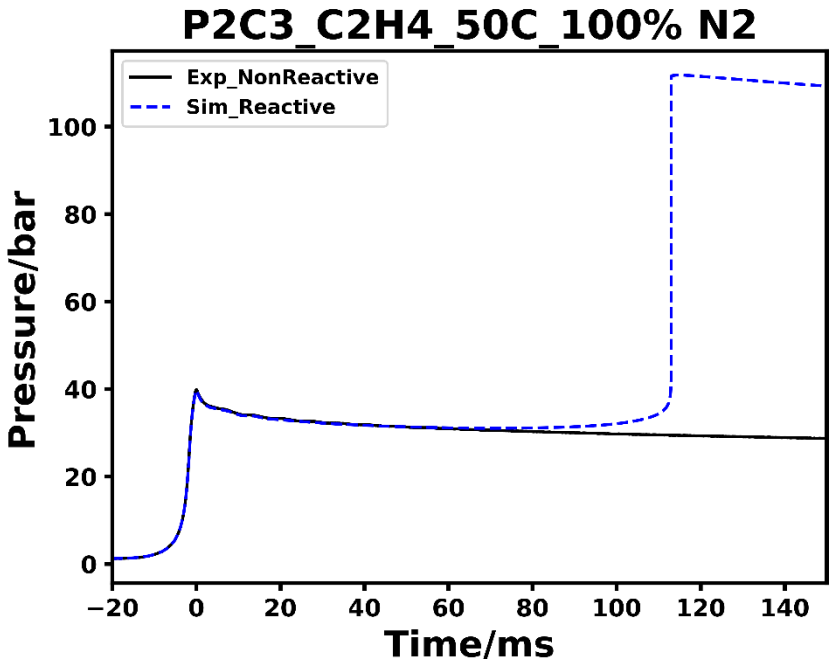

Figure S27. Pressure history of tested reactive and non–reactive mixtures of P2C3 case alongside the simulation's profile for initial temperature of 323 K.

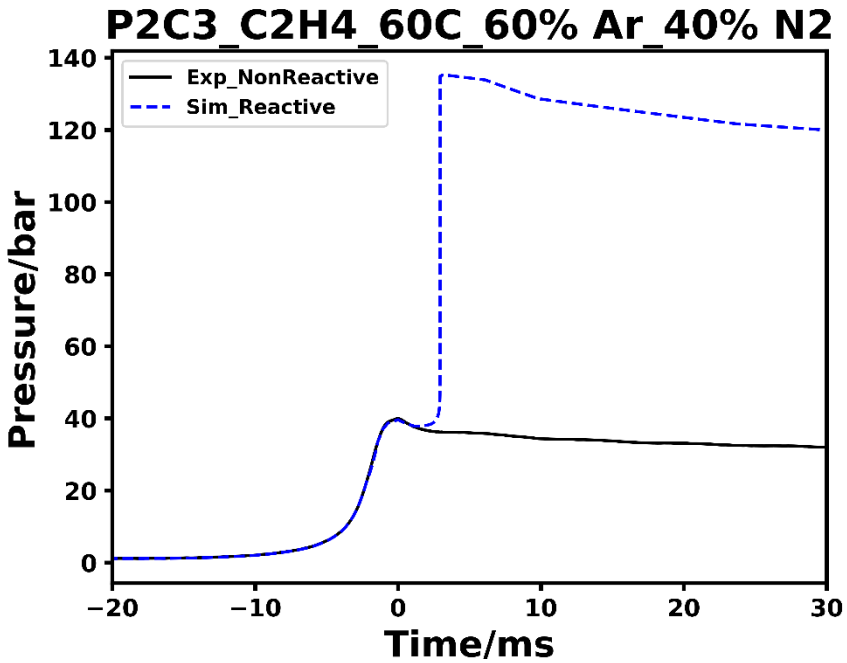

Figure S28. Pressure history of tested reactive and non–reactive mixtures of P2C2 case alongside the simulation's profile for initial temperature of 333 K.

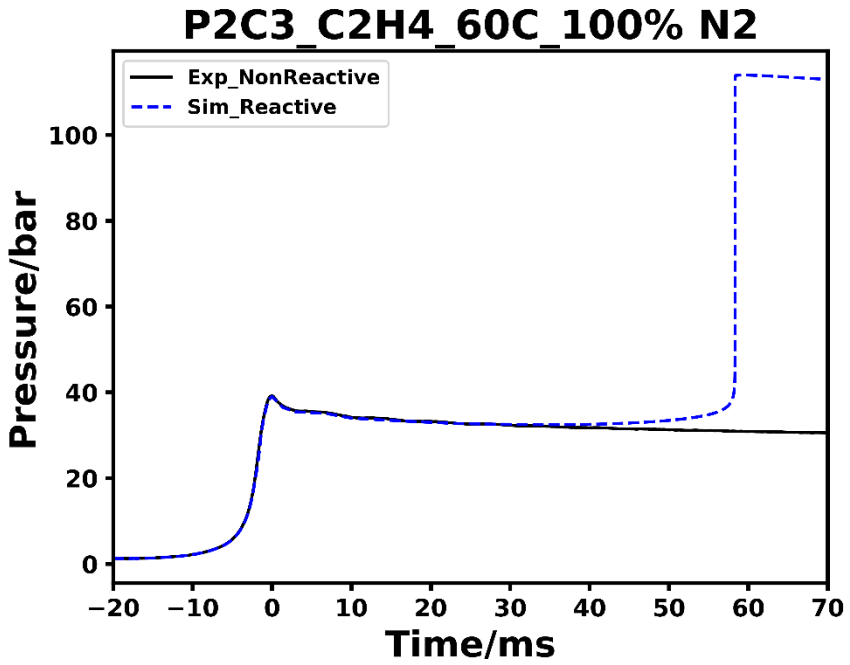

Figure S29. Pressure history of tested reactive and non–reactive mixtures of P2C3 case alongside the simulation's profile for initial temperature of 333 K (100% N_2).

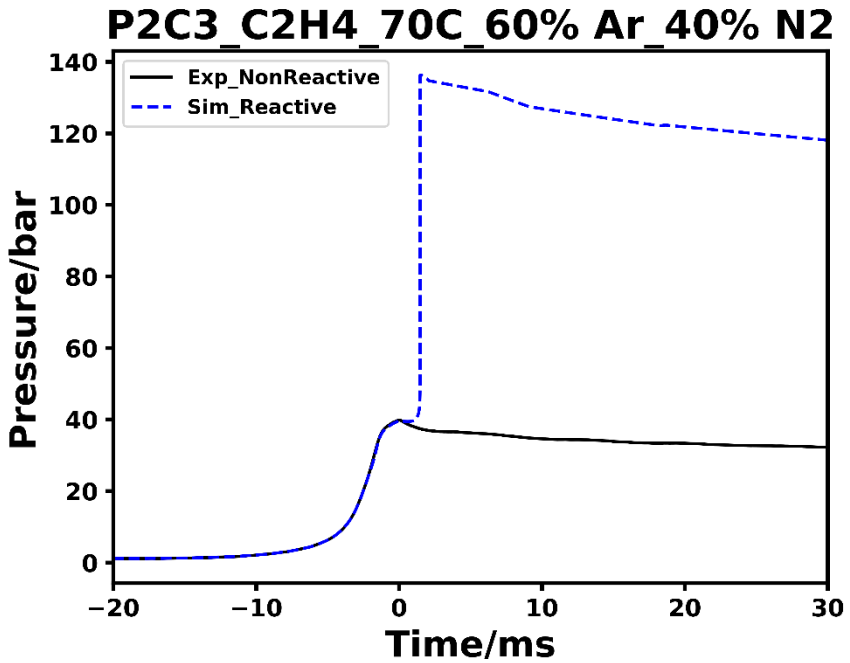

Figure S30. Pressure history of tested reactive and non–reactive mixtures of P2C3 case alongside the simulation's profile for initial temperature of 343 K.

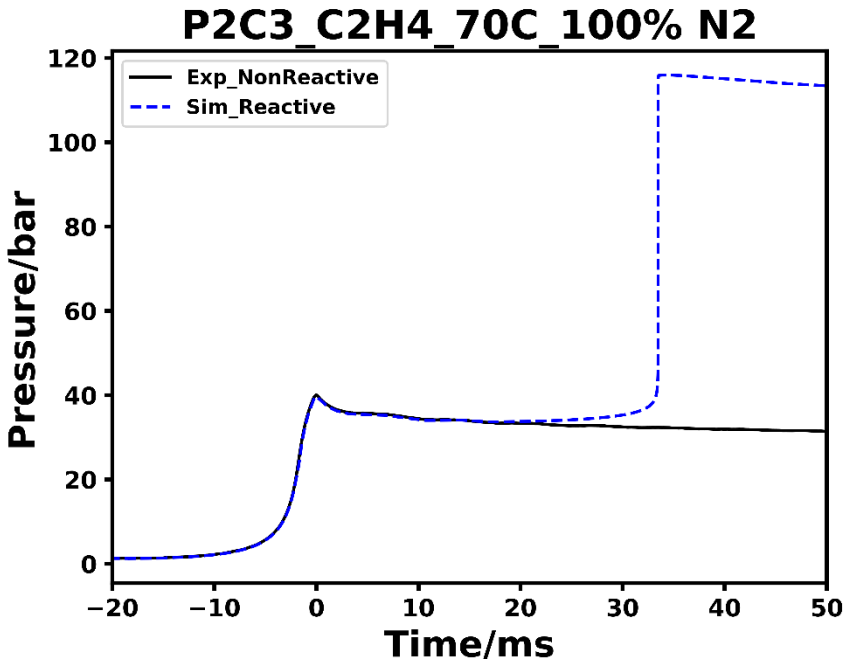

Figure S31. Pressure history of tested reactive and non–reactive mixtures of P2C3 case alongside the simulation's profile for initial temperature of 343 K.

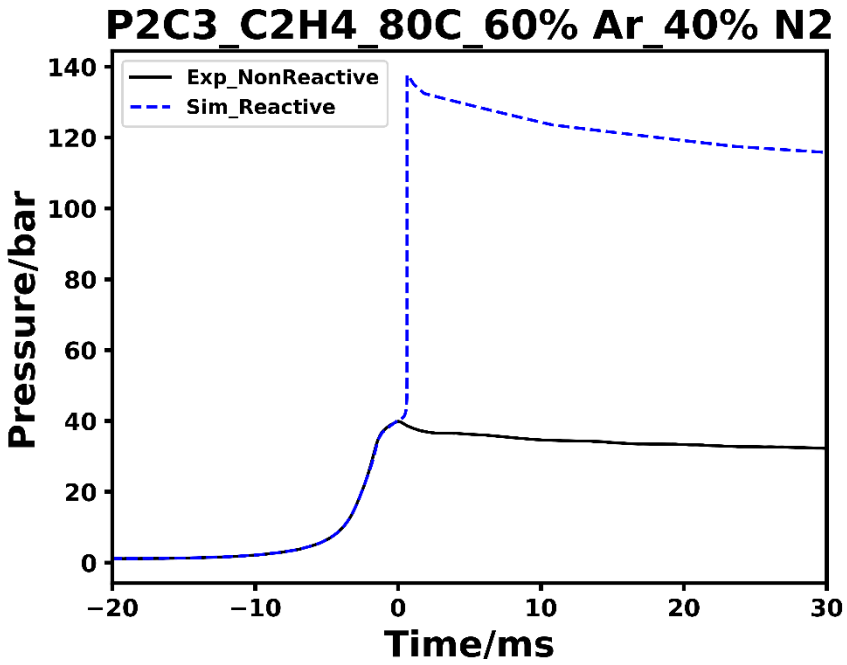

Figure S32. Pressure history of tested reactive and non–reactive mixtures of P2C3 case alongside the simulation's profile for initial temperature of 353 K.

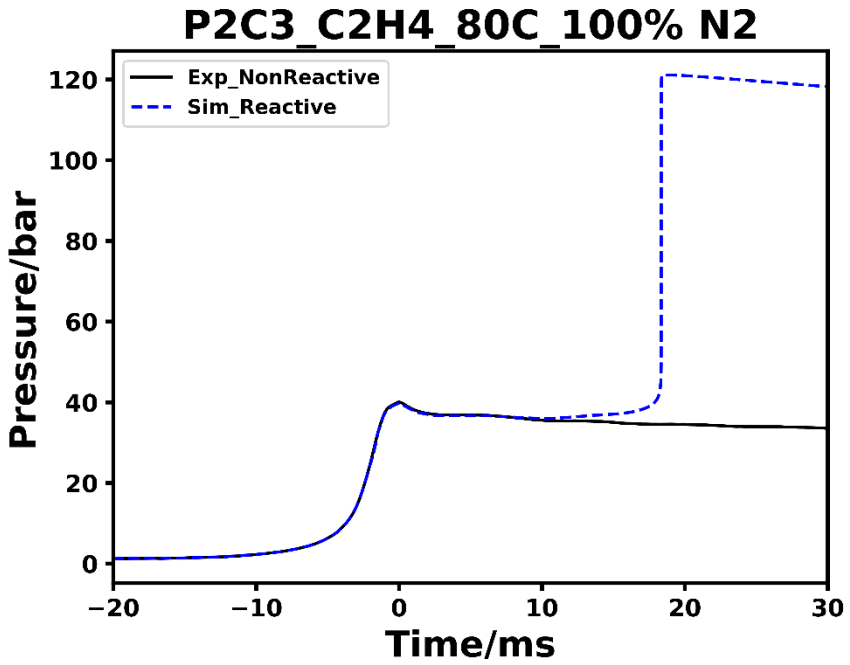

Figure S33. Pressure history of tested reactive and non–reactive mixtures of P2C3 case alongside the simulation's profile for initial temperature of 353 K (100% N_2).

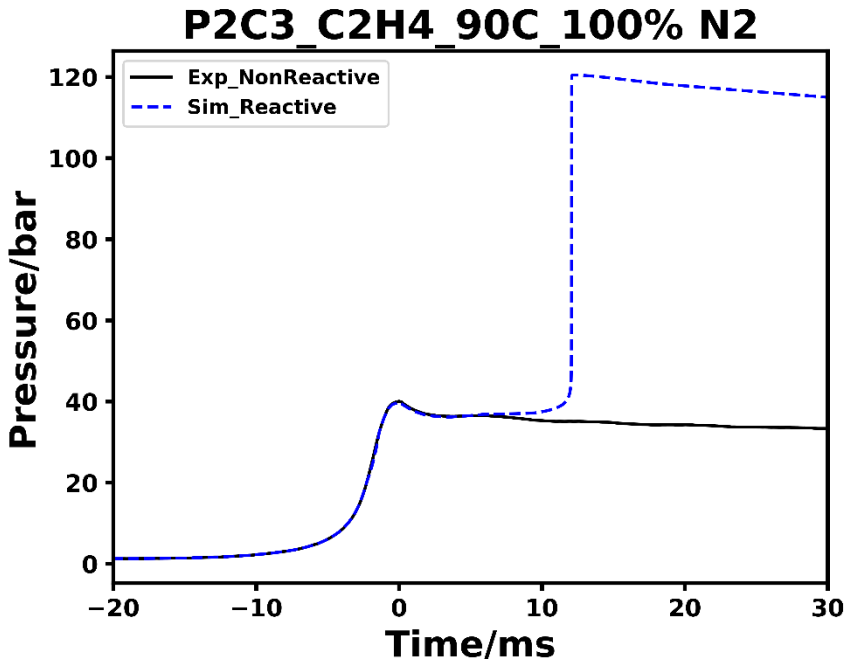

Figure S34. Pressure history of tested reactive and non–reactive mixtures of P2C3 case alongside the simulation's profile for initial temperature of 363 K.

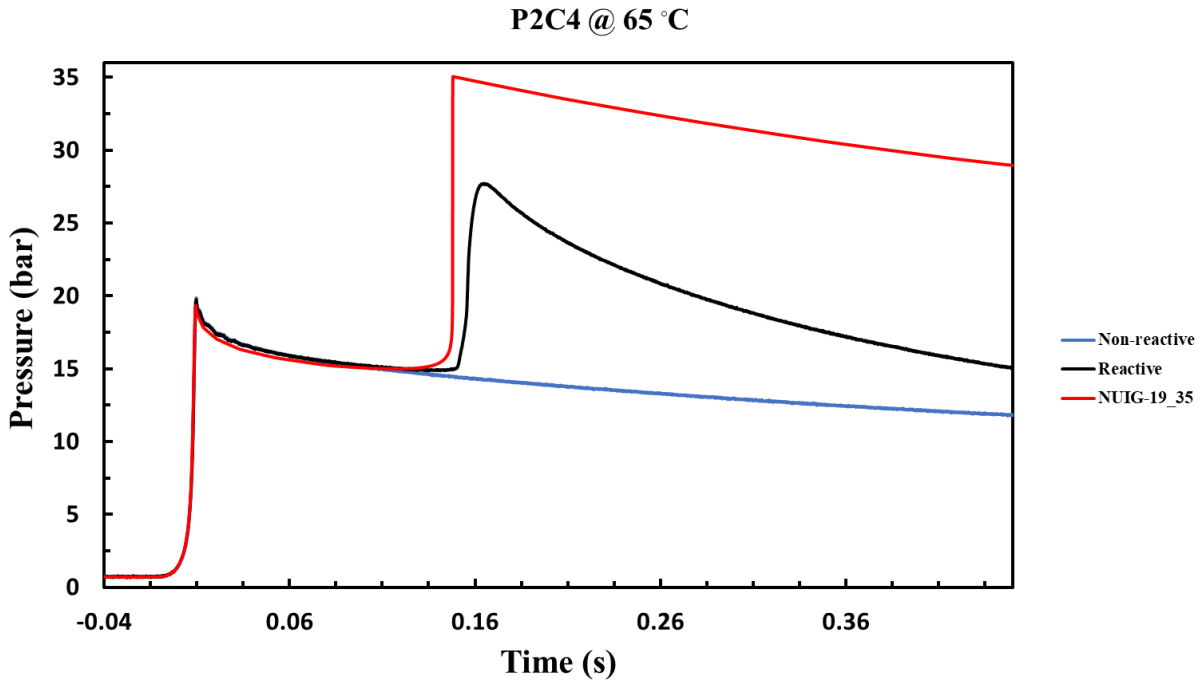

Figure S35. Pressure history of tested reactive and non–reactive mixtures of P2C4 case alongside the simulation's profile for initial temperature of 338 K.

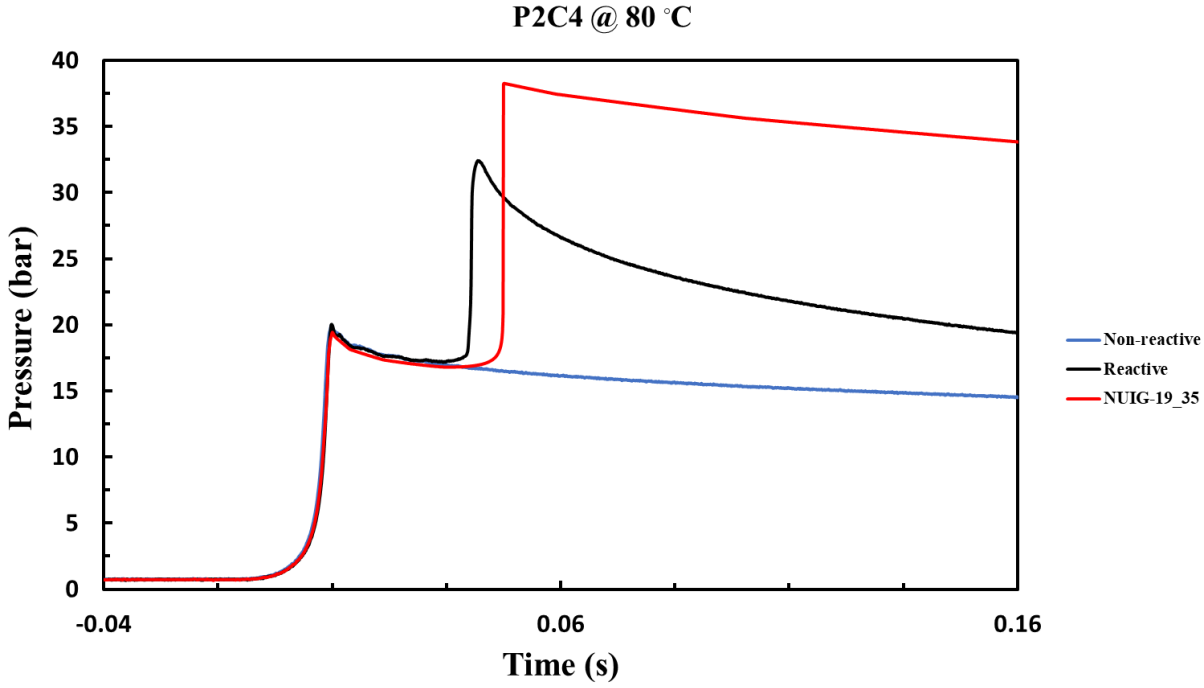

Figure S36. Pressure history of tested reactive and non–reactive mixtures of P2C4 case alongside the simulation's profile for initial temperature of 353 K.

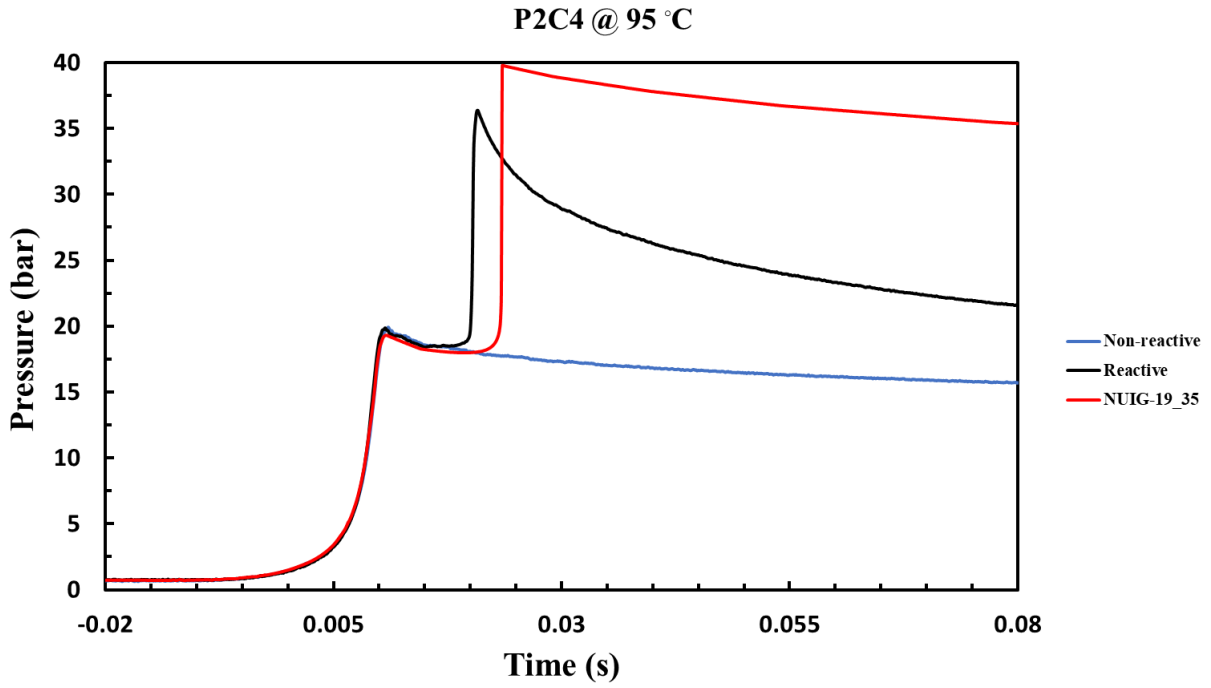

Figure S37. Pressure history of tested reactive and non–reactive mixtures of P2C4 case alongside the simulation's profile for initial temperature of 368 K.

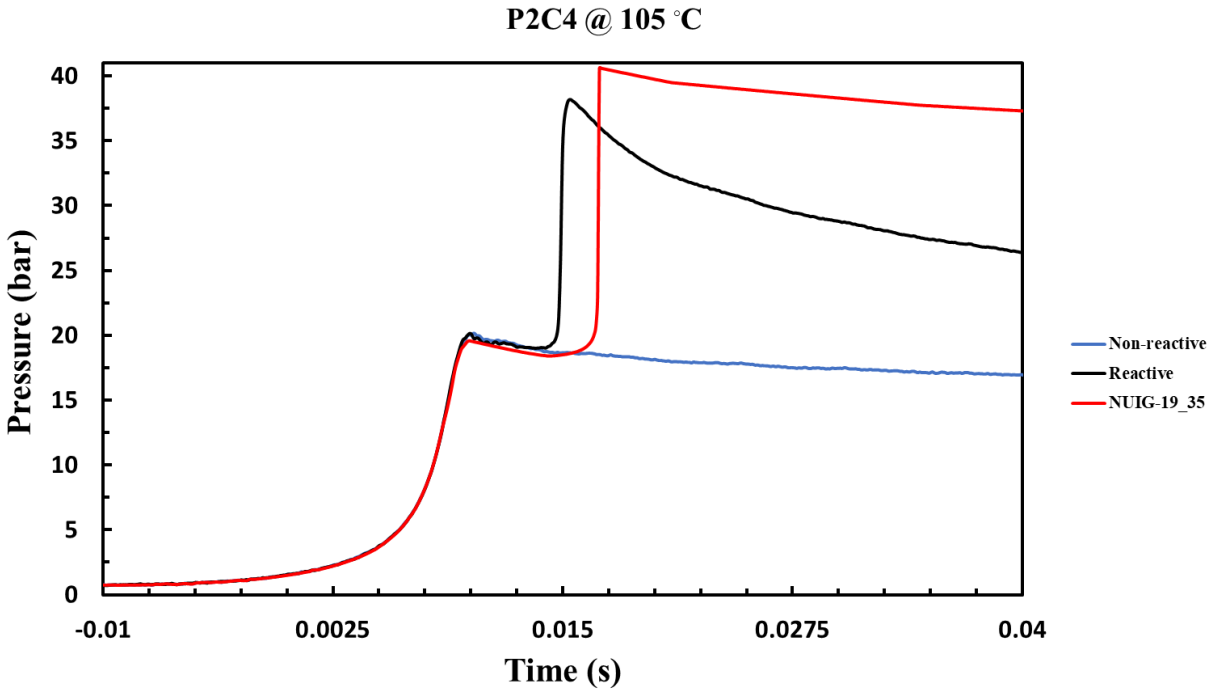

Figure S38. Pressure history of tested reactive and non–reactive mixtures of P2C4 case alongside the simulation's profile for initial temperature of 378 K.

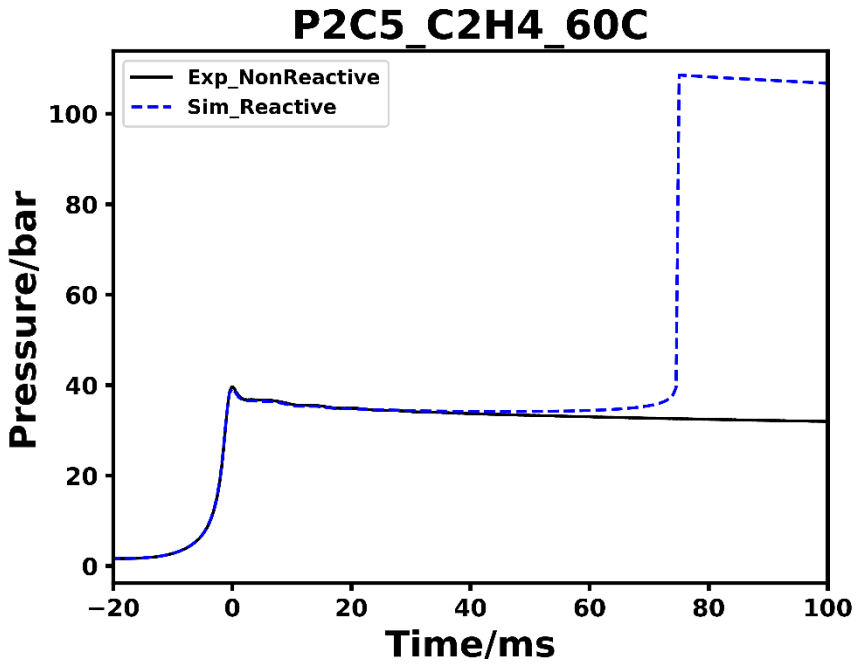

Figure S39. Pressure history of tested reactive and non–reactive mixtures of P2C5 case alongside the simulation's profile for initial temperature of 333 K.

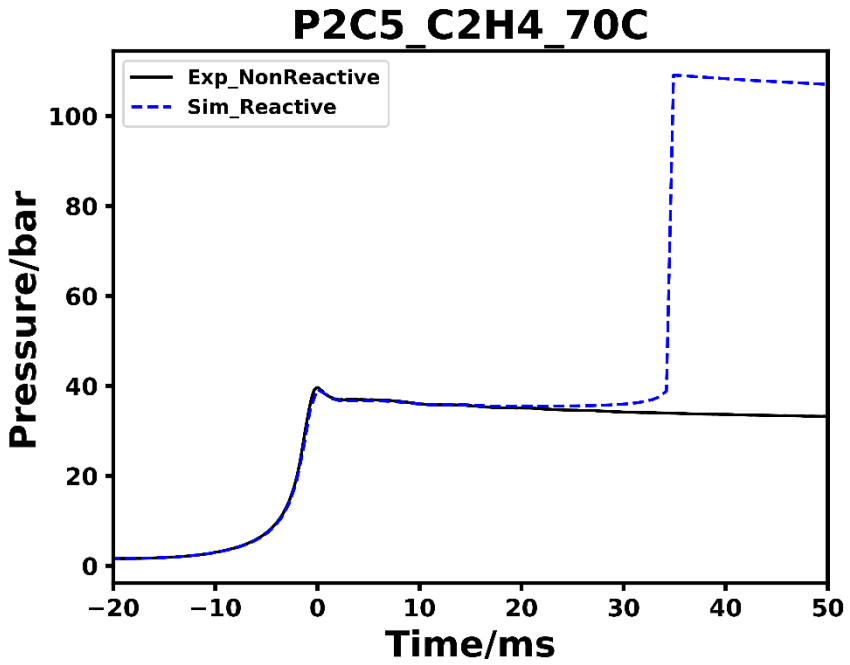

Figure S40. Pressure history of tested reactive and non–reactive mixtures of P2C5 case alongside the simulation's profile for initial temperature of 343 K.

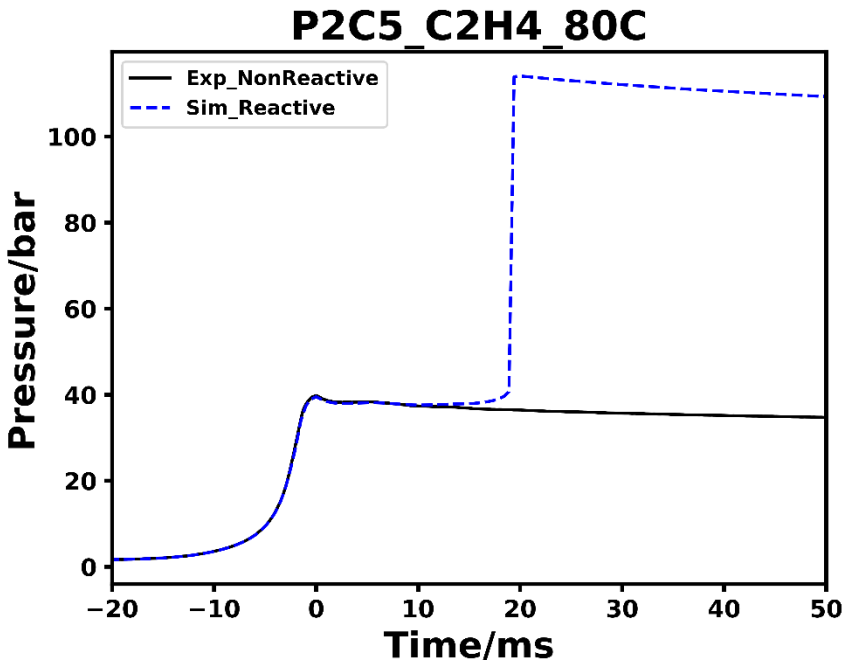

Figure S41. Pressure history of tested reactive and non–reactive mixtures of P2C5 case alongside the simulation's profile for initial temperature of 353 K.

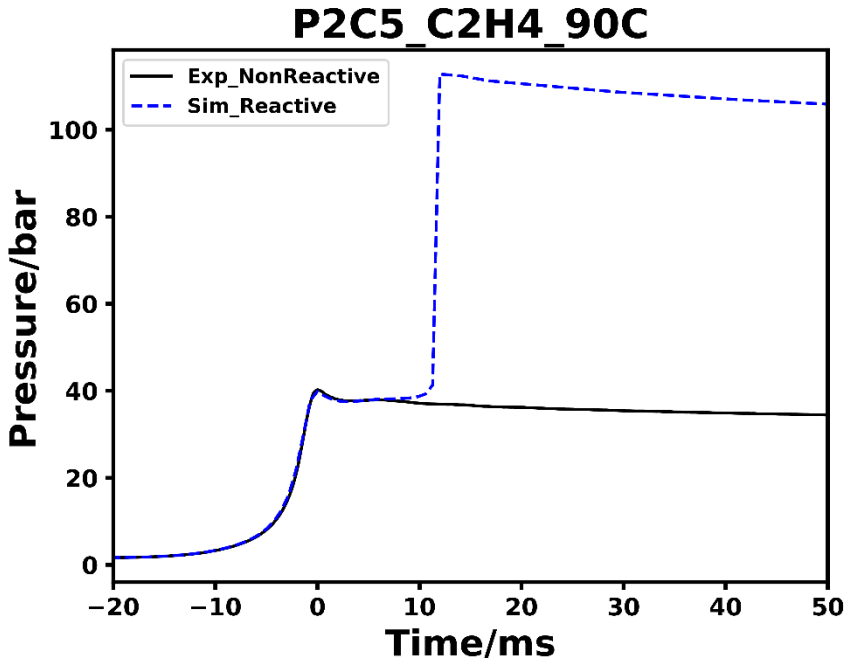

Figure S42. Pressure history of tested reactive and non–reactive mixtures of P2C5 case alongside the simulation's profile for initial temperature of 363 K.

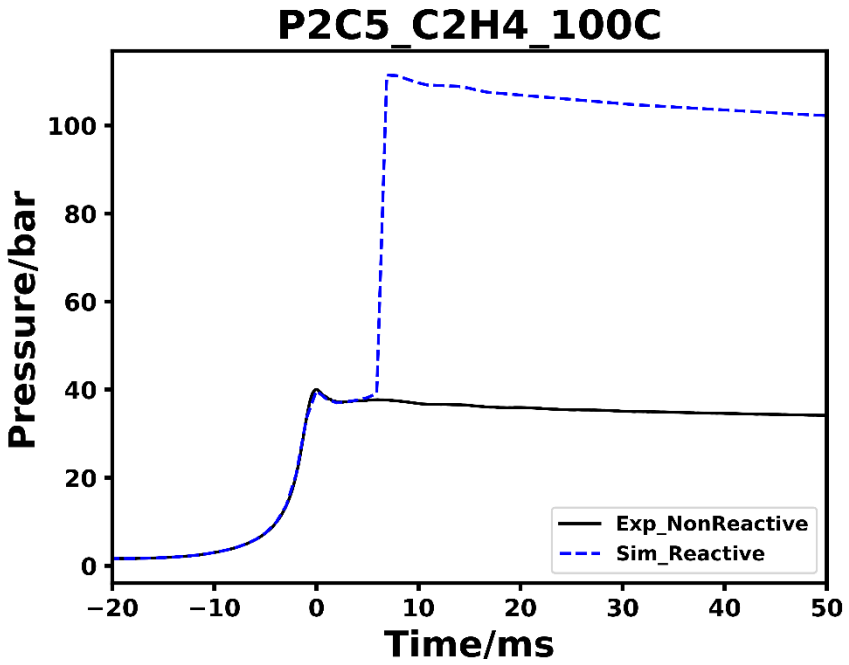

Figure S43. Pressure history of tested reactive and non–reactive mixtures of P2C5 case alongside the simulation's profile for initial temperature of 373 K.

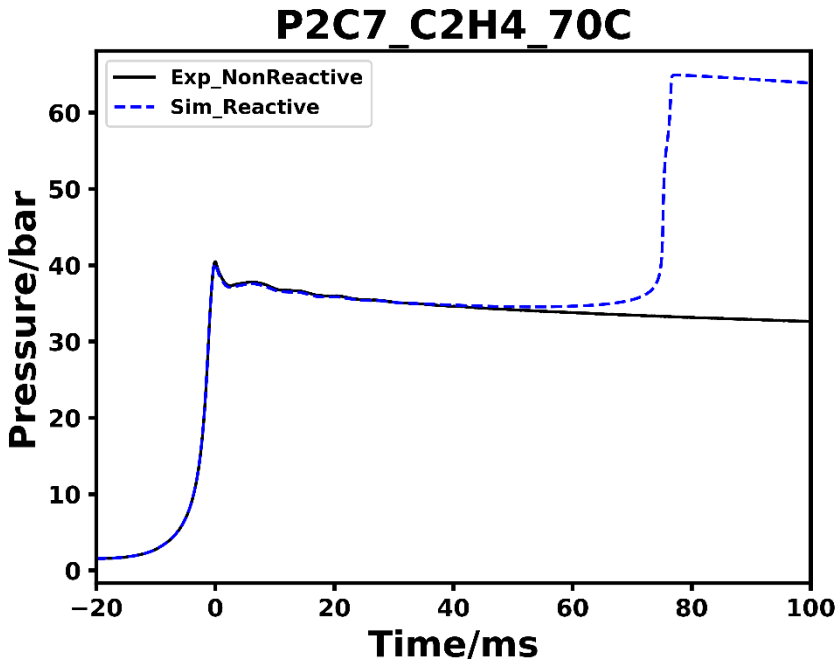

Figure S44. Pressure history of tested reactive and non–reactive mixtures of P2C7 case alongside the simulation's profile for initial temperature of 343 K.

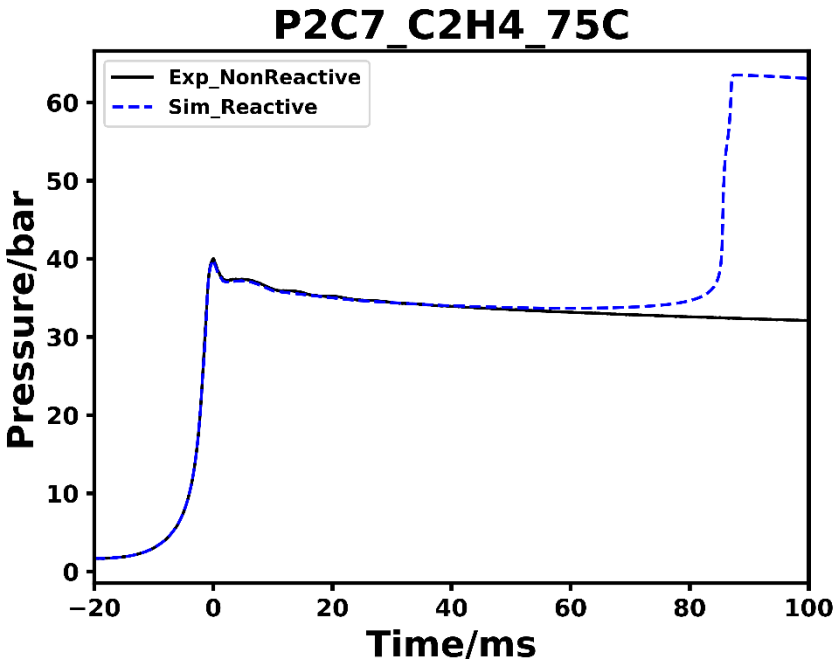

Figure S45. Pressure history of tested reactive and non–reactive mixtures of P2C7 case alongside the simulation's profile for initial temperature of 348 K.

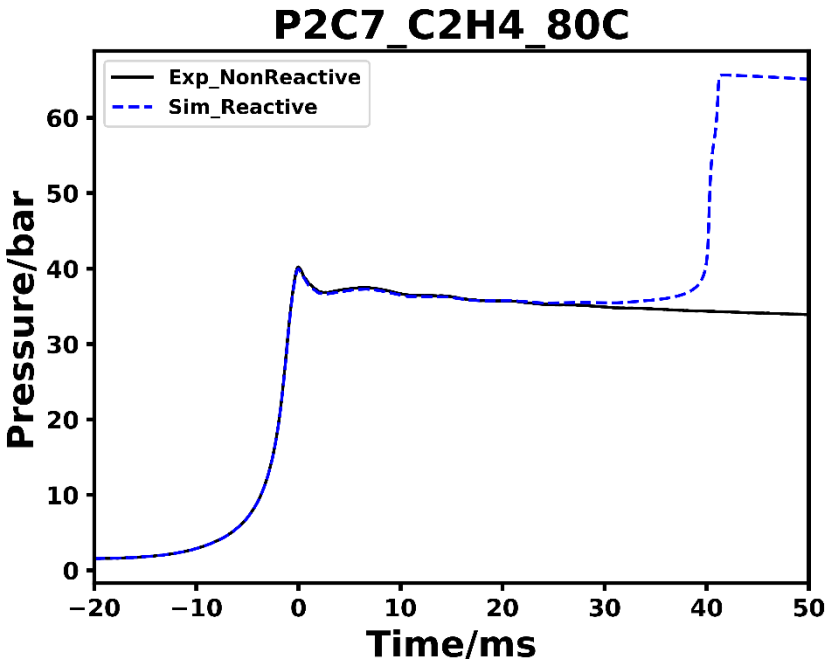

Figure S46. Pressure history of tested reactive and non–reactive mixtures of P2C7 case alongside the simulation's profile for initial temperature of 353 K.

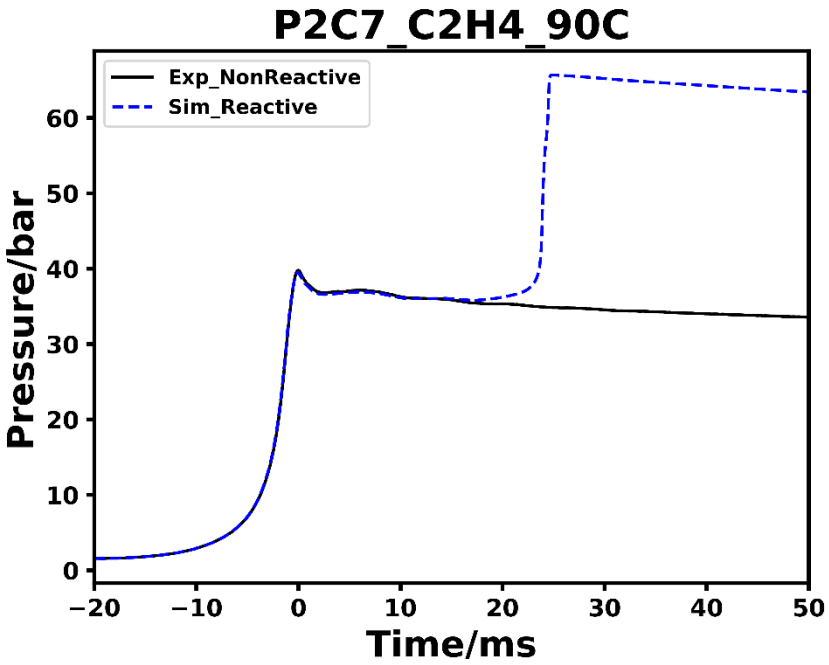

Figure S47. Pressure history of tested reactive and non–reactive mixtures of P2C7 case alongside the simulation's profile for initial temperature of 363 K.

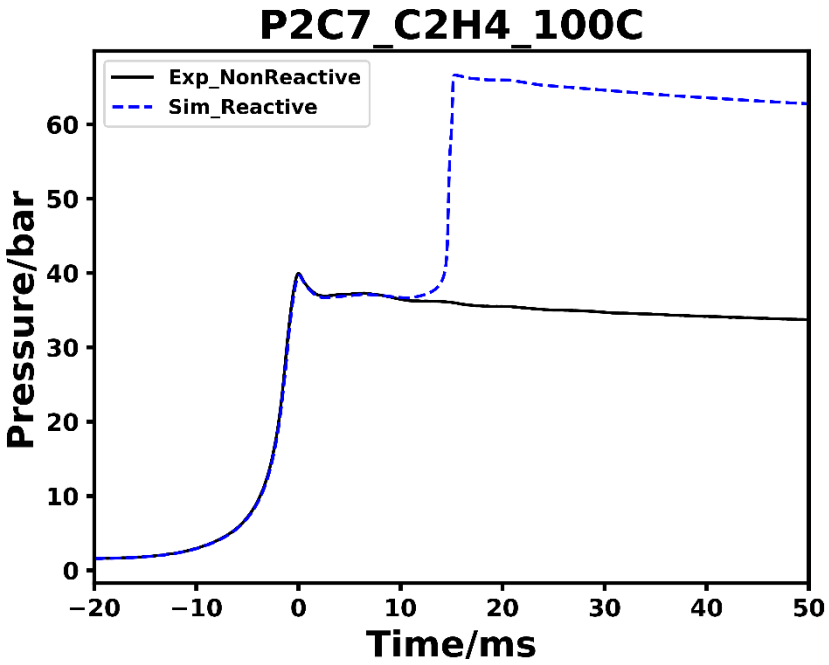

Figure S48. Pressure history of tested reactive and non–reactive mixtures of P2C7 case alongside the simulation's profile for initial temperature of 373 K.

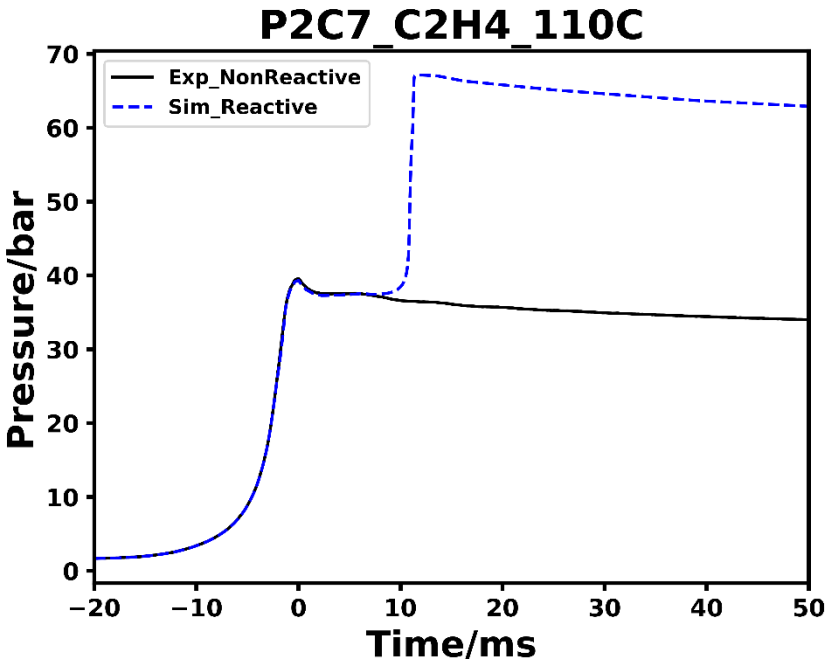

Figure S49. Pressure history of tested reactive and non–reactive mixtures of P2C7 case alongside the simulation's profile for initial temperature of 383 K.

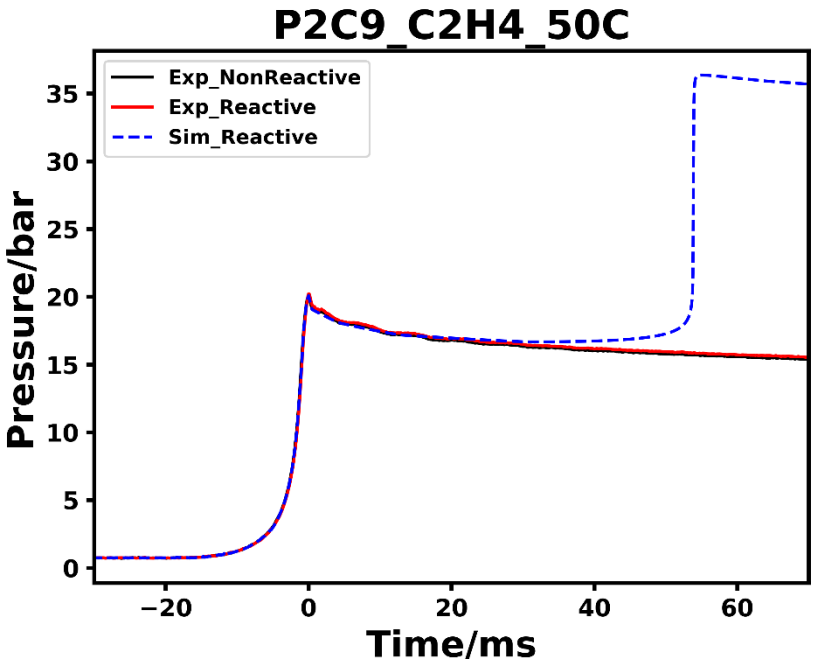

Figure S50. Pressure history of tested reactive and non–reactive mixtures of P2C9 case alongside the simulation's profile for initial temperature of 323 K.

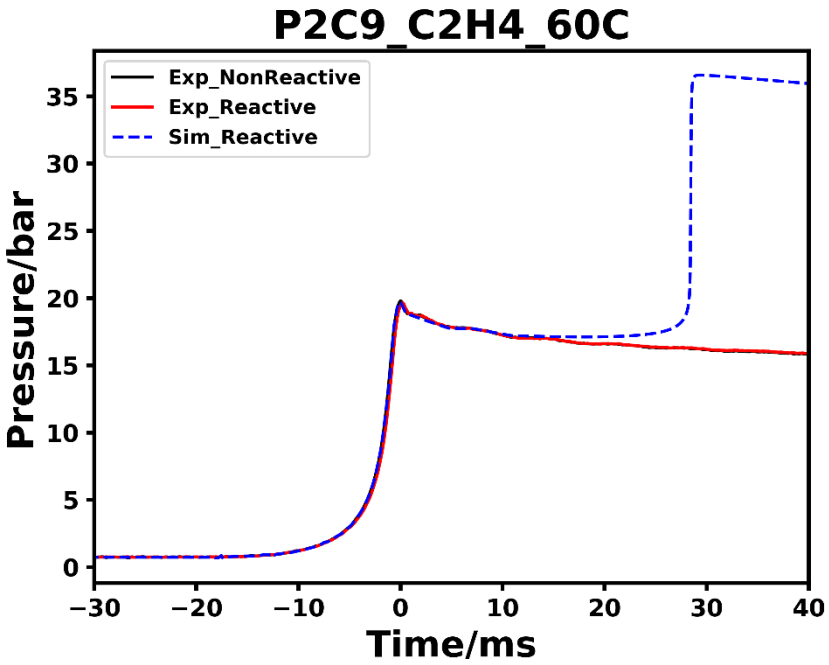

Figure S51. Pressure history of tested reactive and non–reactive mixtures of P2C9 case alongside the simulation's profile for initial temperature of 333 K.

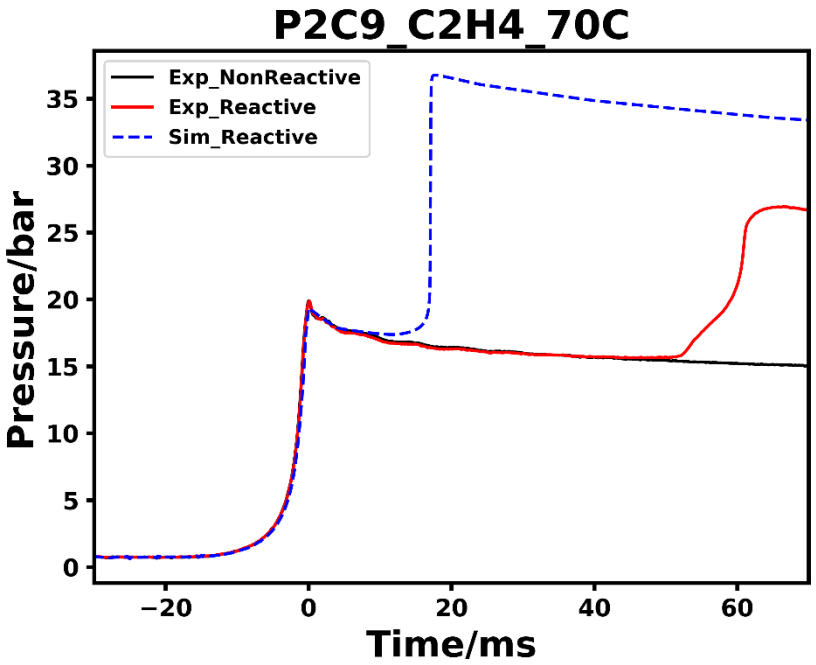

Figure S52. Pressure history of tested reactive and non–reactive mixtures of P2C9 case alongside the simulation's profile for initial temperature of 343 K.

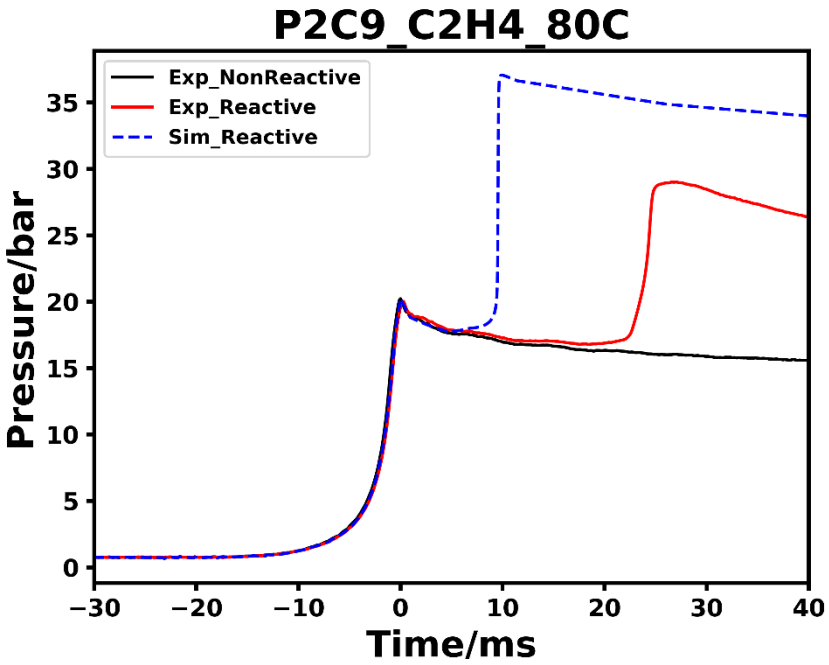

Figure S53. Pressure history of tested reactive and non–reactive mixtures of P2C9 case alongside the simulation's profile for initial temperature of 353 K.

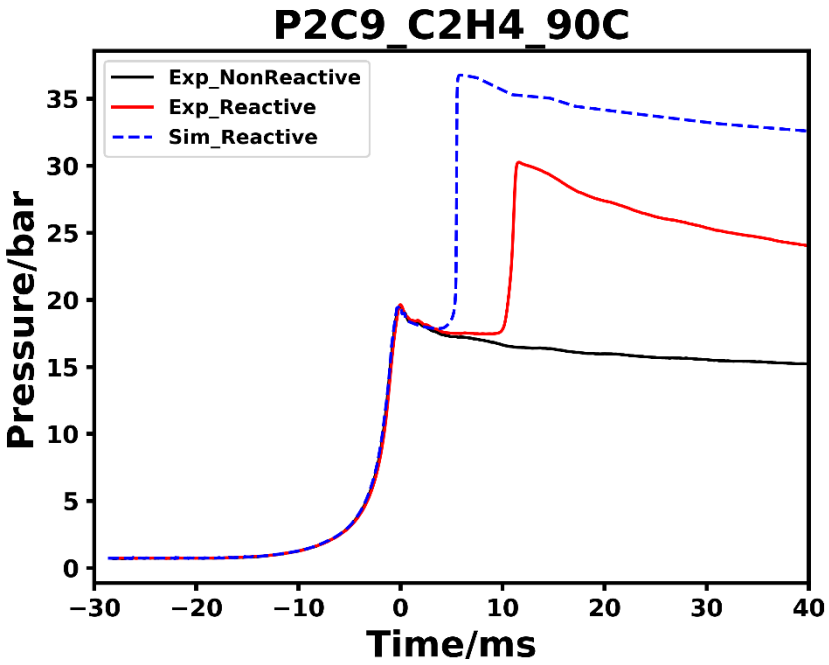

Figure S54. Pressure history of tested reactive and non–reactive mixtures of P2C9 case alongside the simulation's profile for initial temperature of 363 K.

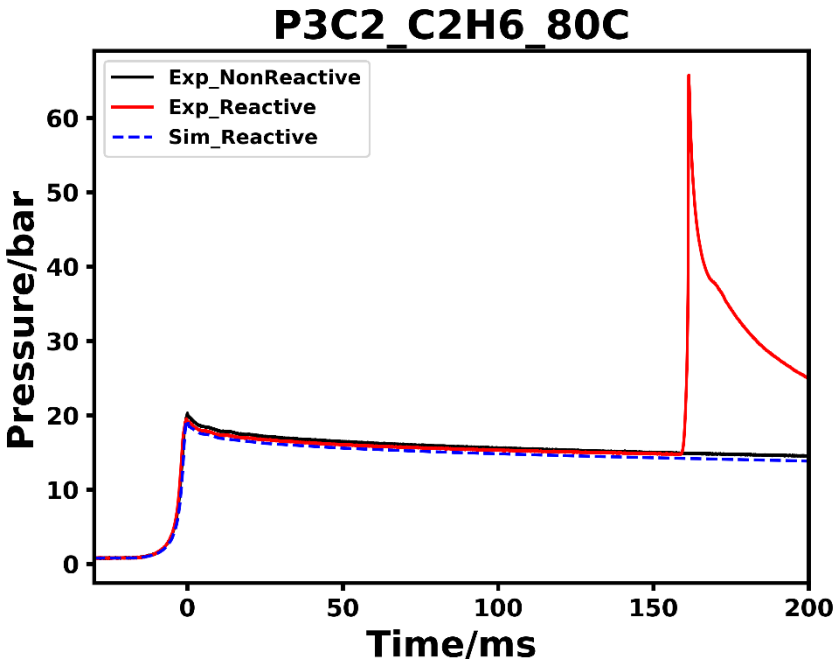

Figure S55. Pressure history of tested reactive and non–reactive mixtures of P3C2 case alongside the simulation's profile for initial temperature of 353 K.

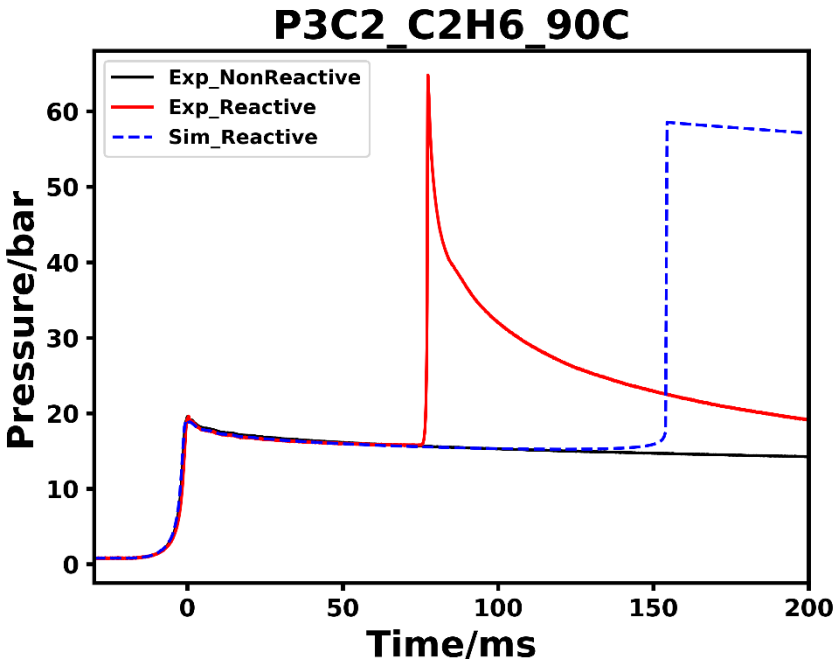

Figure S56. Pressure history of tested reactive and non–reactive mixtures of P3C2 case alongside the simulation's profile for initial temperature of 363 K.

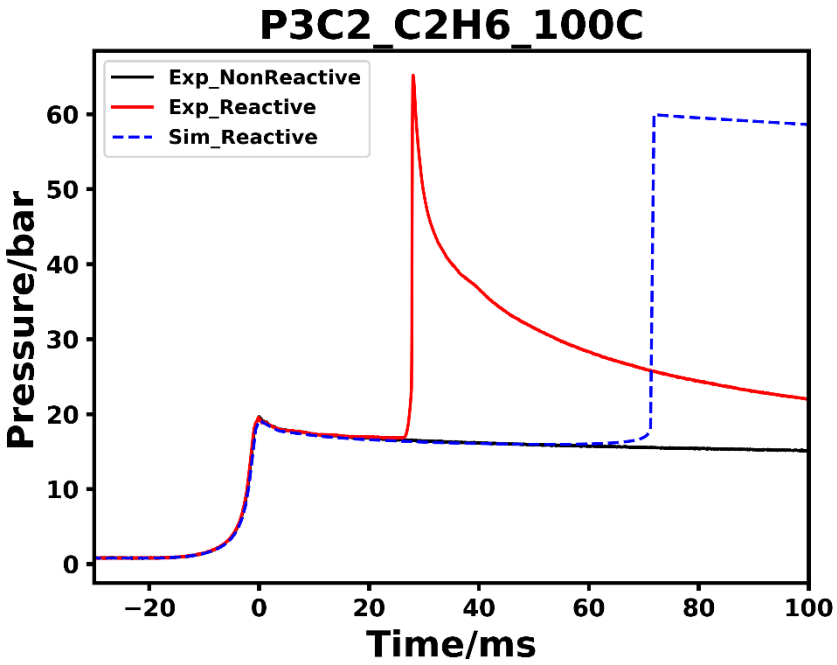

Figure S57. Pressure history of tested reactive and non–reactive mixtures of P3C2 case alongside the simulation's profile for initial temperature of 373 K.

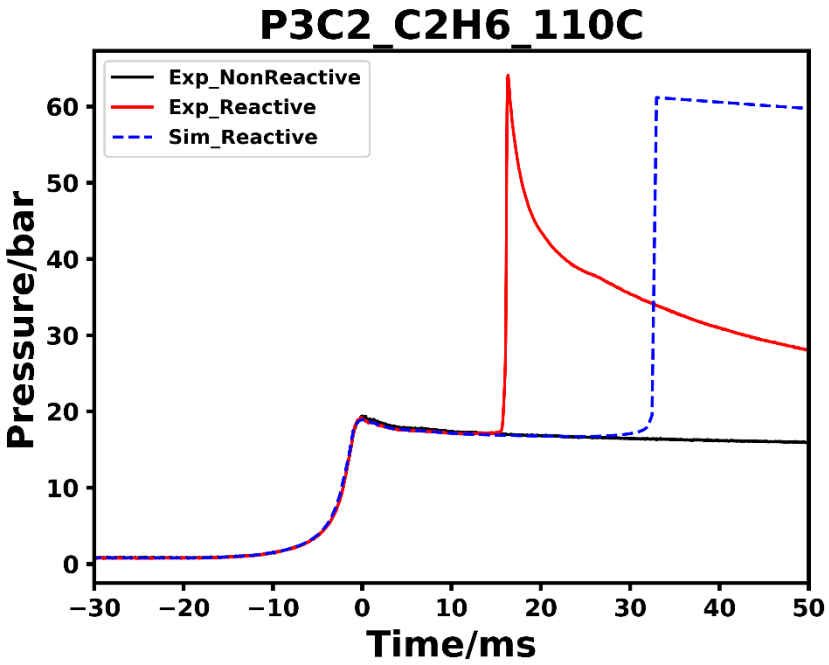

Figure S58. Pressure history of tested reactive and non–reactive mixtures of P3C2 case alongside the simulation's profile for initial temperature of 383 K.

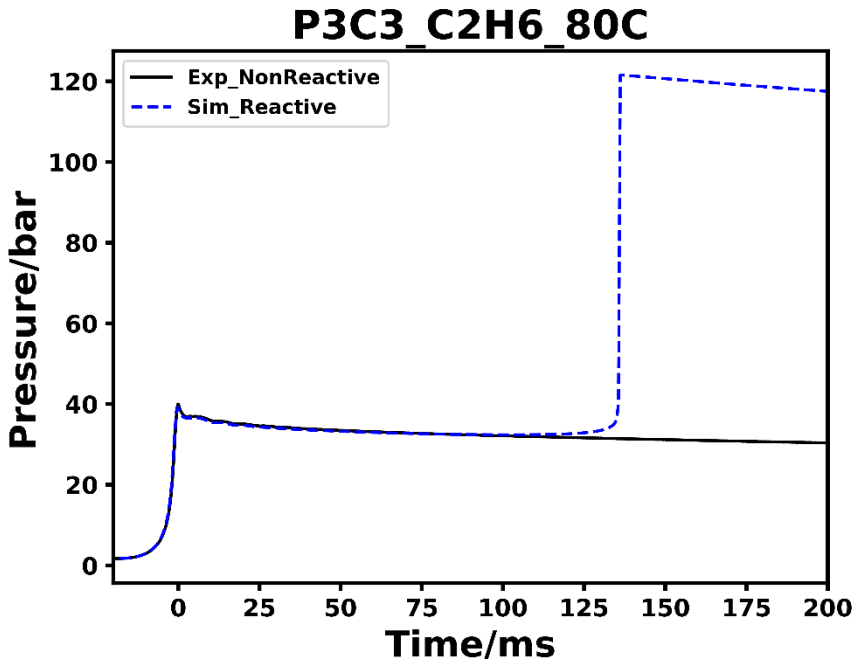

Figure S59. Pressure history of tested reactive and non–reactive mixtures of P3C3 case alongside the simulation's profile for initial temperature of 353 K.

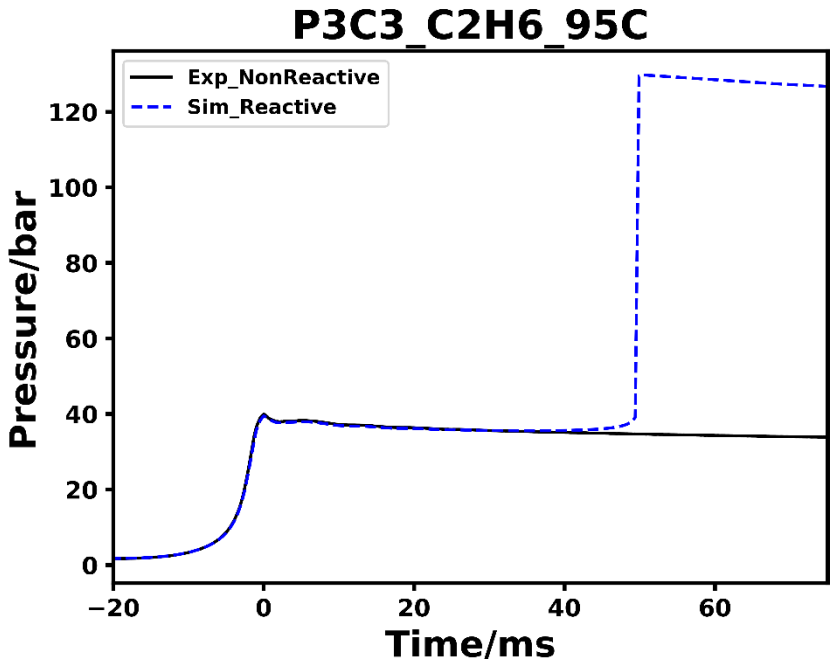

Figure S60. Pressure history of tested reactive and non–reactive mixtures of P3C3 case alongside the simulation's profile for initial temperature of 368 K.

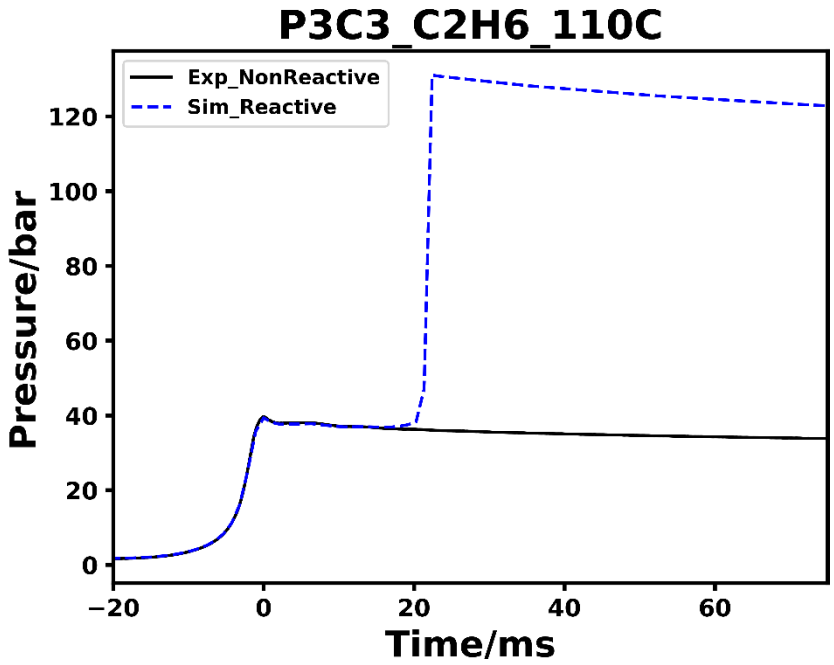

Figure S61. Pressure history of tested reactive and non–reactive mixtures of P3C3 case alongside the simulation's profile for initial temperature of 383 K.

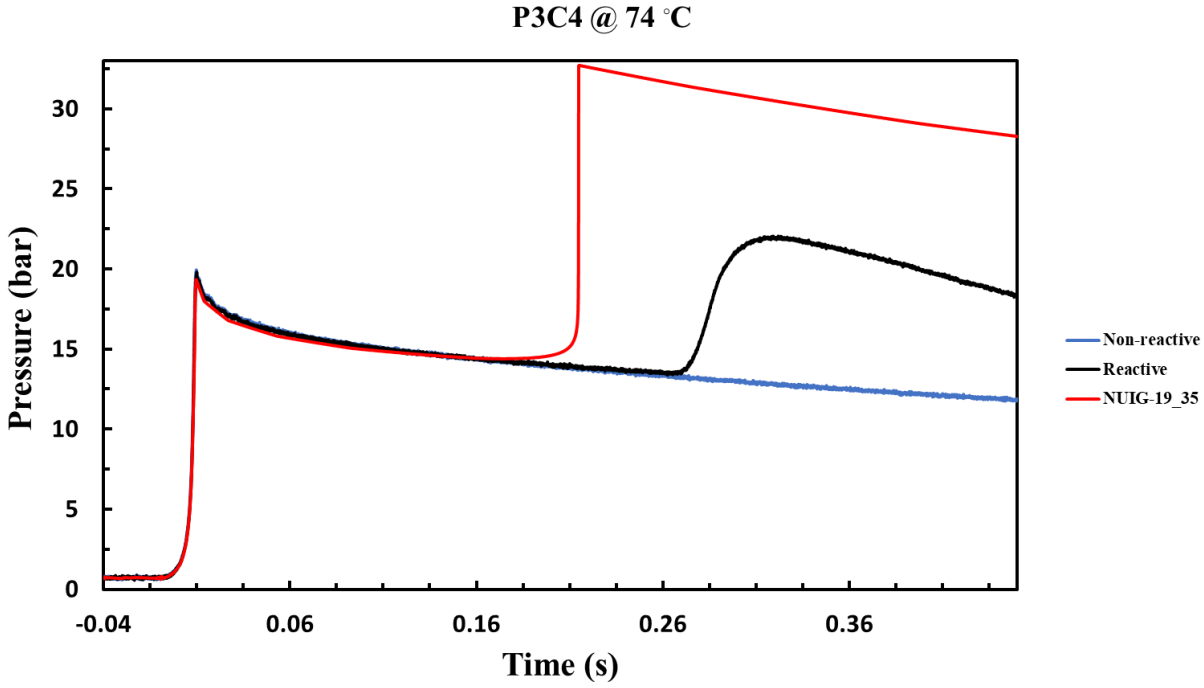

Figure S62. Pressure history of tested reactive and non–reactive mixtures of P3C4 case alongside the simulation's profile for initial temperature of 347 K.

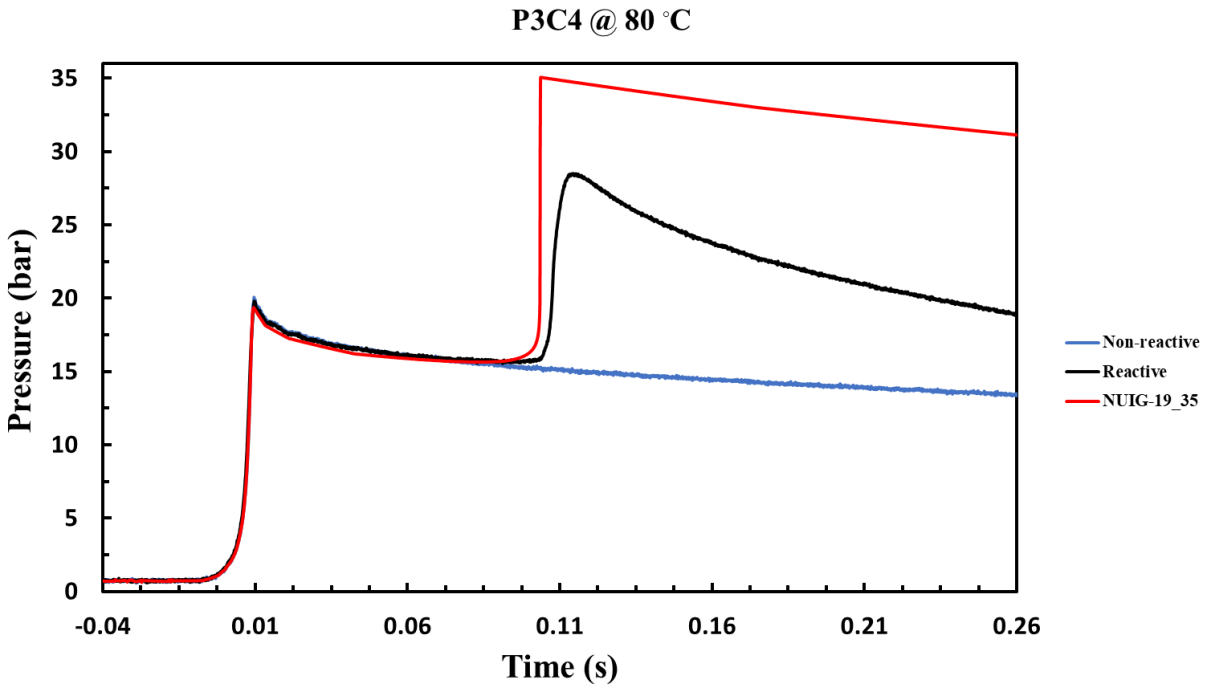

Figure S63. Pressure history of tested reactive and non–reactive mixtures of P3C4 case alongside the simulation's profile for initial temperature of 353 K.

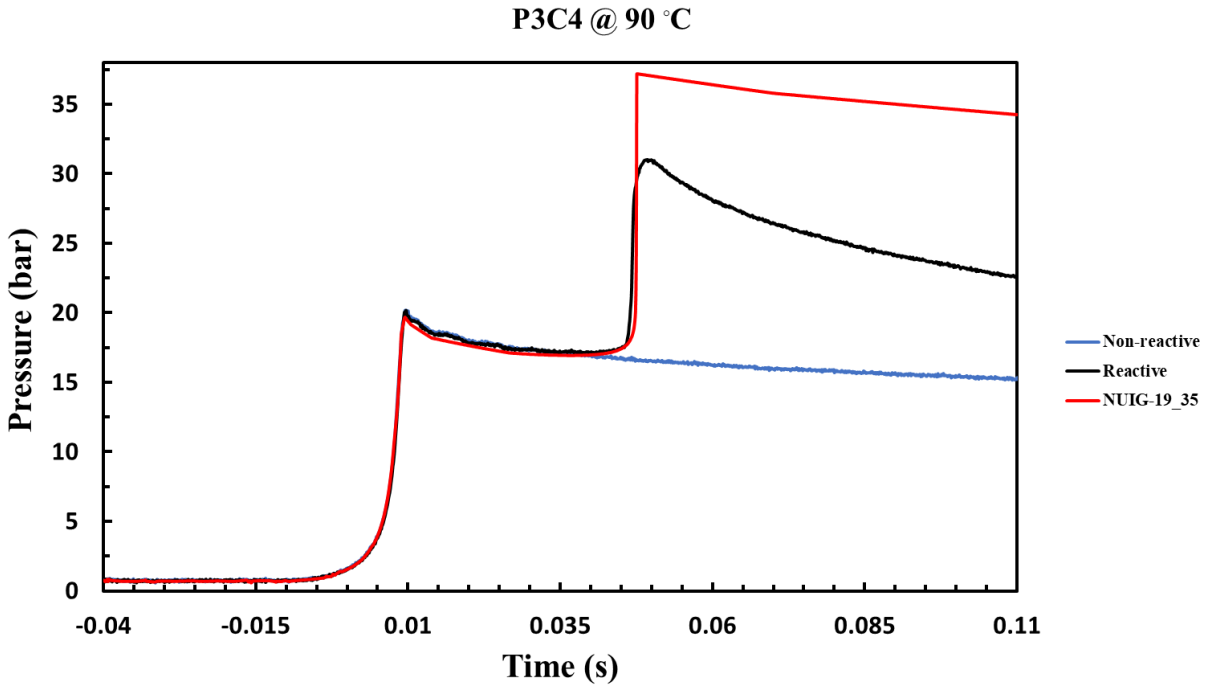

Figure S64. Pressure history of tested reactive and non–reactive mixtures of P3C4 case alongside the simulation's profile for initial temperature of 363 K.

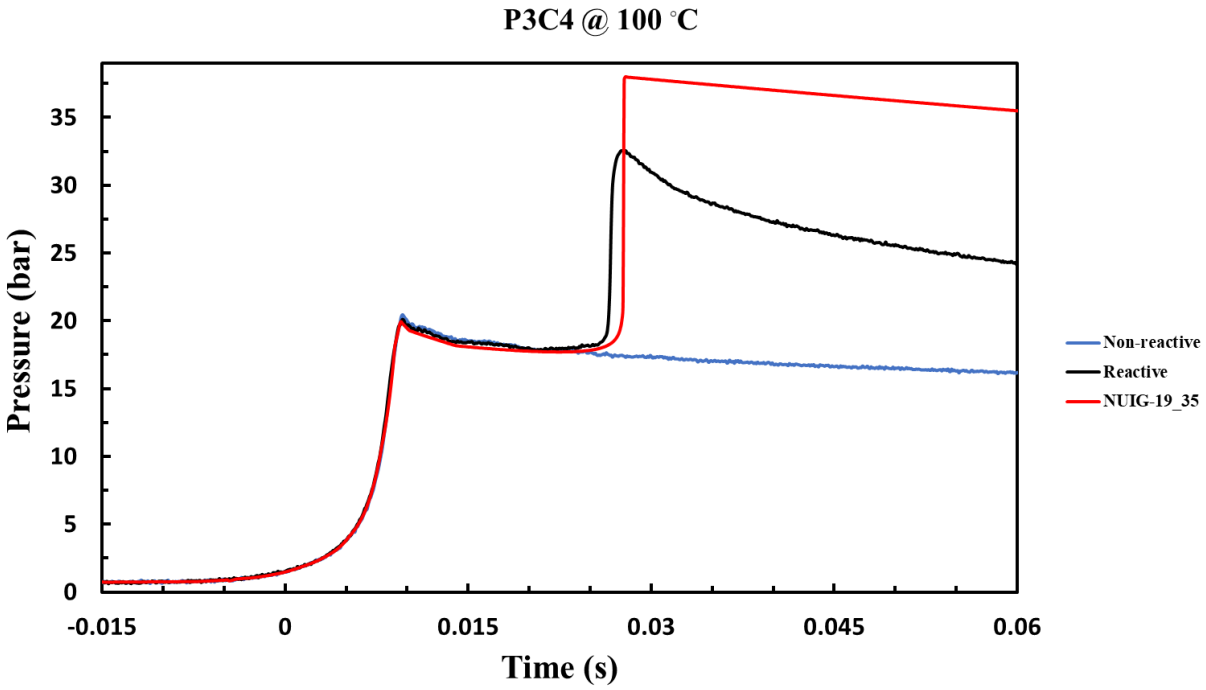

Figure S65. Pressure history of tested reactive and non–reactive mixtures of P3C4 case alongside the simulation's profile for initial temperature of 373 K.

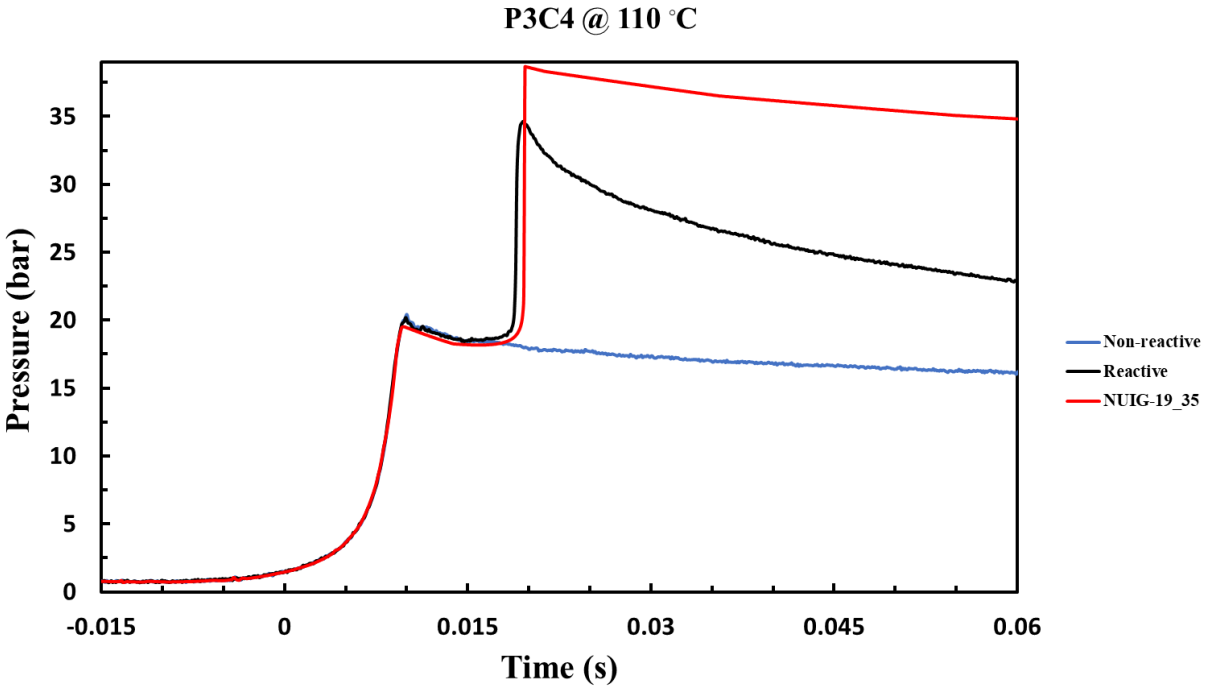

Figure S66. Pressure history of tested reactive and non–reactive mixtures of P3C4 case alongside the simulation's profile for initial temperature of 383 K.

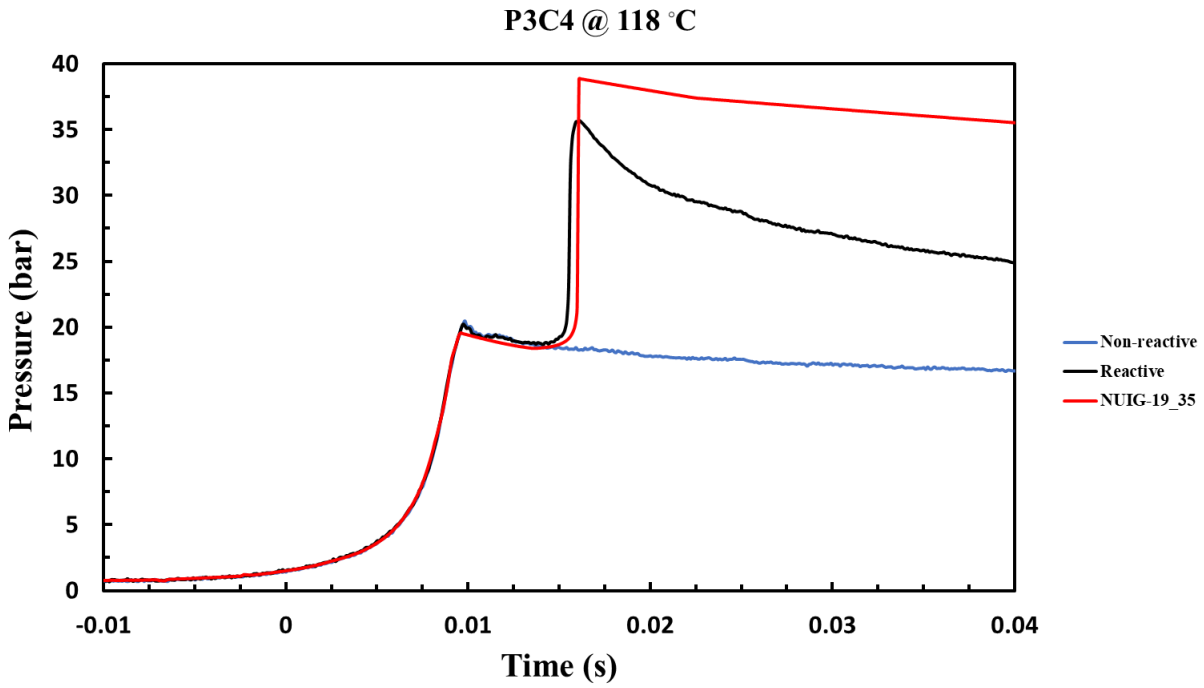

Figure S67. Pressure history of tested reactive and non–reactive mixtures of P3C4 case alongside the simulation's profile for initial temperature of 391 K.

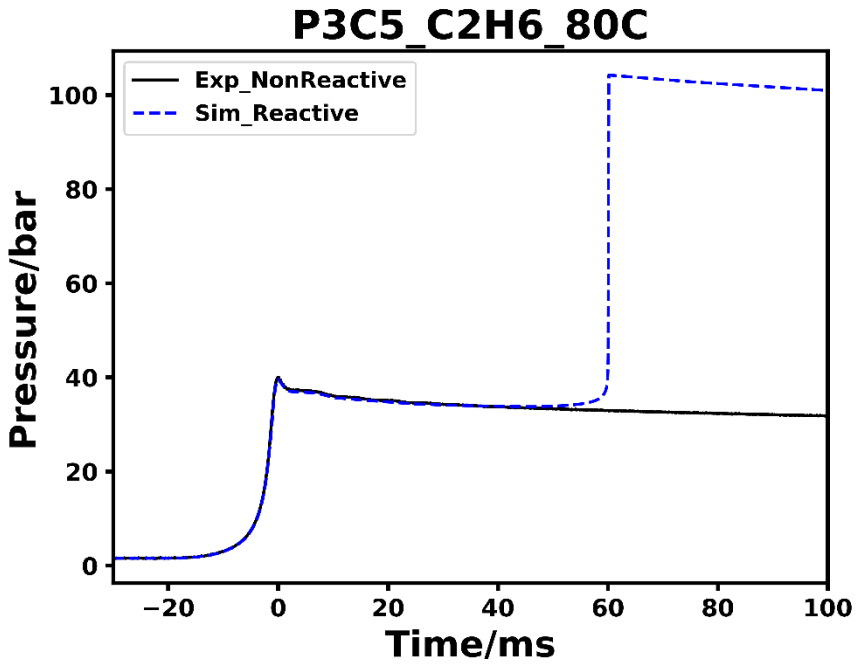

Figure S68. Pressure history of tested reactive and non–reactive mixtures of P3C5 case alongside the simulation's profile for initial temperature of 353 K.

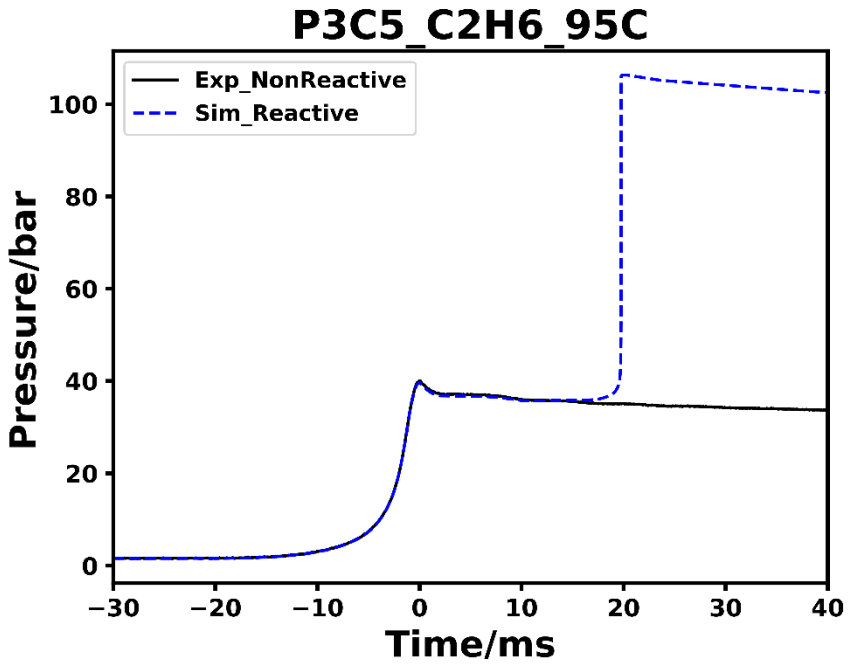

Figure S69. Pressure history of tested reactive and non–reactive mixtures of P3C5 case alongside the simulation's profile for initial temperature of 368 K.

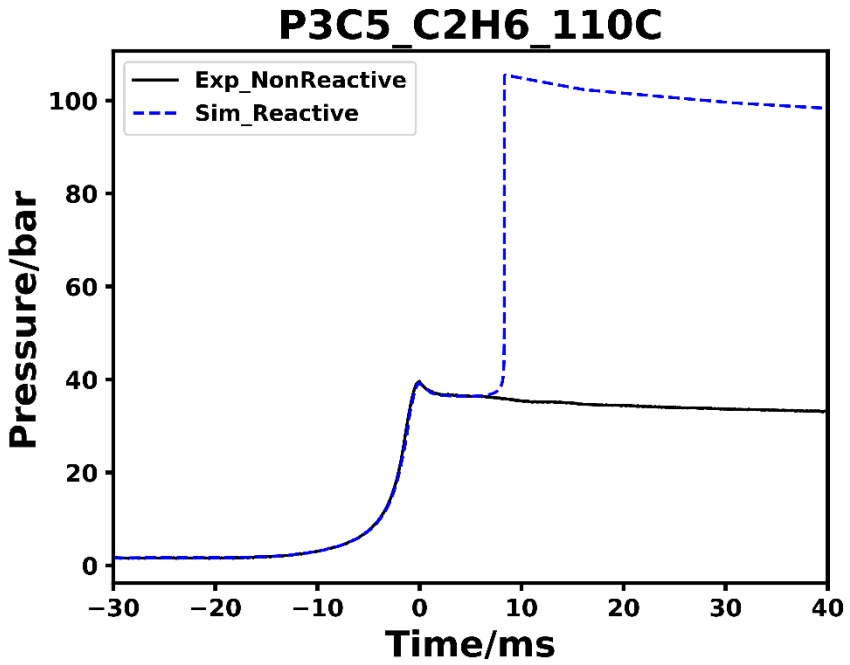

Figure S70. Pressure history of tested reactive and non–reactive mixtures of P3C5 case alongside the simulation's profile for initial temperature of 383 K.

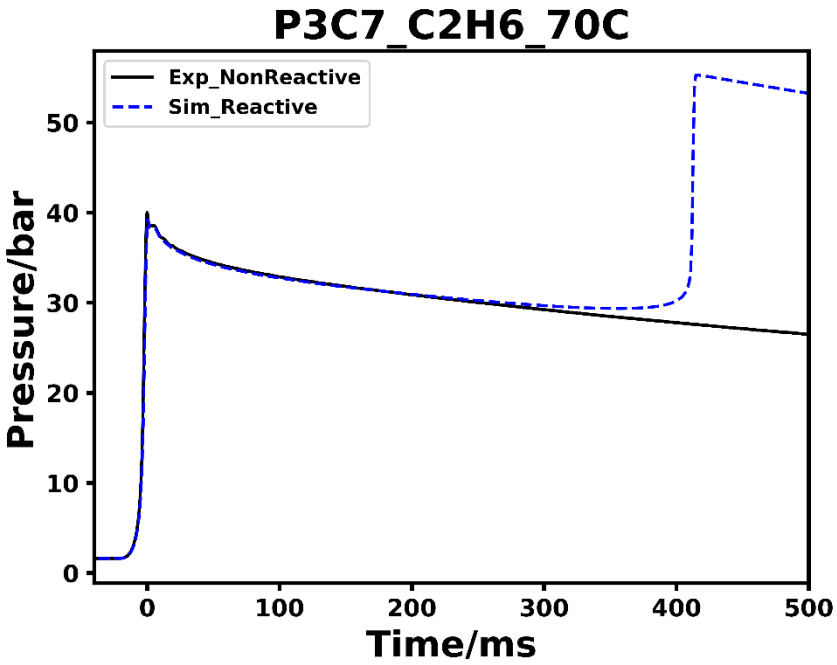

Figure S71. Pressure history of tested reactive and non–reactive mixtures of P3C7 case alongside the simulation's profile for initial temperature of 343 K.

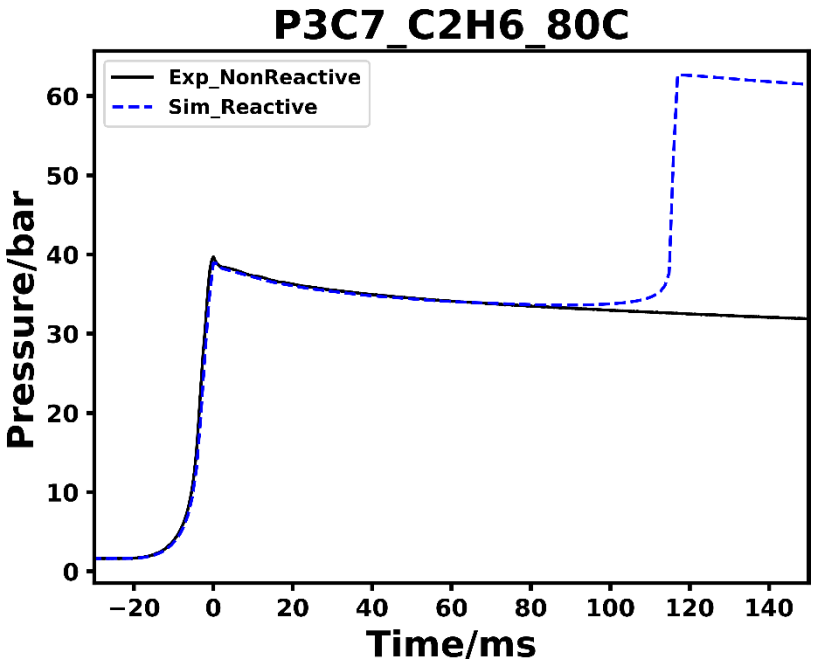

Figure S72. Pressure history of tested reactive and non–reactive mixtures of P3C4 case alongside the simulation's profile for initial temperature of 353 K.

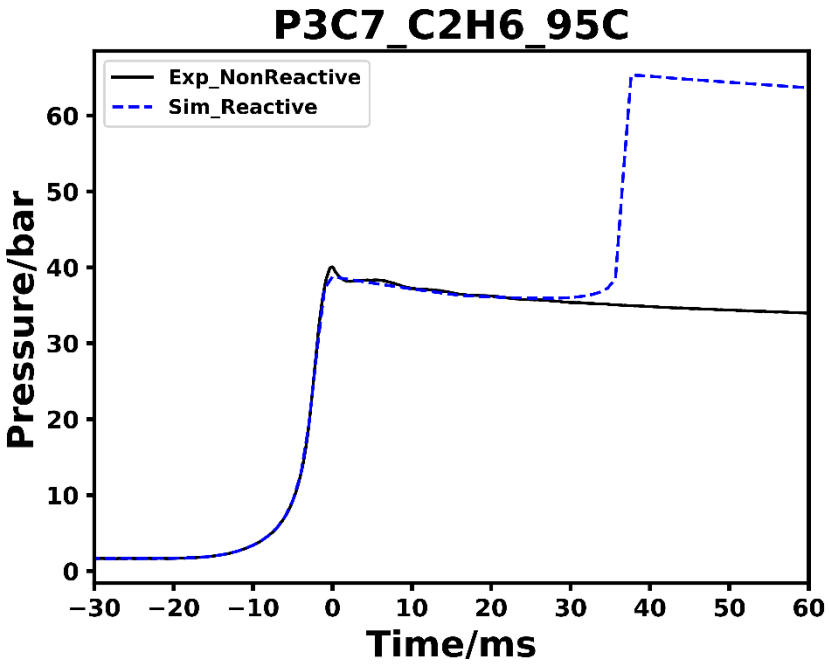

Figure S73. Pressure history of tested reactive and non–reactive mixtures of P3C7 case alongside the simulation's profile for initial temperature of 368 K.

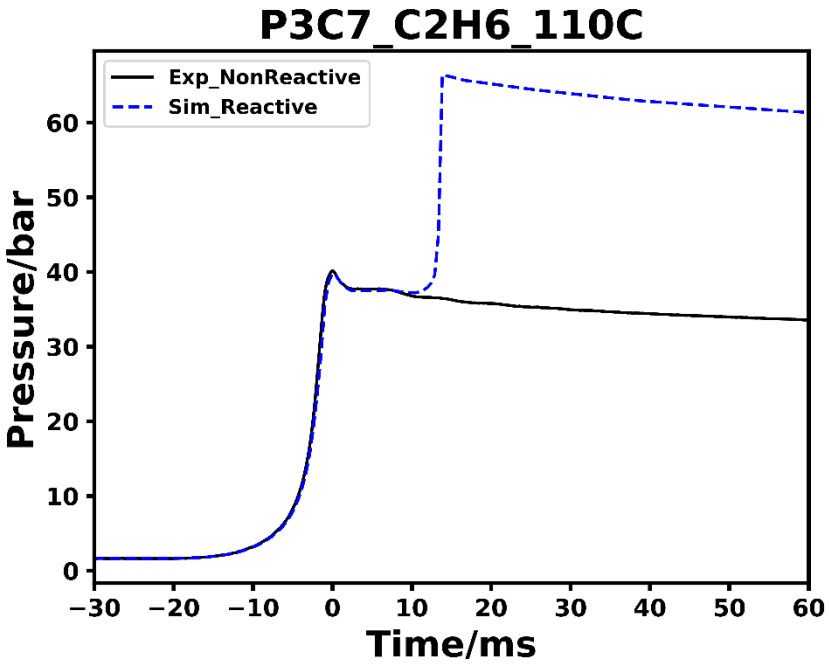

Figure S74. Pressure history of tested reactive and non–reactive mixtures of P3C7 case alongside the simulation's profile for initial temperature of 383 K.

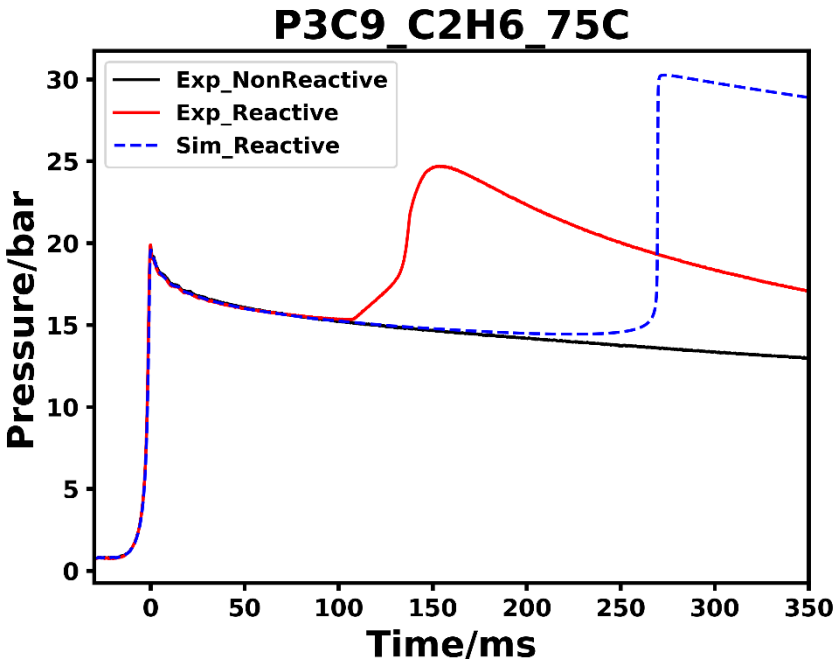

Figure S75. Pressure history of tested reactive and non–reactive mixtures of P3C9 case alongside the simulation's profile for initial temperature of 348 K.

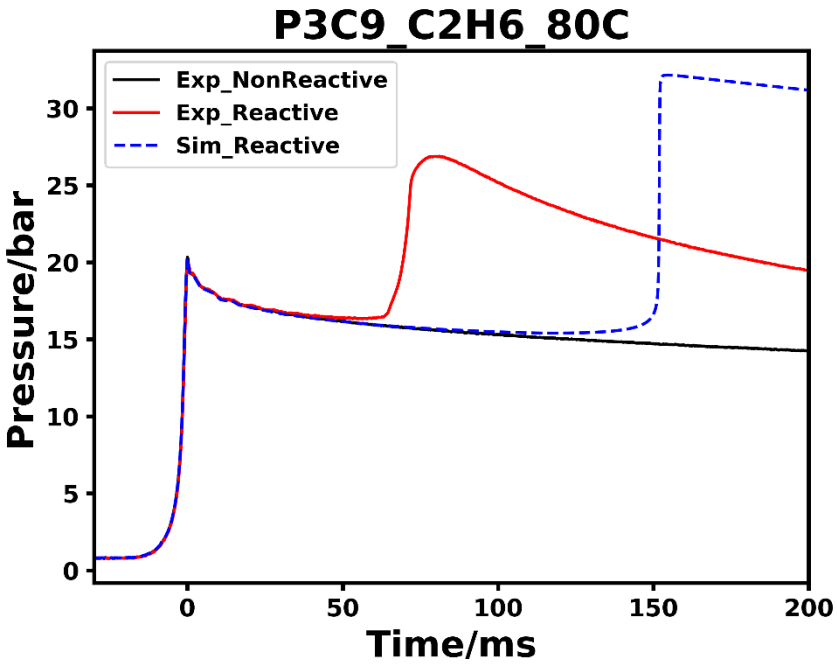

Figure S76. Pressure history of tested reactive and non–reactive mixtures of P3C9 case alongside the simulation's profile for initial temperature of 353 K.

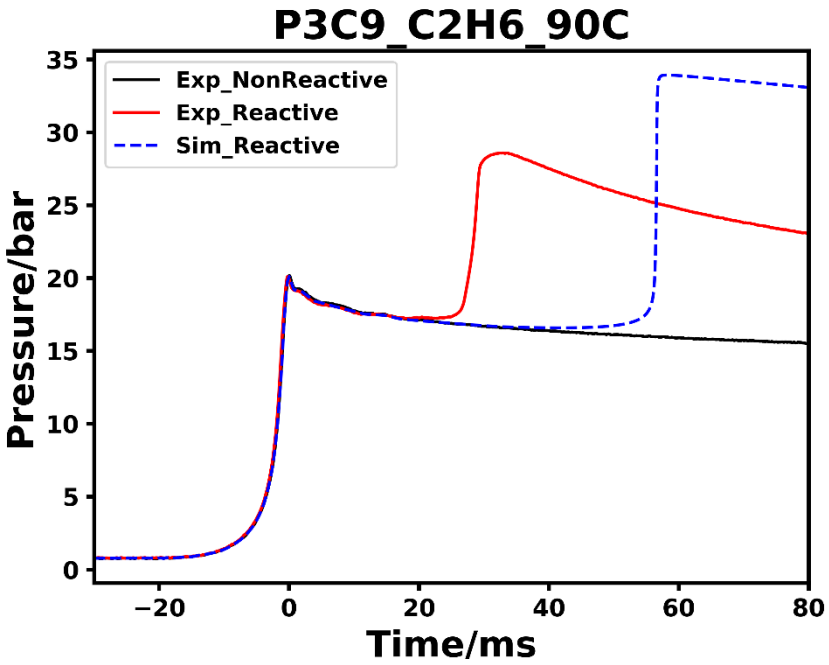

Figure S77. Pressure history of tested reactive and non–reactive mixtures of P3C9 case alongside the simulation's profile for initial temperature of 363 K.

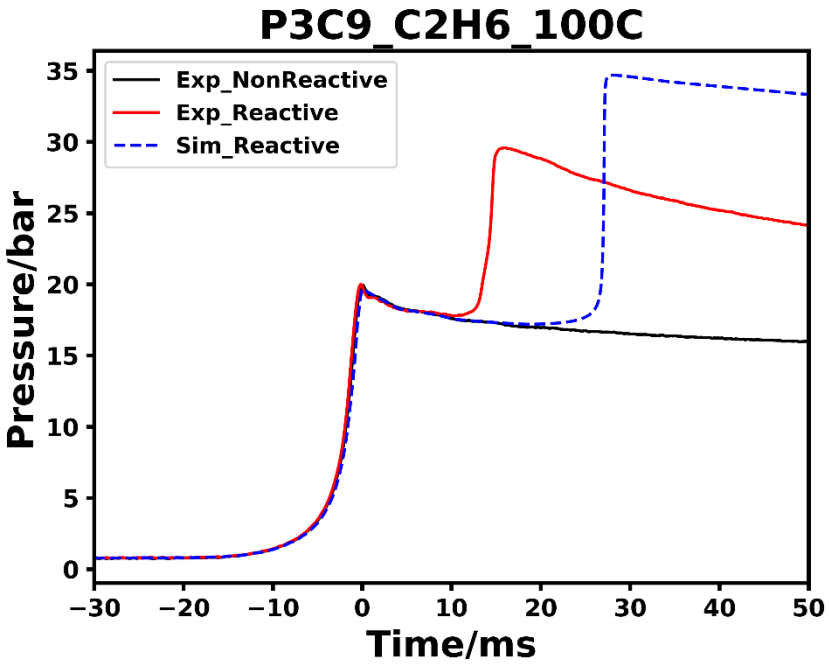

Figure S78. Pressure history of tested reactive and non–reactive mixtures of P3C9 case alongside the simulation's profile for initial temperature of 373 K.

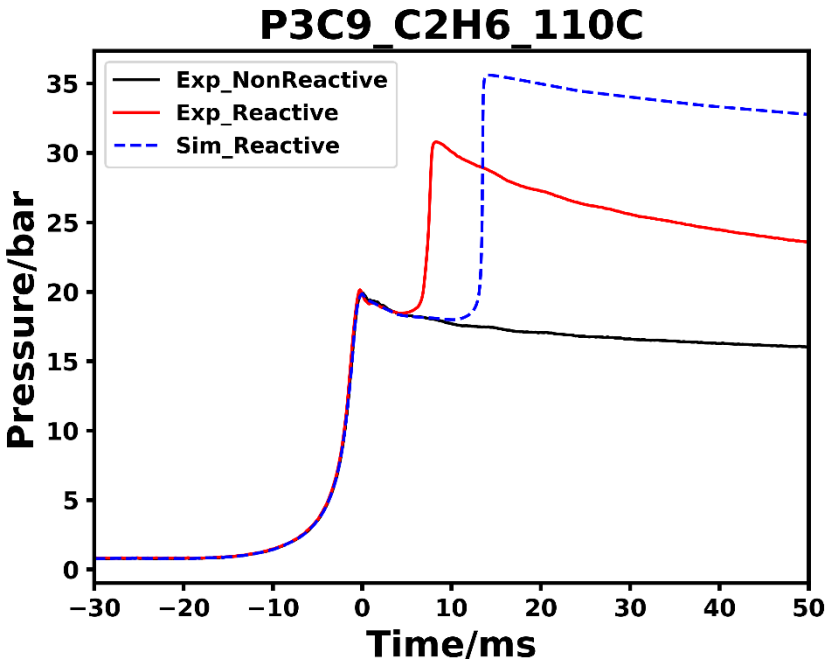

Figure S79. Pressure history of tested reactive and non–reactive mixtures of P3C9 case alongside the simulation's profile for initial temperature of 383 K.

10 Performance of NUIGMech0.9 under high pressure–low temperature regime

The performance of NUIGMech0.9 under high–pressure and low–temperature regime is shown in Figure S80. As seen, this chemical mechanism reproduces the experimental IDTs of various methane mixtures under the studied conditions very well.

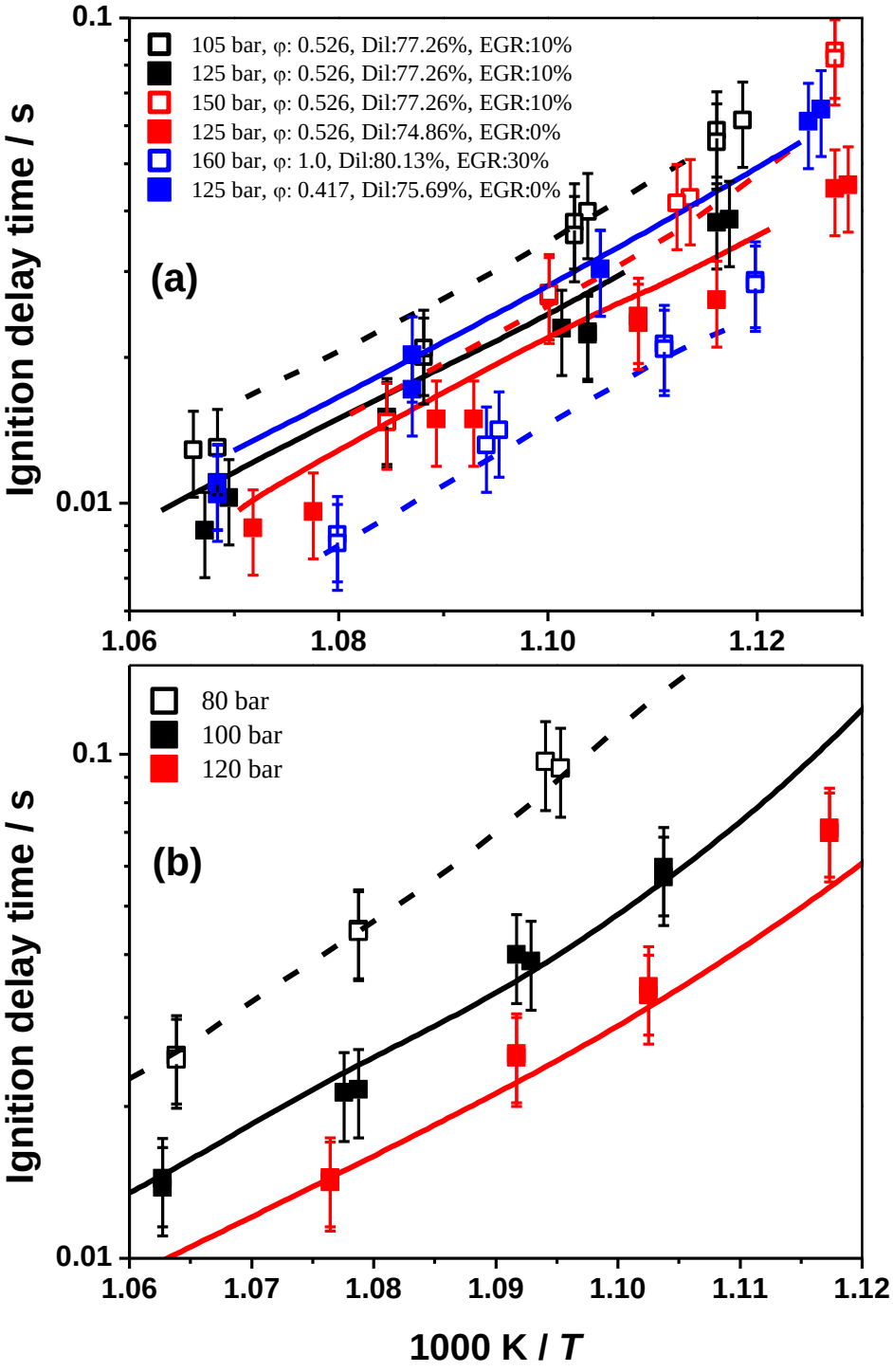

Figure S80. Performance of NUIGMech0.9 under high–pressure and low–temperature regime for methane mixtures: Experimental and simulation data are shown by the same colour symbols and lines, respectively. Dashed lines correspond to the simulation data of the opened symbols; (a) Experimental data from [17], (b) Experimental data from [26]; methane + air mixture with φ = 0.526.

11 Complementary analyses

11.1 Ignition delay time

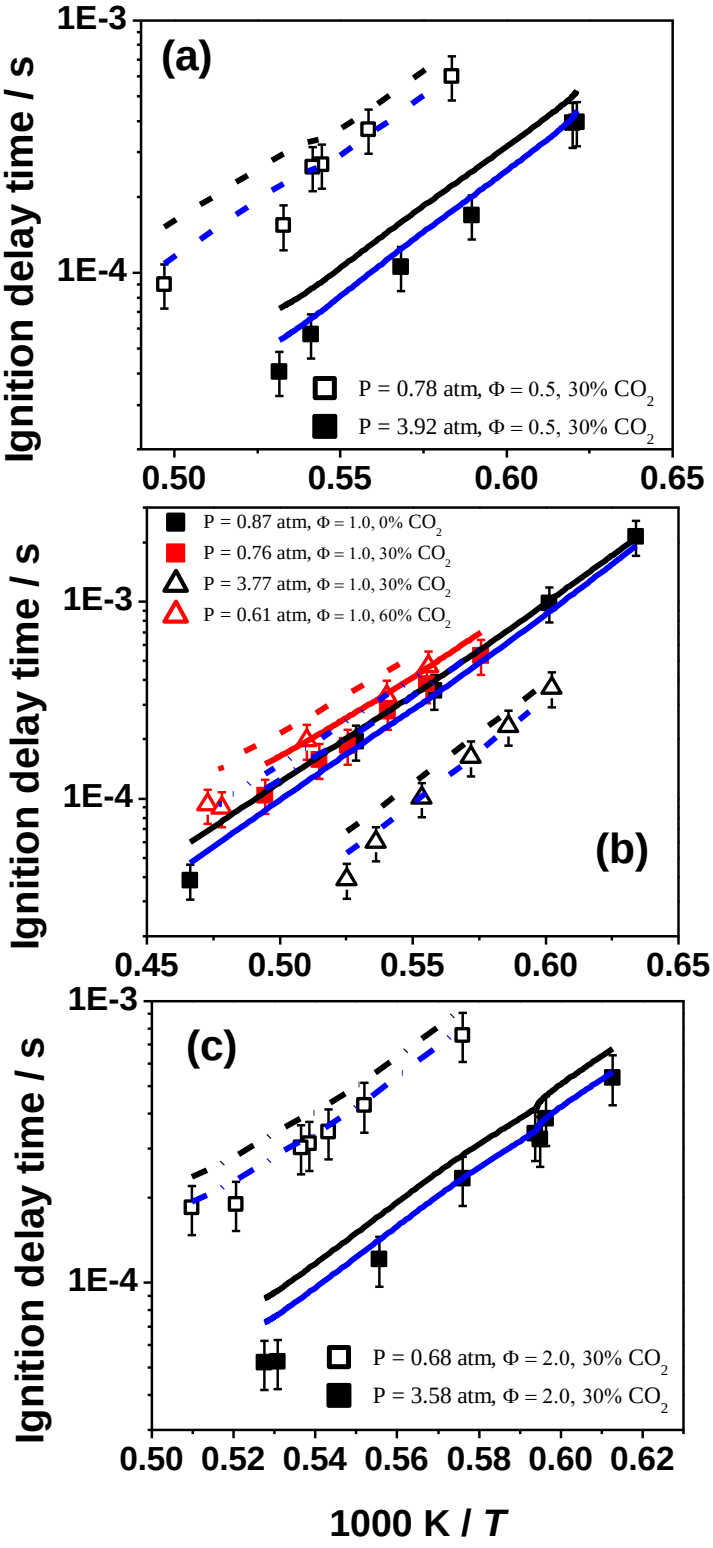

Figure S81. Performance of NUIGMech0.9 under low–pressure and high–temperature regime for methane mixtures: Experimental and simulation data are shown by the same colour symbols and lines, respectively. Dashed lines correspond to the simulation data of the opened symbols; Blue–lines correspond to the simulation data of CRECK chemical mechanism[9]; Experimental data from [27].

11.2 Laminar burning velocity

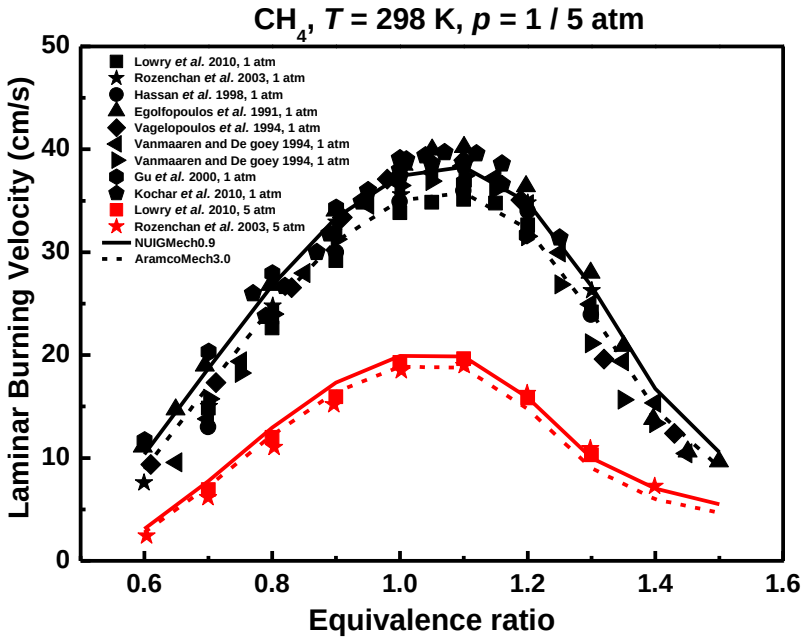

Figure S82. Performance of NUIGMech0.9 for predicting laminar burning velocity of methane + air mixtures under low– (the black symbols and lines) to elevated– (the red symbols and lines) pressures.[28-35]

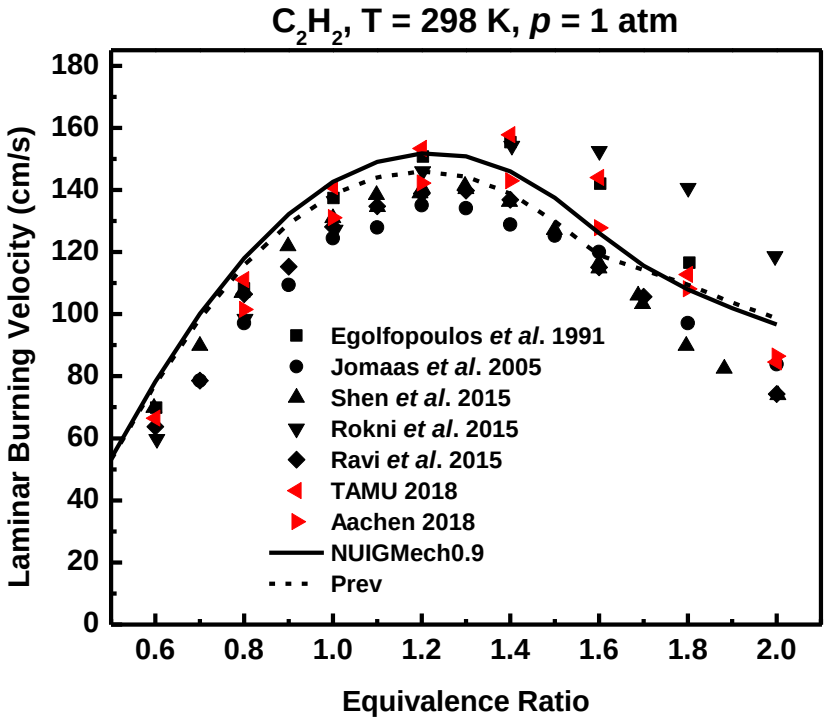

Figure S83. Performance of NUIGMech0.9 for predicting laminar burning velocity of acetylene + air mixtures.[28, 36-40]

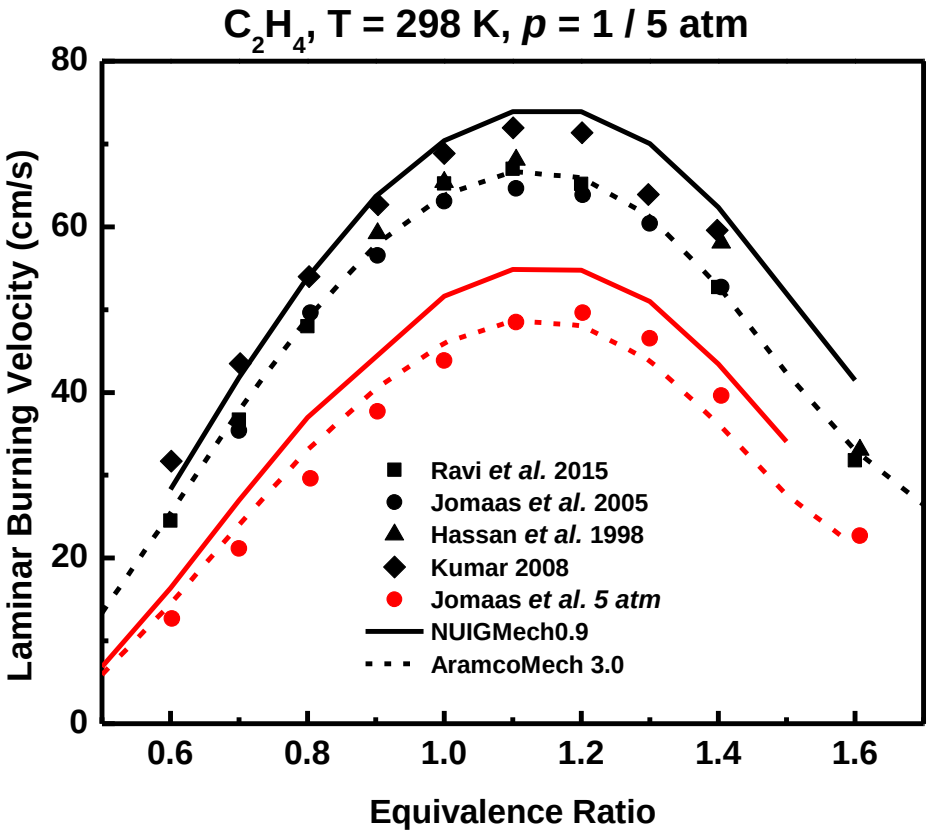

Figure S84. Performance of NUIGMech0.9 for predicting laminar burning velocity of ethylene + air mixtures under low– (the black symbols and lines) to elevated– (the red symbols and lines) pressures.[36, 39, 41, 42]

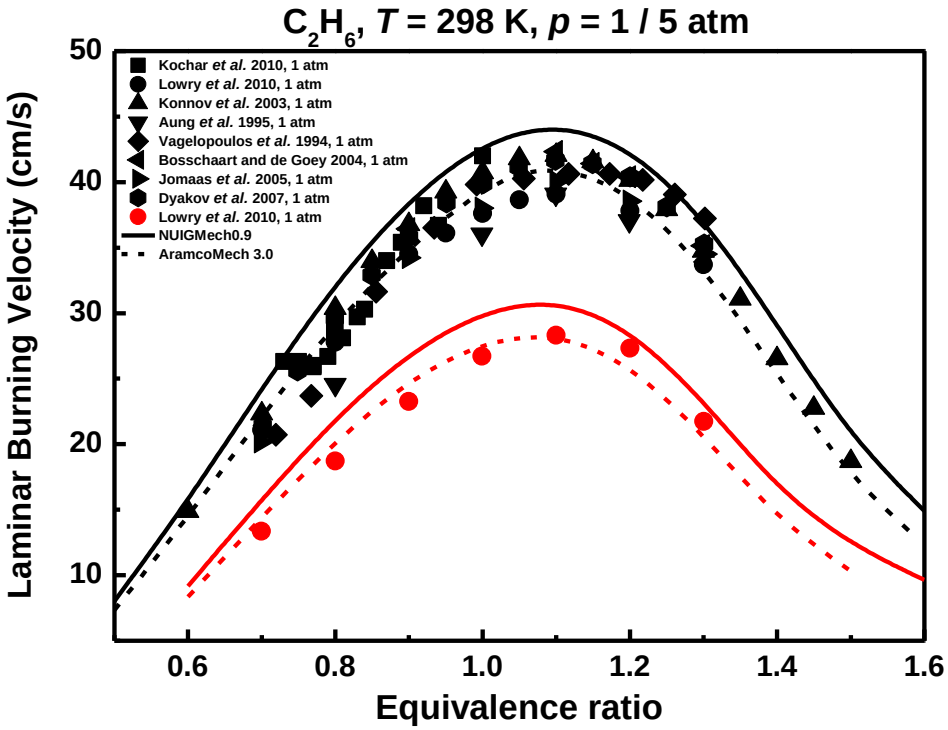

Figure S85. Performance of NUIGMech0.9 for predicting laminar burning velocity of ethane + air mixtures under low– (the black symbols and lines) to elevated– (the red symbols and lines) pressures.[29, 32, 35, 36, 43-46]

11.3 Speciation (JSR): Ethylene

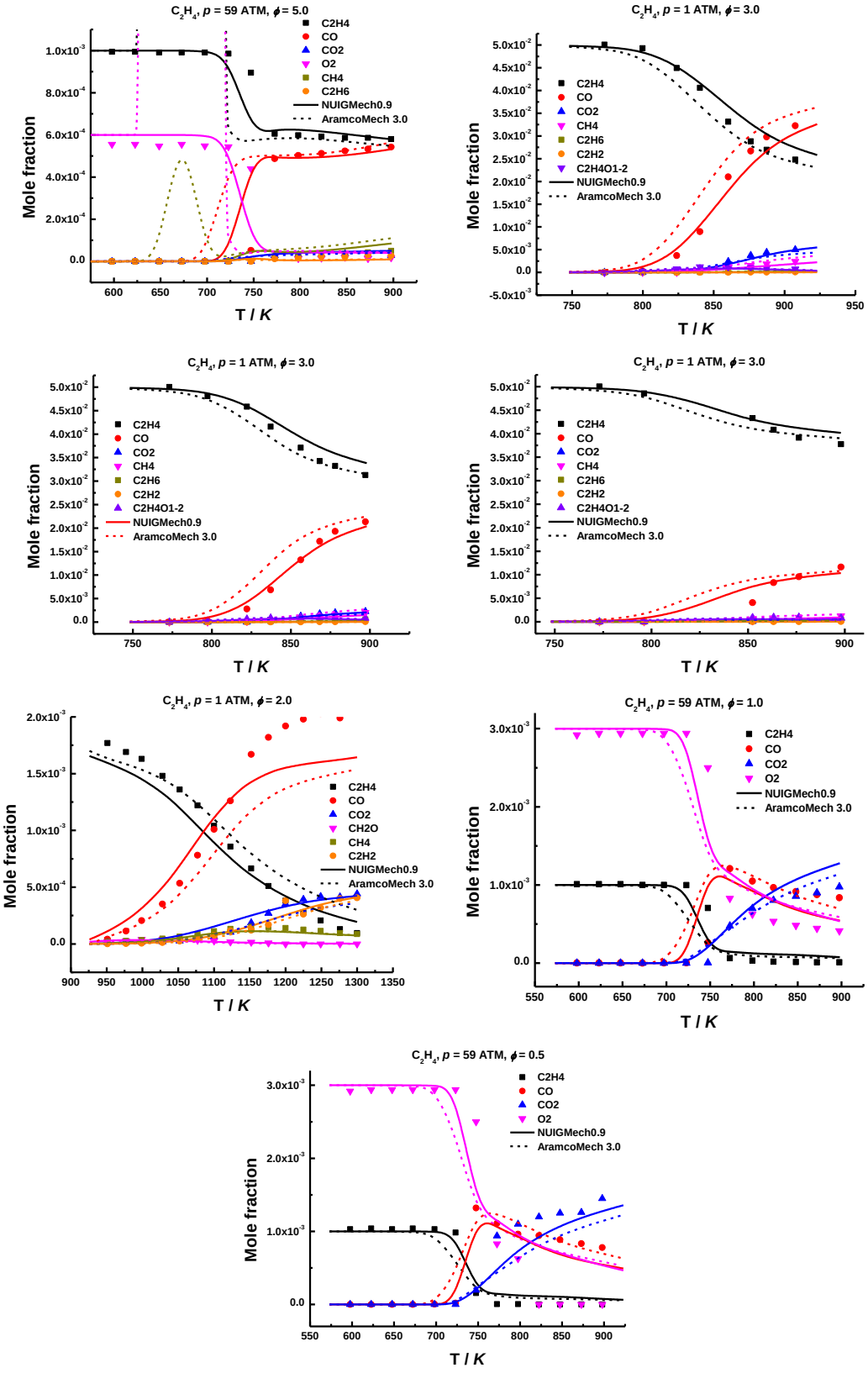

Figure S86. Performance of NUIGMech0.9 for predicting mole fraction distribution of various species over temperature for ethylene + air mixtures at different pressures and equivalence ratios.[47-49]

11.4 Individual and combined effects of the studied parameters on IDTs

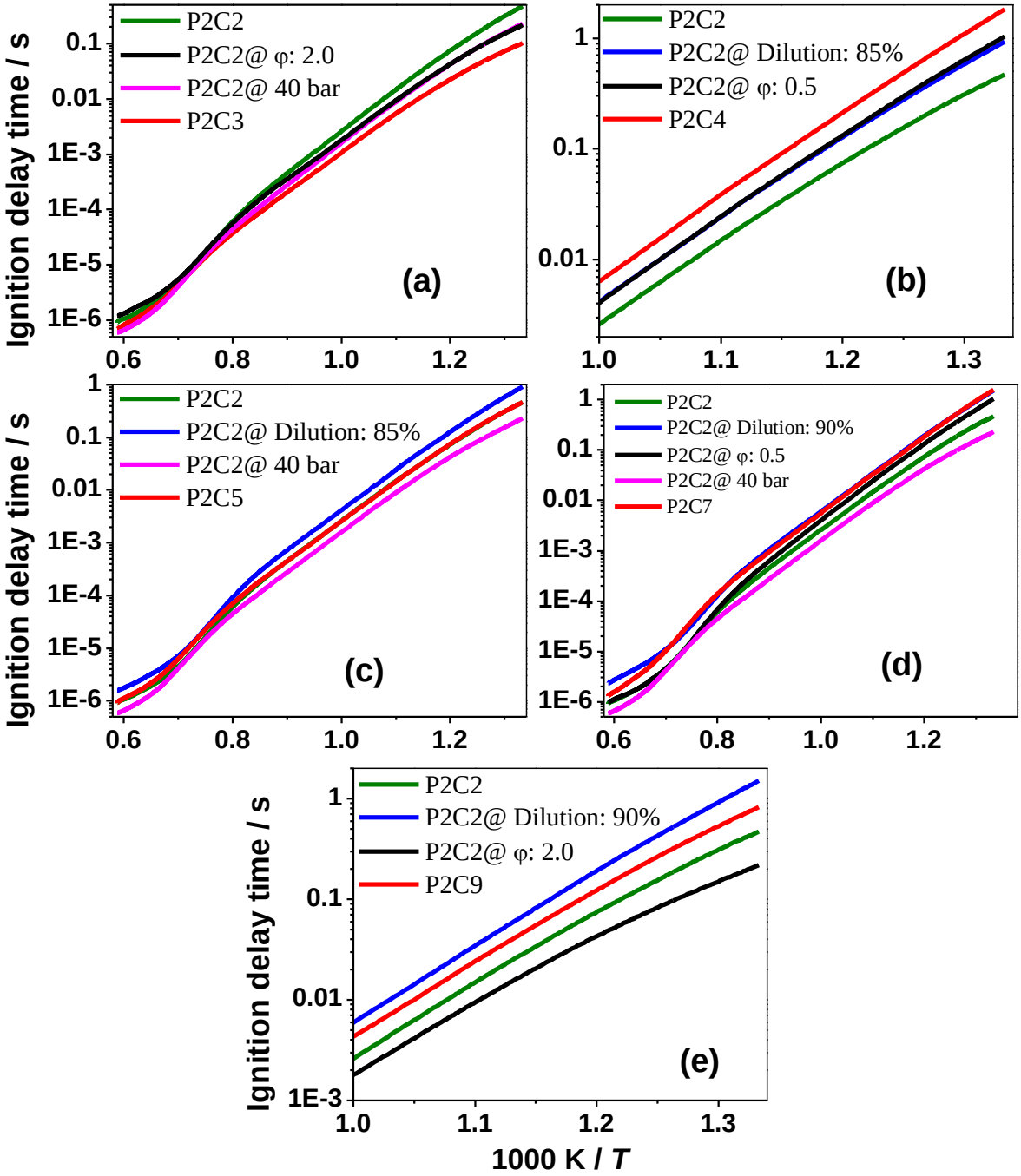

Figure S87. Individual and combined effects of pressure, equivalence ratio and dilution on ethylene's IDTs. (For better interpretation of the colours, the reader is referred to the web version of this article)

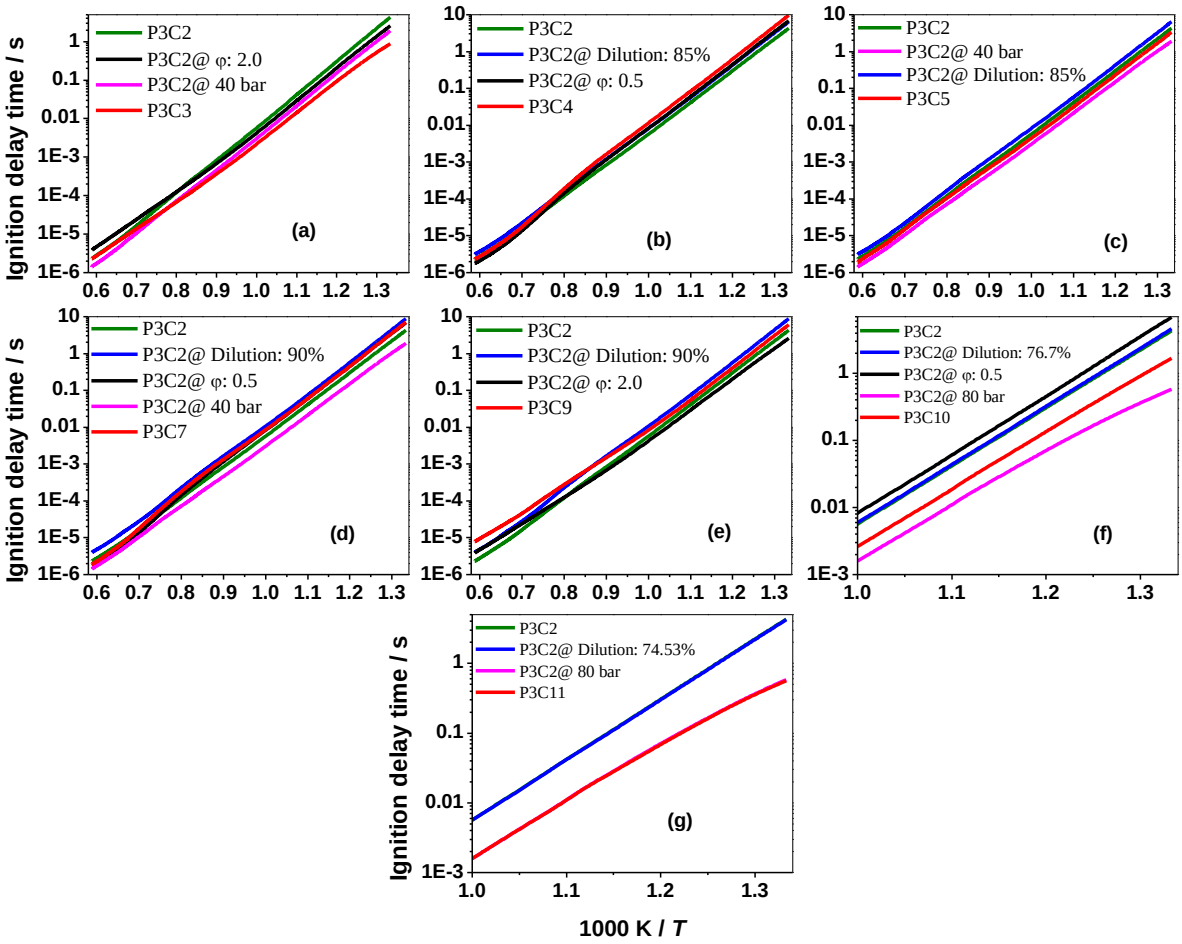

Figure S88. Individual and combined effects of pressure, equivalence ratio and dilution on ethane's IDTs. (For better interpretation of the colours, the reader is referred to the web version of this article)

11.5 Chemical kinetics development analyses

To gain a better understanding of the effect of the studied parameters on IDT, brute–force sensitivity analyses of IDT followed by flux analyses are performed for the important reactions in the individual zones (lines 1–3) identified in Figures 6 and 8. The sensitivity coefficient (S) of the brute–force sensitivity analysis is calculated as:

$$S = \frac{ln\left(\frac{\tau^+}{\tau^-}\right)}{ln\left(\frac{2}{0.5}\right)} \tag{31}$$

As shown above, the rate constant for each reaction is increased/decreased by a factor of two and the related IDTs are calculated as τ^+ and τ^-, respectively. Also, the net flux values shown in the following figures are normalized with net fluxes of the corresponding reactions in the base condition (P2C2 for ethylene and P3C2 for ethane). Therefore, if there is no change in the net flux of a specific reaction, the normalized value is unity, otherwise it may be higher or lower than unity in accordance with any change in the net flux rates.

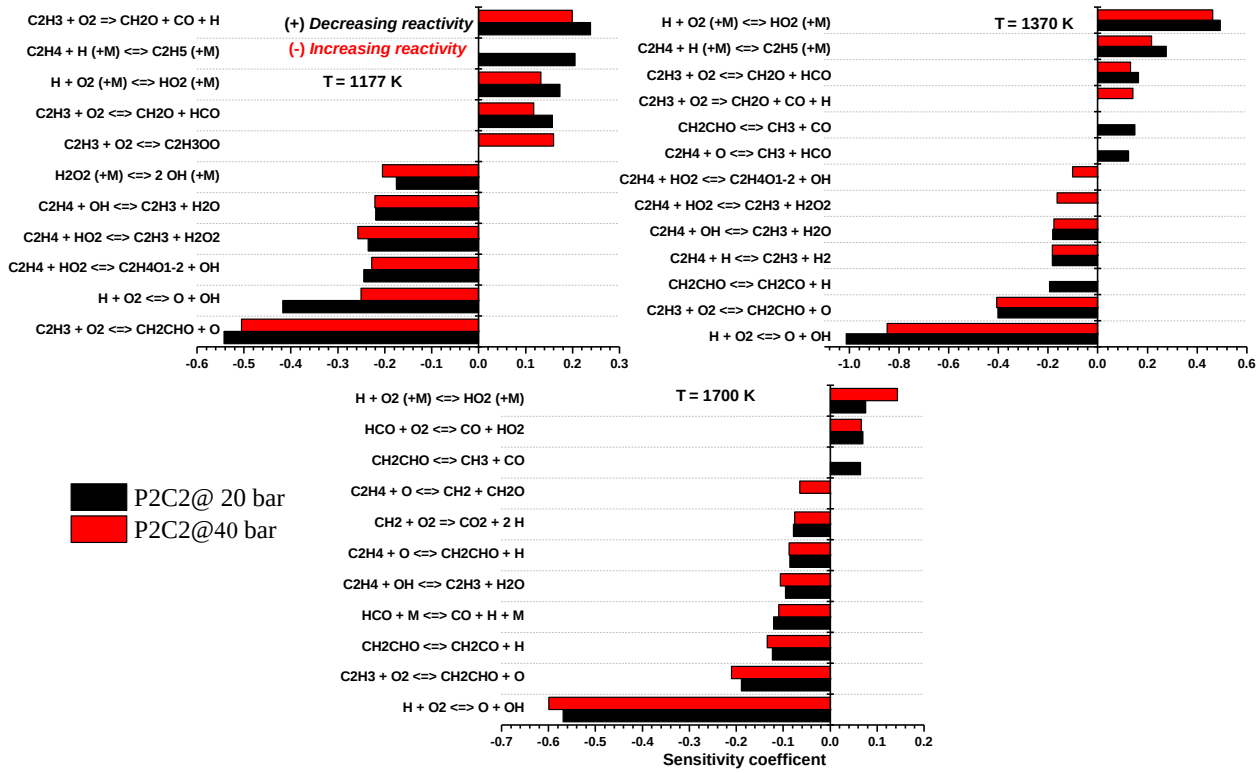

Figure S89. Effect of pressure on the ten most prominent reactions and their fluxes, brute force sensitivity analysis of IDT corresponding to lines (1–3) in Figures 6(a,d); P2C2: φ = 1.0, 75.0% N_2. (For better interpretation of the colours, the reader is referred to the web version of this article)

Table S20. Effect of pressure rise on the ten most prominent reactions of ethylene at different temperatures

Temperature (K)	Promoted reactions	Suppressed reactions
1177	$\dot{C}_2H_3 + O_2 \leftrightarrow \dot{C}_2H_3OO$	$C_2H_4 + \dot{H} \leftrightarrow \dot{C}_2H_5(+M)$
1370	$C_2H_4 + H\dot{O}_2 \leftrightarrow \dot{C}_2H_3 + H_2O_2$	$\dot{C}H_2CHO \leftrightarrow CH_2CO + \dot{H}$
	$C_2H_4 + H\dot{O}_2 \leftrightarrow C_2H_4O1 - 2 + \dot{O}H$	$C_2H_4 + \ddot{O} \leftrightarrow \dot{C}H_3 + H\dot{C}O$
	$\dot{C}_2H_3 + O_2 \rightarrow CH_2O + \ddot{C}O + \dot{H}$	$\dot{C}H_2CHO \leftrightarrow \dot{C}H_3 + \ddot{C}O$
1700	$C_2H_4 + \ddot{O} \rightarrow \ddot{C}H_2 + CH_2O$	$\dot{C}H_2CHO \leftrightarrow \dot{C}H_3 + \ddot{C}O$

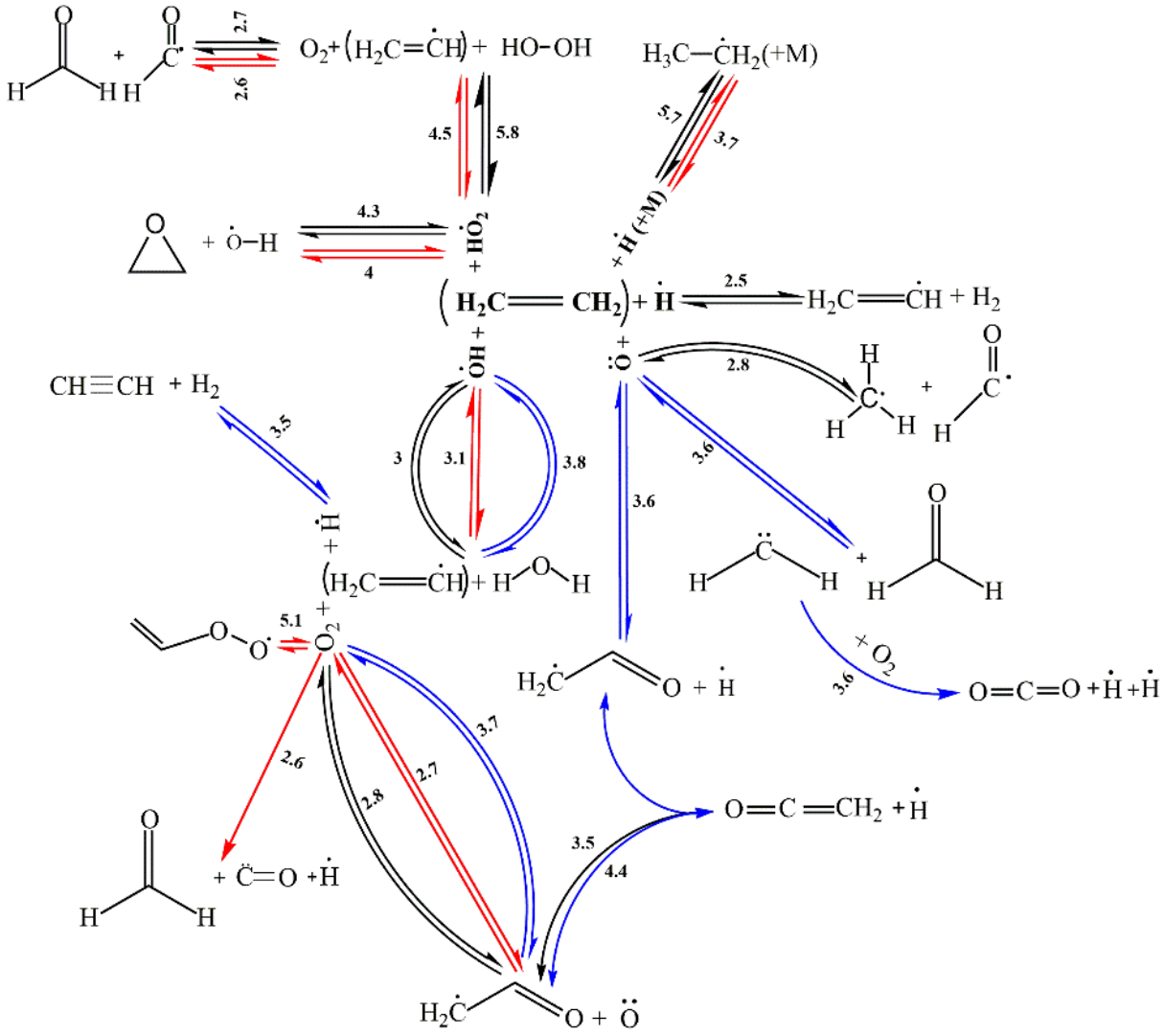

Figure S90. Effect of pressure on the normalized flux analysis of the ten most prominent reactions corresponding to lines (1–3) in Figures 6(a,d); P2C2: φ = 1.0, 75.0% N_2 (based on the flux analysis of P2C2 base case when 20% of ethylene (fuel) is consumed); the blue line: case (1), T = 1700 K, the black line: case (2), T = 1370 K, the red line: case (3), T = 1177 K (1112 K in Figure 6d). (For better interpretation of the colours, the reader is referred to the web version of this article)

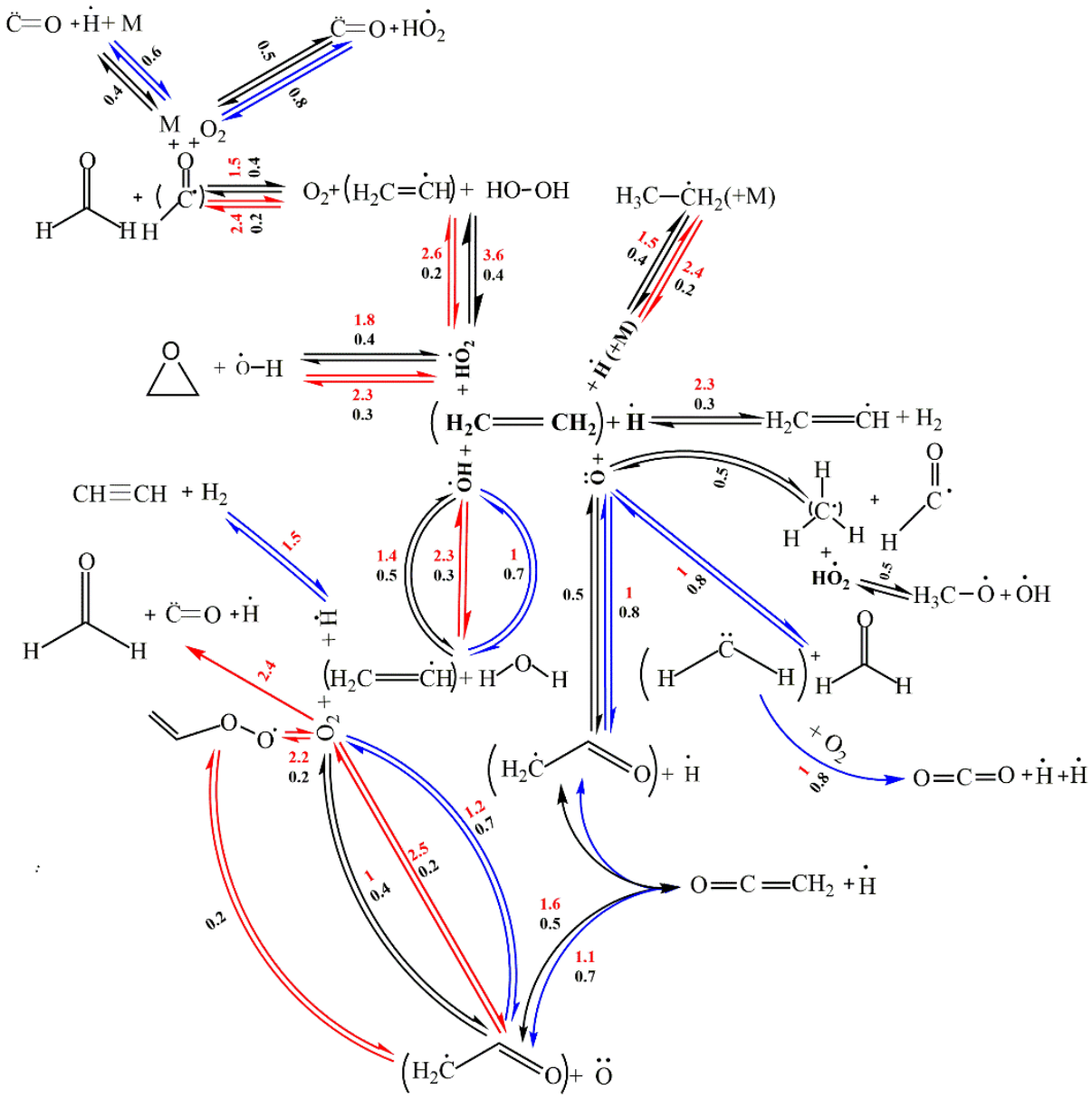

Figure S91. Effect of changing in equivalence ratio on the normalized flux analysis of the ten most prominent reactions corresponding to lines (1–3) in Figures 6(a,d); P2C2: φ = 1.0, 75.0% N_2, 20 bar, (based on the flux analysis of P2C2 base case when 20% of ethylene (fuel) is consumed); the blue line: case (1), T = 1700 K, the black line: case (2), T = 1370 K, the red line: case (3), T = 1177 K (φ = 2.0) and 1112 K (φ = 0.5); the red number: φ = 2.0, the black number: φ = 0.5. (For better interpretation of the colours, the reader is referred to the web version of this article)

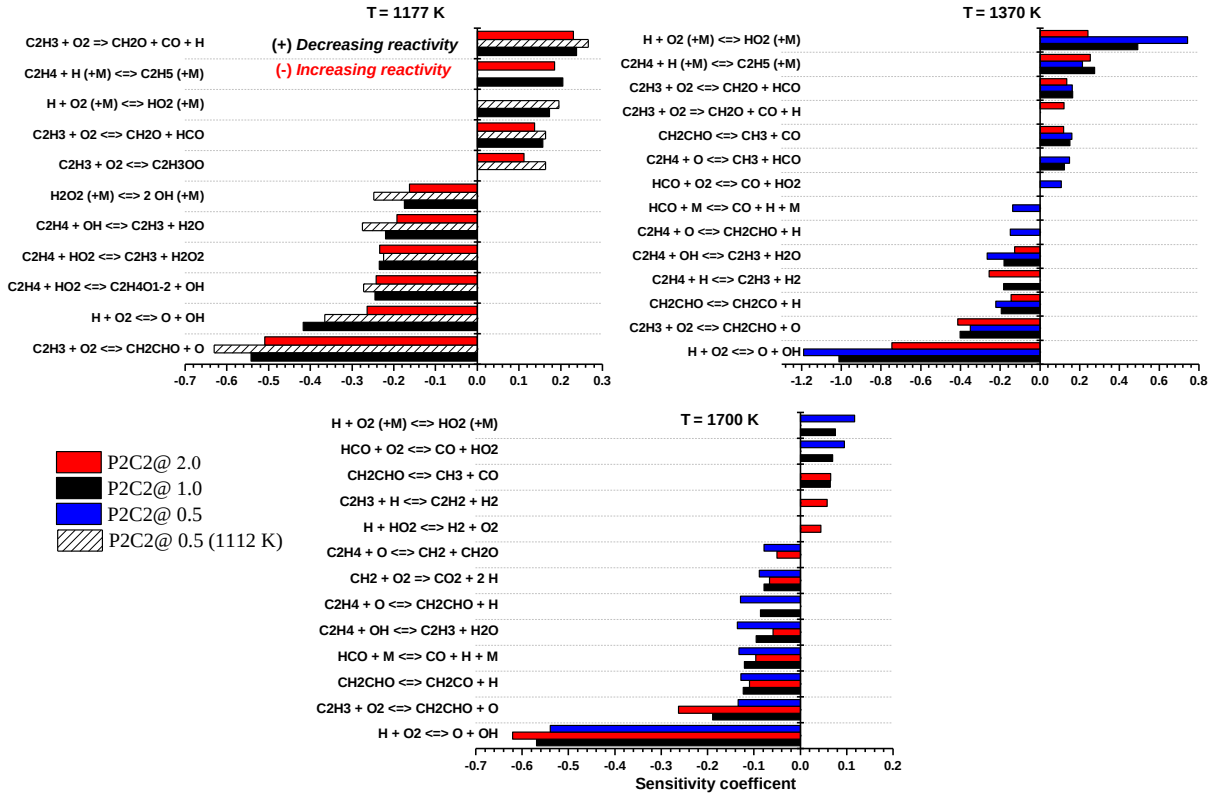

Figure S92. Effect of changing in equivalence ratio on the ten most prominent reactions, brute force sensitivity analysis of IDT corresponding to lines (1–3) in Figures 6(a,d); P2C2: φ = 1.0, 75.0% N_2, 20 bar (For better interpretation of the colours, the reader is referred to the web version of this article)

Table S21. Effect of increasing equivalence ratio on the ten most prominent reactions of ethylene at different temperatures in comparison to P2C2 case.

Temperature (K)	Promoted reactions	Suppressed reactions
1177	$\dot{C}_2H_3 + O_2 \leftrightarrow \dot{C}_2H_3OO$	$\dot{H} + O_2 \leftrightarrow H\dot{O}_2(+M)$
1370	$\dot{C}_2H_3 + O_2 \rightarrow CH_2O + \ddot{C}O + \dot{H}$	$C_2H_4 + \ddot{O} \leftrightarrow \dot{C}H_3 + H\dot{C}O$
1700	$C_2H_4 + \ddot{O} \leftrightarrow \ddot{C}H_2 + CH_2O$	$\dot{H} + O_2(+M) \leftrightarrow H\dot{O}_2(+M)$
	$\dot{H} + H\dot{O}_2 \leftrightarrow H_2 + O_2$	$C_2H_4 + \ddot{O} \leftrightarrow \dot{C}H_2CHO + \dot{H}$
	$\dot{C}_2H_3 + \dot{H} \leftrightarrow C_2H_2 + H_2$	$H\dot{C}O + O_2 \leftrightarrow \ddot{C}O + H\dot{O}_2$

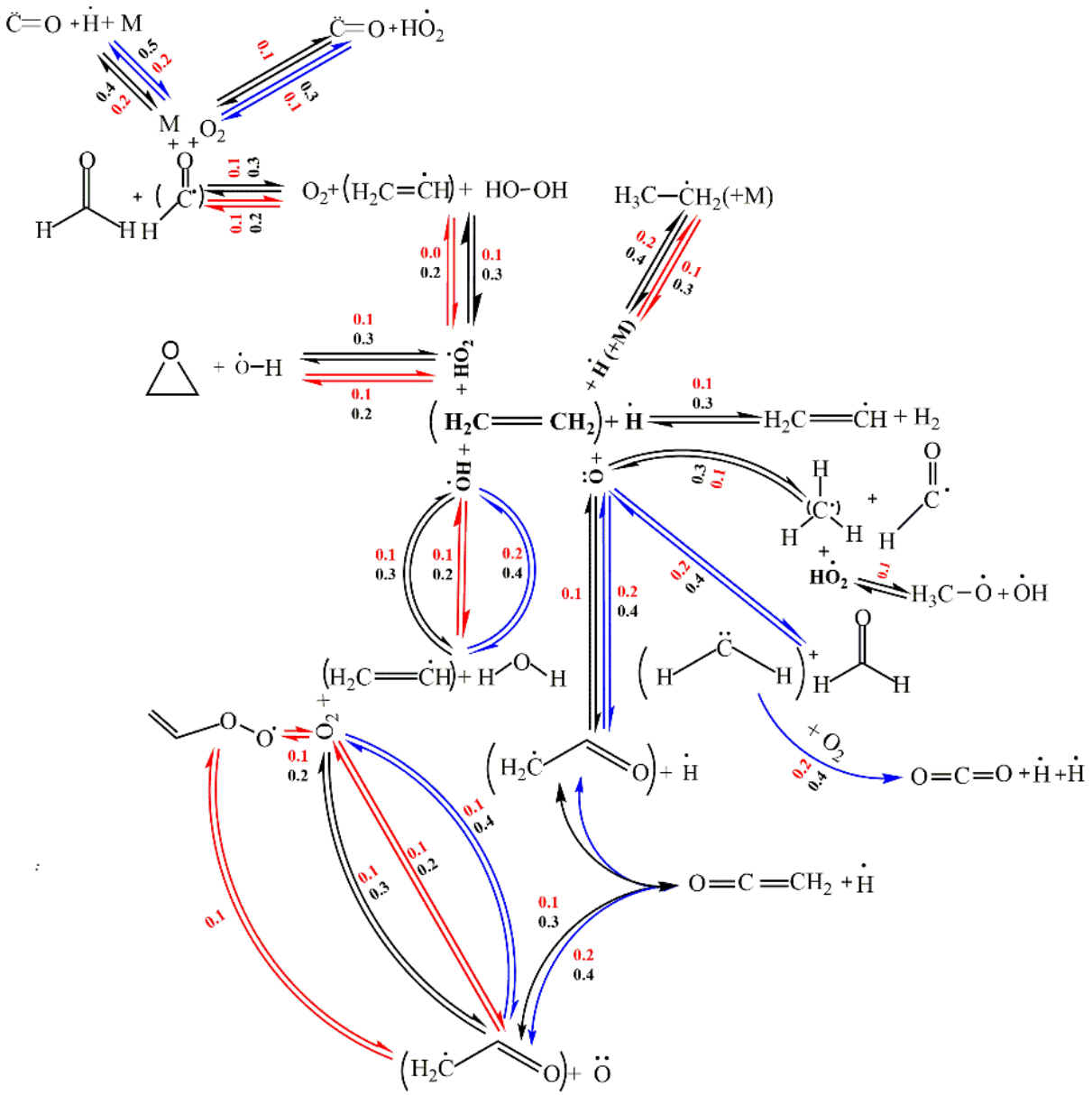

Figure S93. Effect of changing in dilution level on the normalized flux analysis of the ten most prominent reactions corresponding to lines (1–3) in Figures 6(c,d); P2C2: φ = 1.0, 75.0% N_2, 20 bar (based on the flux analysis of P2C2 base case when 20% of ethylene (fuel) is consumed); the blue line: case (1), T = 1700 K, the black line: case (2), T = 1370 K, the red line: case (3), T = 1177 K (85%) and 1112 K (90%); the red number: 90%, the black number: 85%.(For better interpretation of the colours, the reader is referred to the web version of this article)

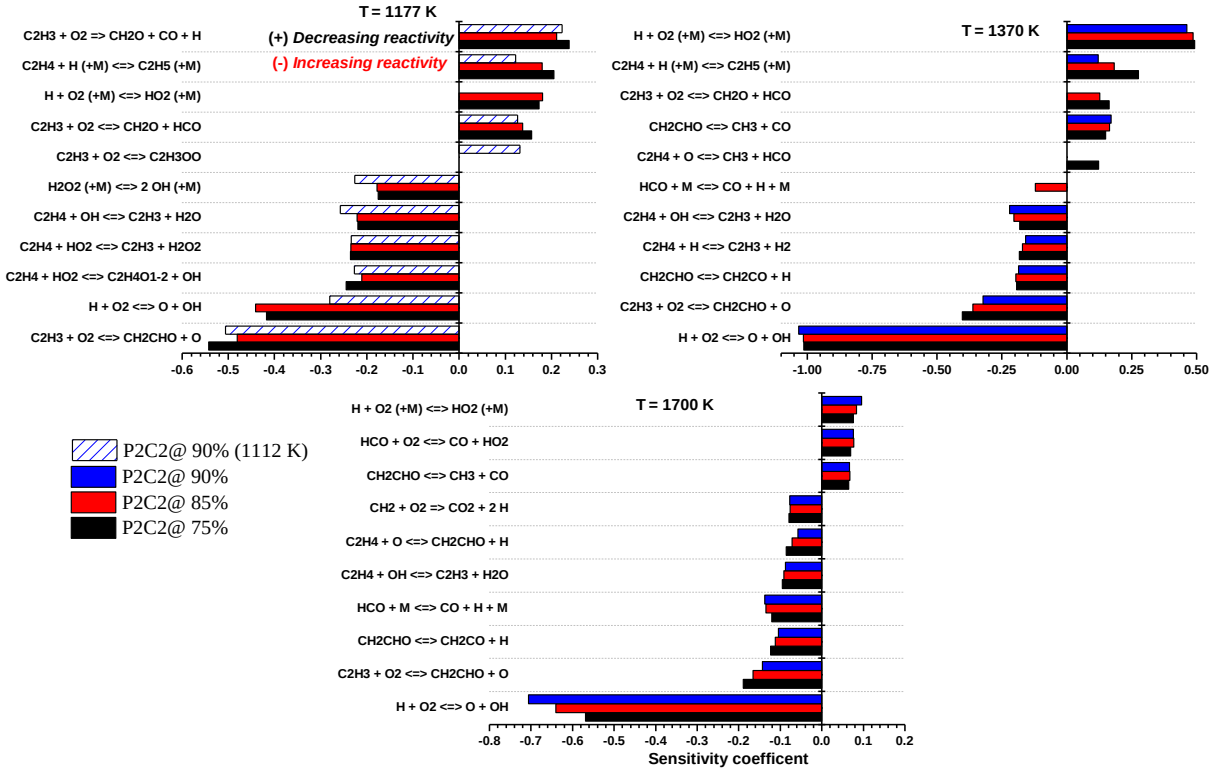

Figure S94. Effect of changing in dilution level on the ten most prominent reactions, brute force sensitivity analysis of IDT corresponding to lines (1–3) in Figures 6(c,d); P2C2: φ = 1.0, 75.0% N_2, 20 bar For better interpretation of the colours, the reader is referred to the web version of this article)

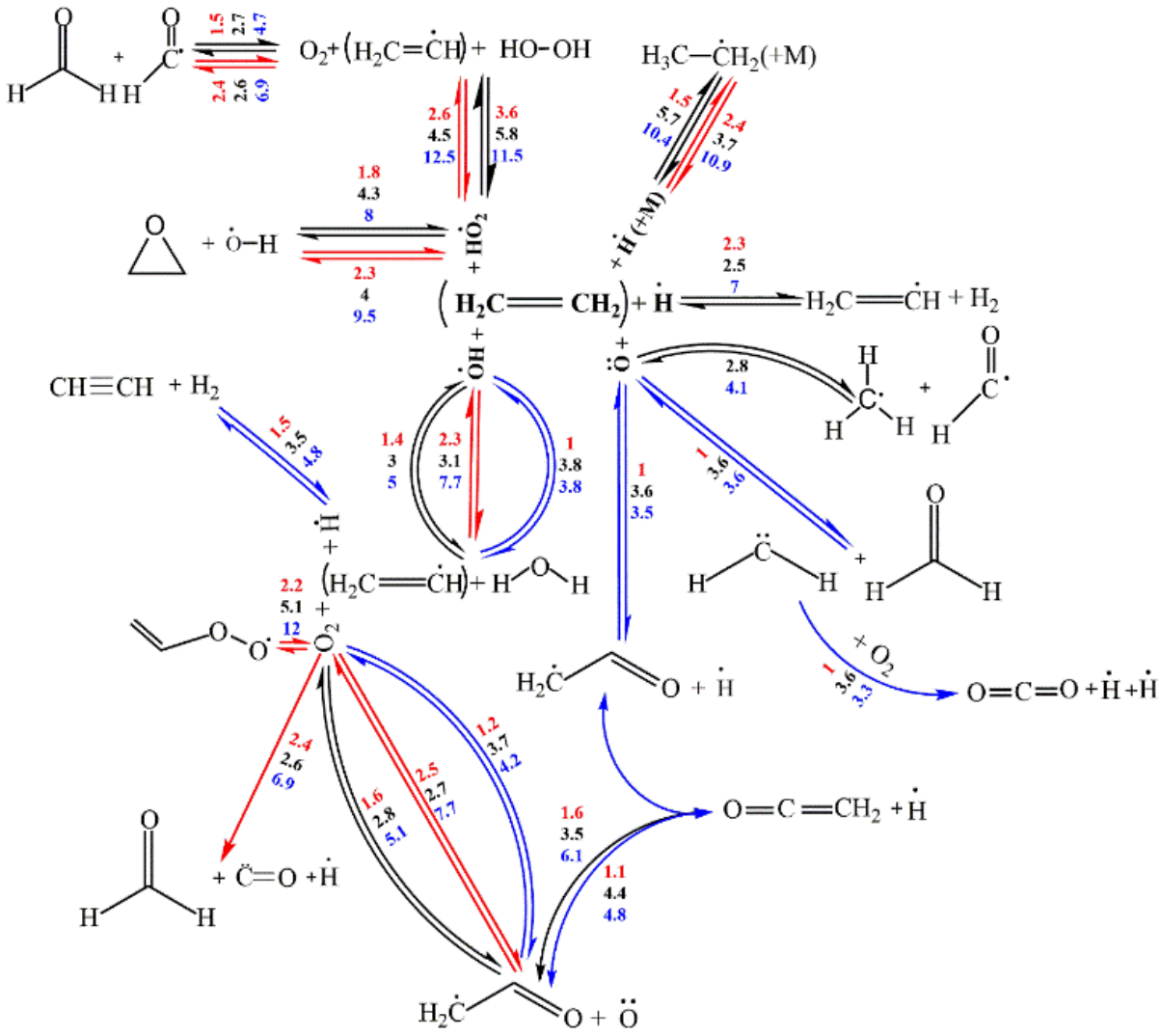

Figure S95. Normalized flux analysis (based on the flux analysis of P2C2 base case when 20% of ethylene (fuel) is consumed) of some important reactions corresponding to Figure 6a; the blue line: case (1), T = 1700 K, the black line: case (2), T = 1370 K, the red line: case (3), T = 1177 K; the red number: effect of equivalence ratio, the black number: effect of pressure, and the blue number: combined effects. (For better interpretation of the colours, the reader is referred to the web version of this article)

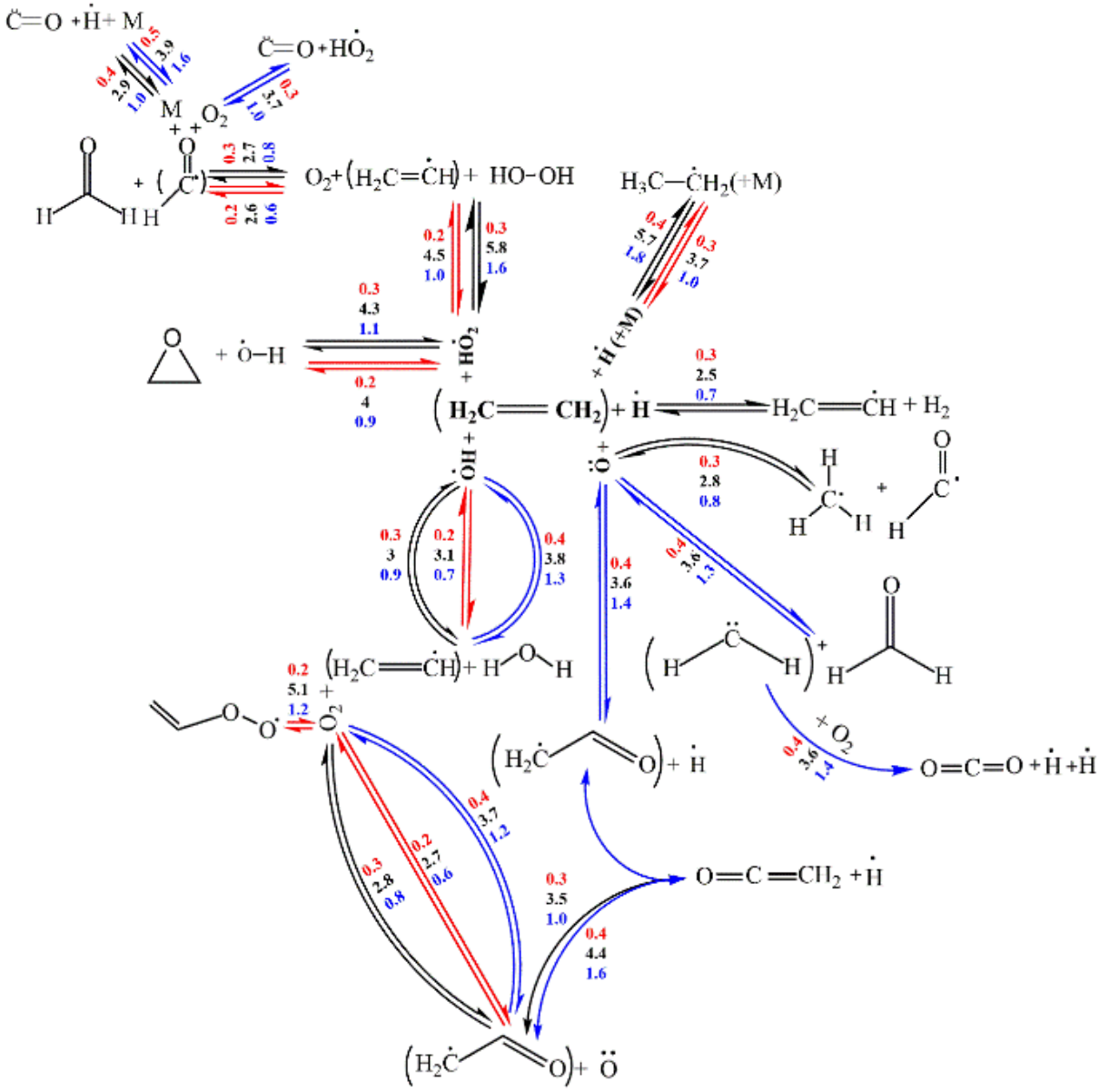

Figure S96. Normalized flux analysis (based on the flux analysis of P2C2 base case when 20% of ethylene (fuel) is consumed) of some important reactions corresponding to Figure 6c; the blue line: case (1), T = 1700 K, the black line: case (2), T = 1370 K, the red line: case (3), T = 1112 K; the red number: effect of dilution, the black number: effect of pressure, and the blue number: combined effects. (For better interpretation of the colours, the reader is referred to the web version of this article)

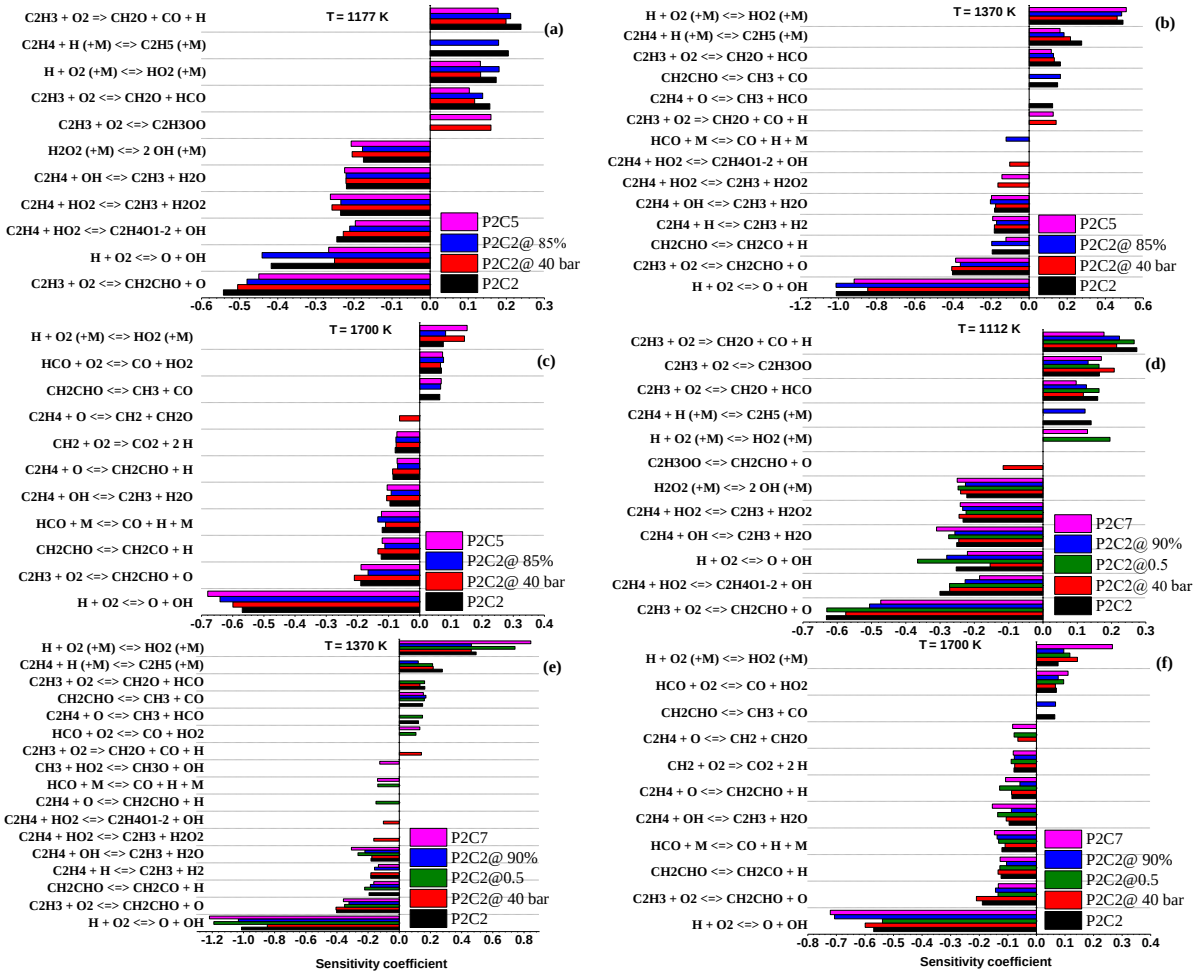

Figure S97. Brute force sensitivity analysis of IDT corresponding to lines (1–3) in Figure 6c: (a) T = 1177 K; (b) T = 1370 K; (c) T = 1700 K; and figure 7(d): (d) T = 1112 K; (e) T = 1370 K; (f) T = 1700 K.

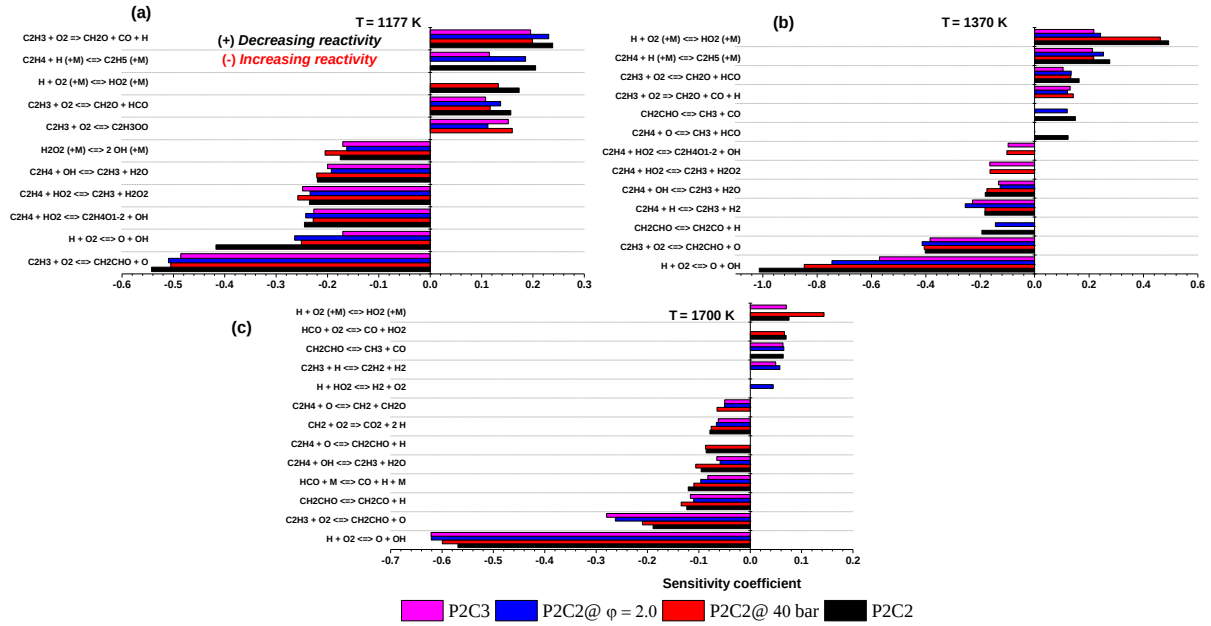

Figure S98. Brute force sensitivity analysis of IDT corresponding to lines (1–3) in Figure 6a: (a) T = 1177 K; (b) T = 1370 K; (c) T = 1700 K.

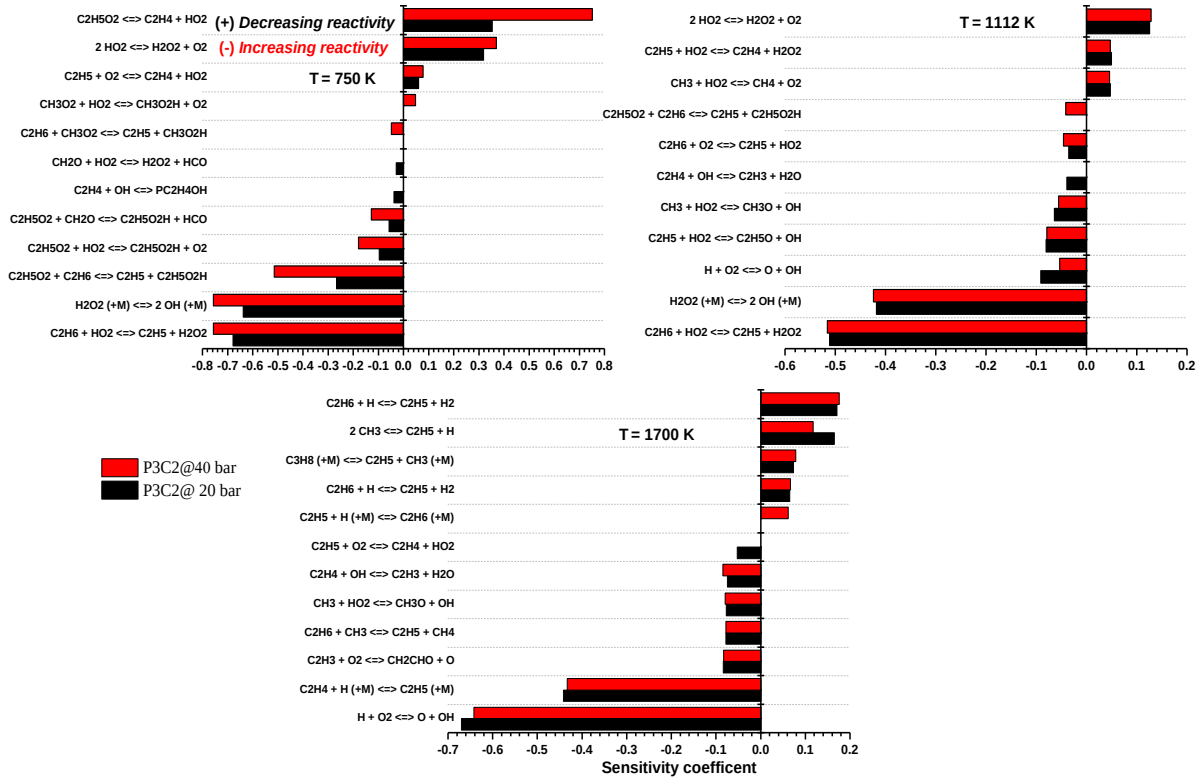

Figure S99. Effect of pressure on the ten most prominent reactions, brute force sensitivity analysis of IDT corresponding to lines (1–3) in Figure 8d; P3C2: φ = 1.0, 75% N_2, 20 bar. (For better interpretation of the colours, the reader is referred to the web version of this article)

Table S22. Effect of increasing pressure on the ten most prominent reactions of ethane at different temperatures in comparison to P3C2 case.

Temperature (K)	Promoted reactions	Suppressed reactions
750	$C_2H_6 + H\dot{O}_2 \leftrightarrow \dot{C}_2H_5 + CH_3O_2H$	$C_2H_4 + \dot{O}H \leftrightarrow P\dot{C}_2H_4OH$
	$CH_3\dot{O}_2 + H\dot{O}_2 \leftrightarrow CH_3O_2H + O_2$	$CH_2O + H\dot{O}_2 \leftrightarrow H_2O_2 + H\dot{C}O$
1112	$C_2H_5\dot{O}_2 + C_2H_6 \rightarrow \dot{C}_2H_5 + C_2H_5O_2H$	$C_2H_4 + \dot{O}H \leftrightarrow \dot{C}_2H_3 + H_2O$
1700	$\dot{C}_2H_5 + \ddot{H}(+M) \leftrightarrow C_2H_6(+M)$	$\dot{C}_2H_5 + O_2 \leftrightarrow C_2H_4 + H\dot{O}_2$

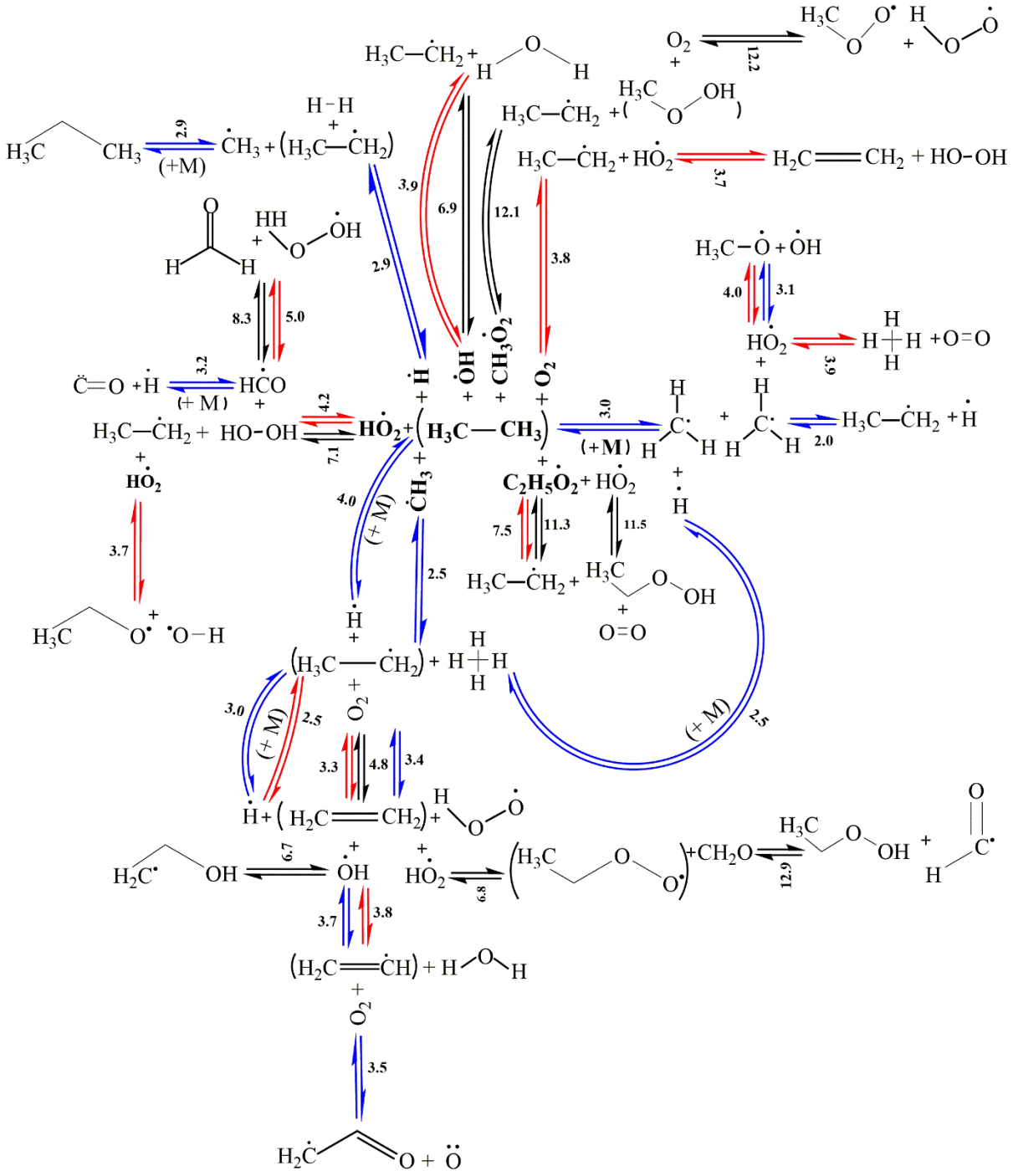

Figure S100. Effect of pressure on the normalized flux analysis of ten most prominent reactions of ethane corresponding to lines (1–3) in Figure 8d; P3C2: φ = 1.0, 75% N_2, 20 bar, (based on the flux analysis of P3C2 base case when 20% of ethane (fuel) is consumed); the blue line: case (1), T = 1700 K, the red line: case (2), T = 1112 K, the black line: case (3), T = 750 K. (For better interpretation of the colours, the reader is referred to the web version of this article)

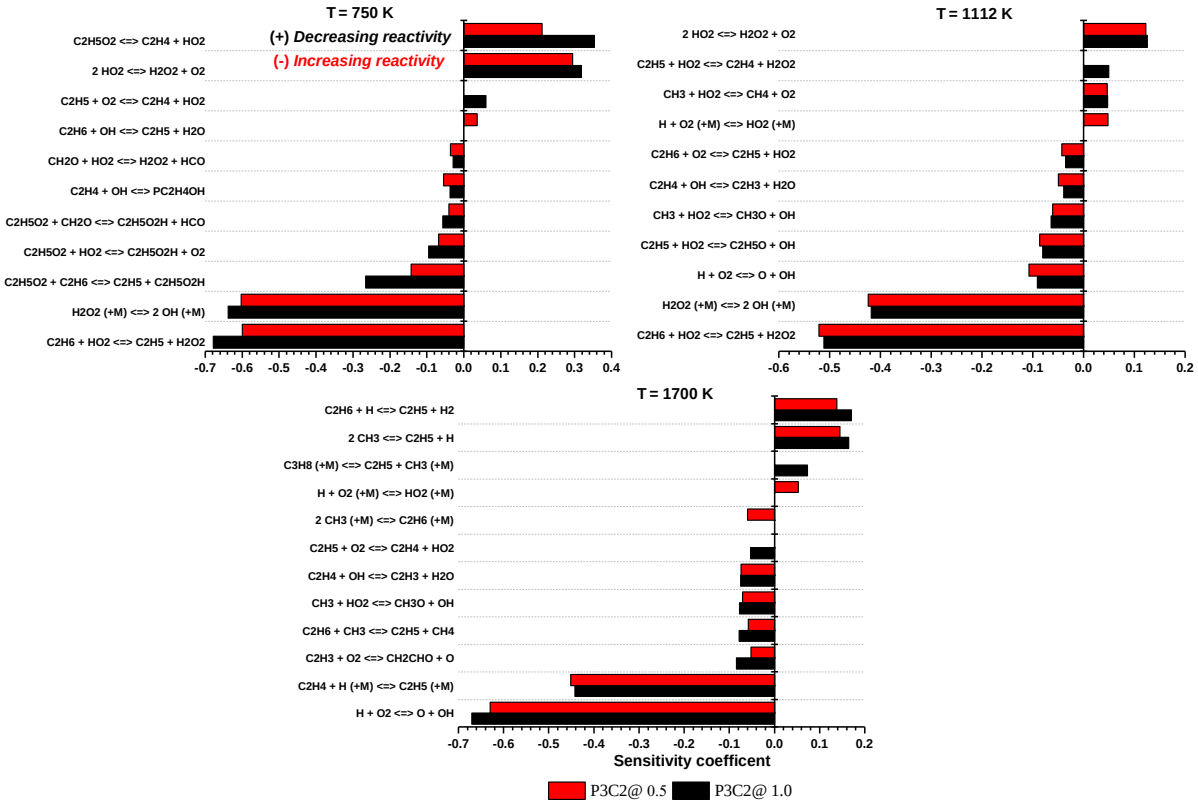

Figure S101. Effect of equivalence ratio on the ten most prominent reactions, brute force sensitivity analysis of IDT corresponding to lines (1–3) in Figures 8(b,d); P3C2: φ = 1.0, 75% N_2, 20 bar. (For better interpretation of the colours, the reader is referred to the web version of this article)

Table S23. Effect of decreasing equivalence ratio on the ten most prominent reactions of ethane at different temperatures in comparison to P3C2 case.

Temperature (K)	Promoted reactions	Suppressed reactions
750	$C_2H_6 + \dot{O}H \leftrightarrow \dot{C}_2H_5 + H_2O$	$\dot{C}_2H_5 + O_2 \leftrightarrow C_2H_4 + H\dot{O}_2$
1112	$\dot{H} + O_2(+M) \rightarrow HO_2(+M)$	$\dot{C}_2H_5 + H\dot{O}_2 \leftrightarrow C_2H_4 + H_2O_2$
1700	$\dot{C}H_3 + \dot{C}H_3(+M) \leftrightarrow C_2H_6(+M)$	$C_3H_8(+M) \leftrightarrow \dot{C}_2H_5 + CH_3(+M)$
		$C_2H_6 + \dot{H} \leftrightarrow \dot{C}_2H_5 + H_2$
	$\dot{H} + O_2(+M) \leftrightarrow H\dot{O}_2(+M)$	
		$\dot{C}_2H_5 + O_2 \leftrightarrow C_2H_4 + H\dot{O}_2$

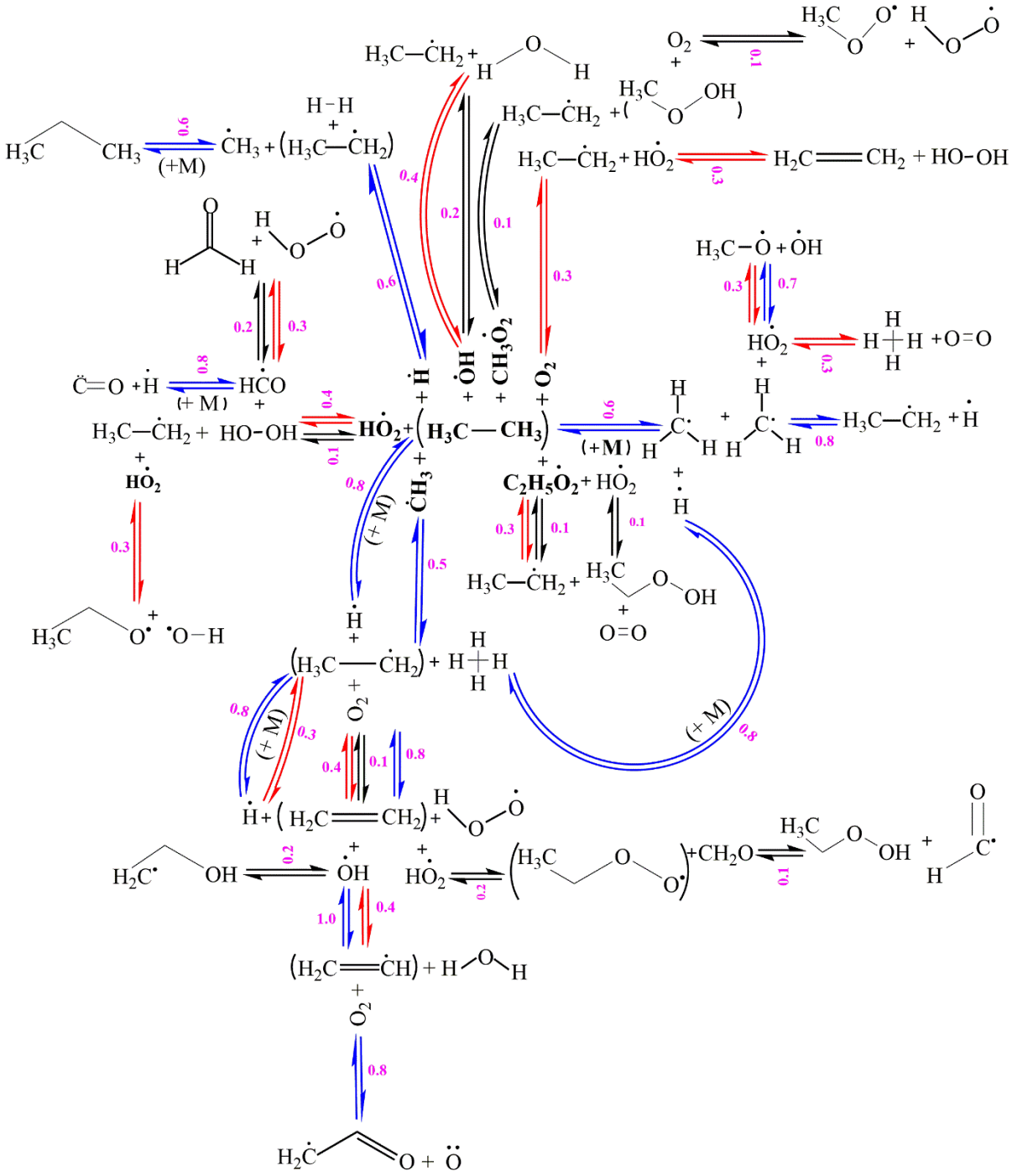

Figure S102. Effect of equivalence ratio on the normalized flux analysis of ten most prominent reactions of ethane corresponding to lines (1–3) in Figures 8(b,d); P3C2: φ = 1.0, 75% N_2, 20 bar (based on the flux analysis of P3C2 base case when 20% of ethane (fuel) is consumed); the blue line: case (1), T = 1700 K, the red line: case (2), T = 1112 K, the black line: case (3), T = 750 K. (For better interpretation of the colours, the reader is referred to the web version of this article)

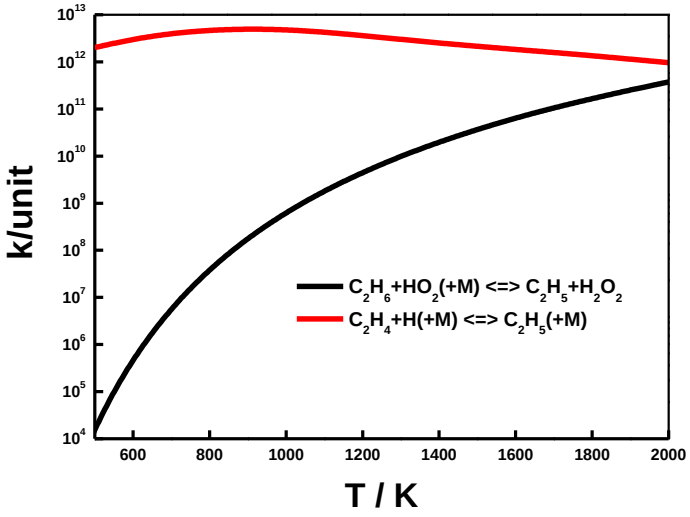

Figure S103. A comparison between two important reactions involved in the effect of equivalence ratio on ethane oxidation.

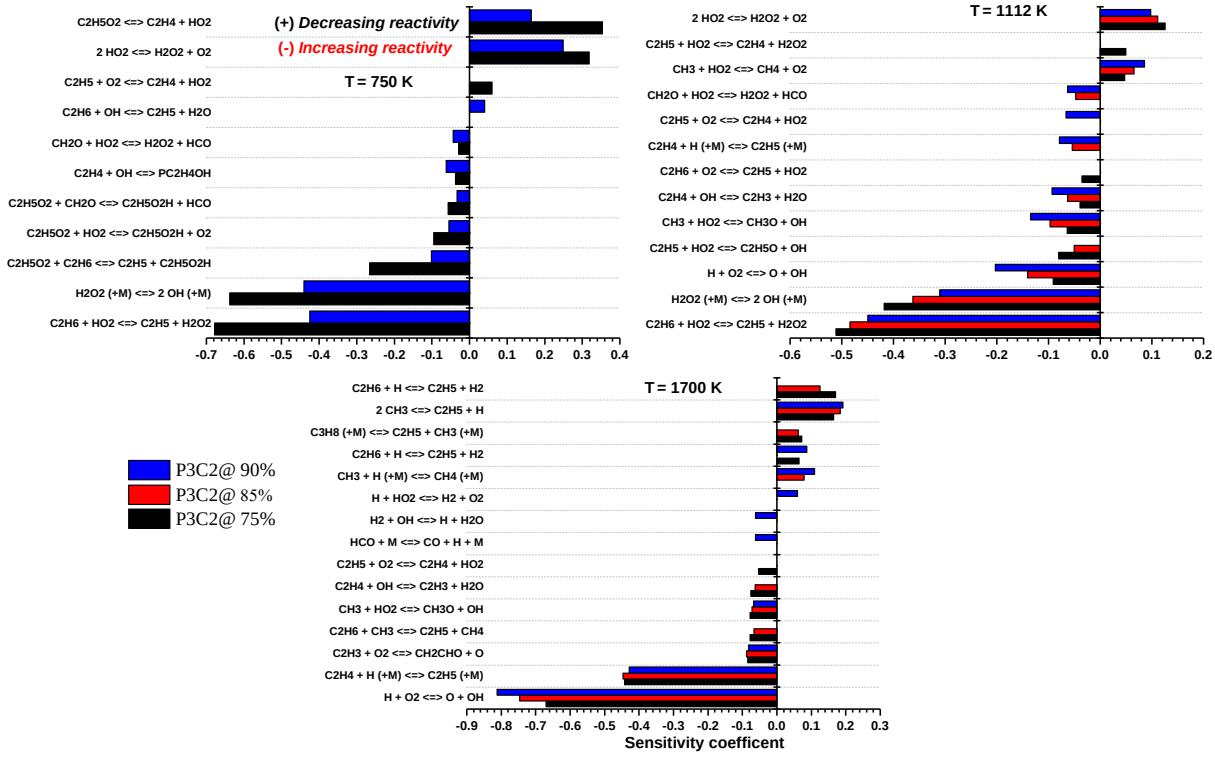

Figure S104. Effect of dilution level on the ten most prominent reactions and their fluxes, brute force sensitivity analysis of IDT corresponding to lines (1–3) in Figures 8(b,d); P3C2: φ = 1.0, 75% N_2, 20 bar (For better interpretation of the colours, the reader is referred to the web version of this article)

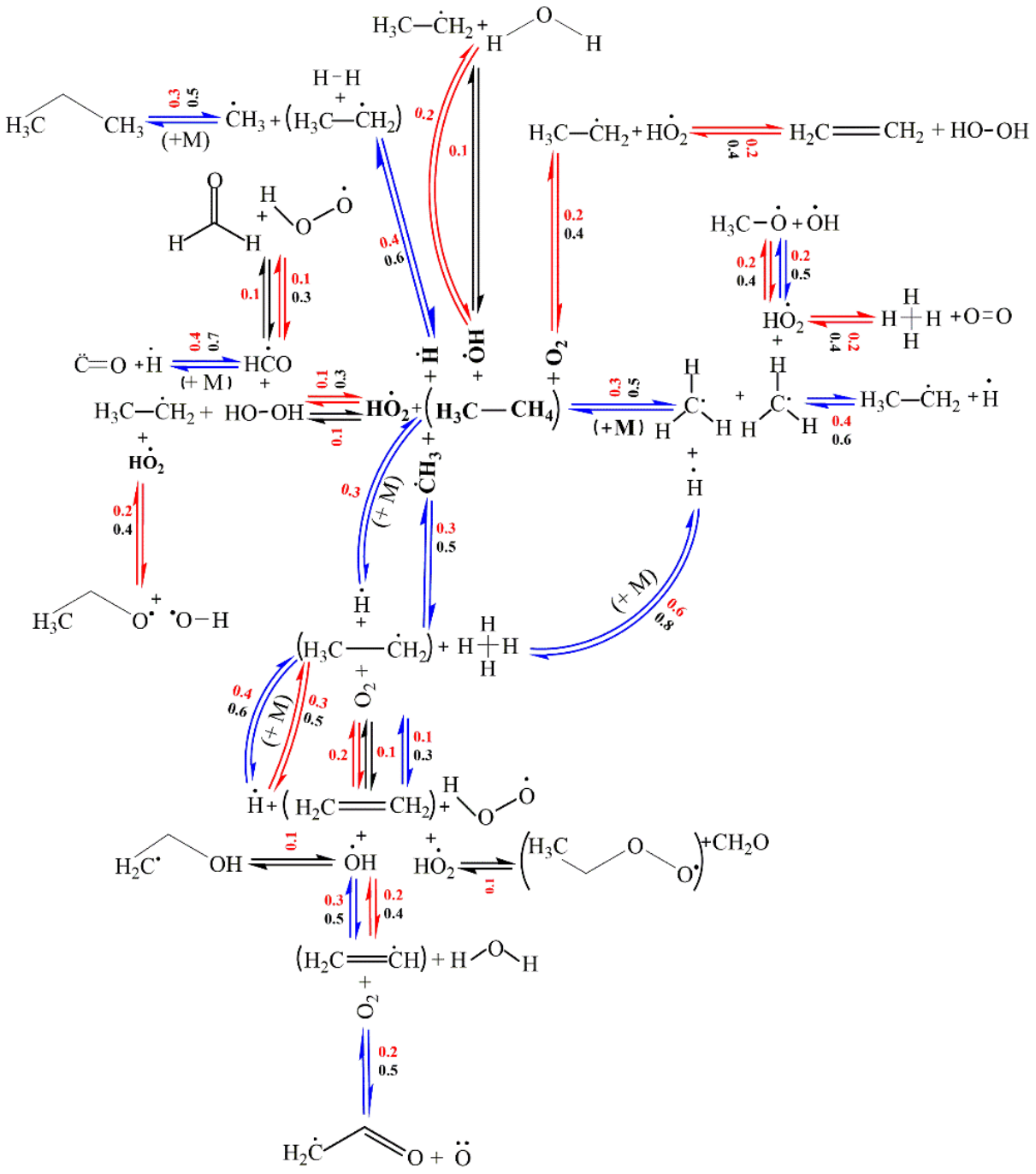

Figure S105. Effect of dilution level on the normalized flux analysis of the ten most prominent reactions corresponding to lines (1–3) in Figures 8(b,d); P3C2: φ = 1.0, 75% N_2, 20 bar (based on the flux analysis of P3C2 base case when 20% of ethane (fuel) is consumed); the blue line: case (1), T = 1700 K, the red line: case (2), T = 1112 K, the black line: case (3), T = 750 K; the red number: 90% and the black number: 85% (For better interpretation of the colours, the reader is referred to the web version of this article)

Table S24. Effect of increasing dilution (75% → 85%, Figure 8b) on the ten most prominent reactions of ethane at different temperatures in comparison to P3C2 case.

Temperature (K)	Promoted reactions	Suppressed reactions
1112	$C_2H_4 + \dot{H}\ (+M) \leftrightarrow \dot{C}_2H_5(+M)$	$C_2H_6 + O_2 \rightarrow \dot{C}_2H_5 + HO_2$
	$CH_2O + H\dot{O}_2 \leftrightarrow H_2O_2 + H\dot{C}O$	$\dot{C}_2H_5 + H\dot{O}_2 \leftrightarrow C_2H_4 + H_2O_2$
1700	$\dot{C}H_3 + \dot{H}\ (+M) \leftrightarrow CH_4\ (+M)$	$\dot{C}_2H_5 + O_2 \leftrightarrow C_2H_4 + H\dot{O}_2$

Table S25. Effect of increasing dilution (75% → 90% Figure 8d) on the ten most prominent reactions of ethane at different temperatures in comparison to P3C2 case.

Temperature (K)	Promoted reactions	Suppressed reactions
750	$C_2H_6 + \dot{O}H \leftrightarrow \dot{C}_2H_5 + H_2O$	$\dot{C}_2H_5 + O_2 \leftrightarrow C_2H_4 + H\dot{O}_2$
1112	$C_2H_4 + \dot{H}\ (+M) \leftrightarrow \dot{C}_2H_5(+M)$	$C_2H_6 + O_2 \rightarrow \dot{C}_2H_5 + HO_2$
	$CH_2O + H\dot{O}_2 \leftrightarrow H_2O_2 + H\dot{C}O$	$\dot{C}_2H_5 + H\dot{O}_2 \leftrightarrow C_2H_4 + H_2O_2$
	$\dot{C}_2H_5 + O_2 \leftrightarrow C_2H_4 + H\dot{O}_2$	$\dot{C}_2H_5 + H\dot{O}_2 \leftrightarrow C_2H_5\dot{O} + \dot{O}H$
1700	$\dot{C}H_3 + \dot{H}\ (+M) \leftrightarrow CH_4\ (+M)$	$C_2H_6 + \dot{H} \leftrightarrow \dot{C}_2H_5 + H_2$
	$H\dot{C}O + M \leftrightarrow \ddot{C}O + \dot{H} + M$	$C_3H_8(+M) \leftrightarrow \dot{C}_2H_5 + CH_3(+M)$
		$C_2H_4 + \dot{O}H \leftrightarrow \dot{C}_2H_3 + H_2O$
	$H_2 + \dot{O}H \leftrightarrow \dot{H} + H_2O$	$C_2H_6 + \dot{C}H_3 \leftrightarrow \dot{C}_2H_5 + CH_4$
	$\dot{H} + H\dot{O}_2 \leftrightarrow H_2 + O_2$	$\dot{C}_2H_5 + O_2 \leftrightarrow C_2H_4 + H\dot{O}_2$

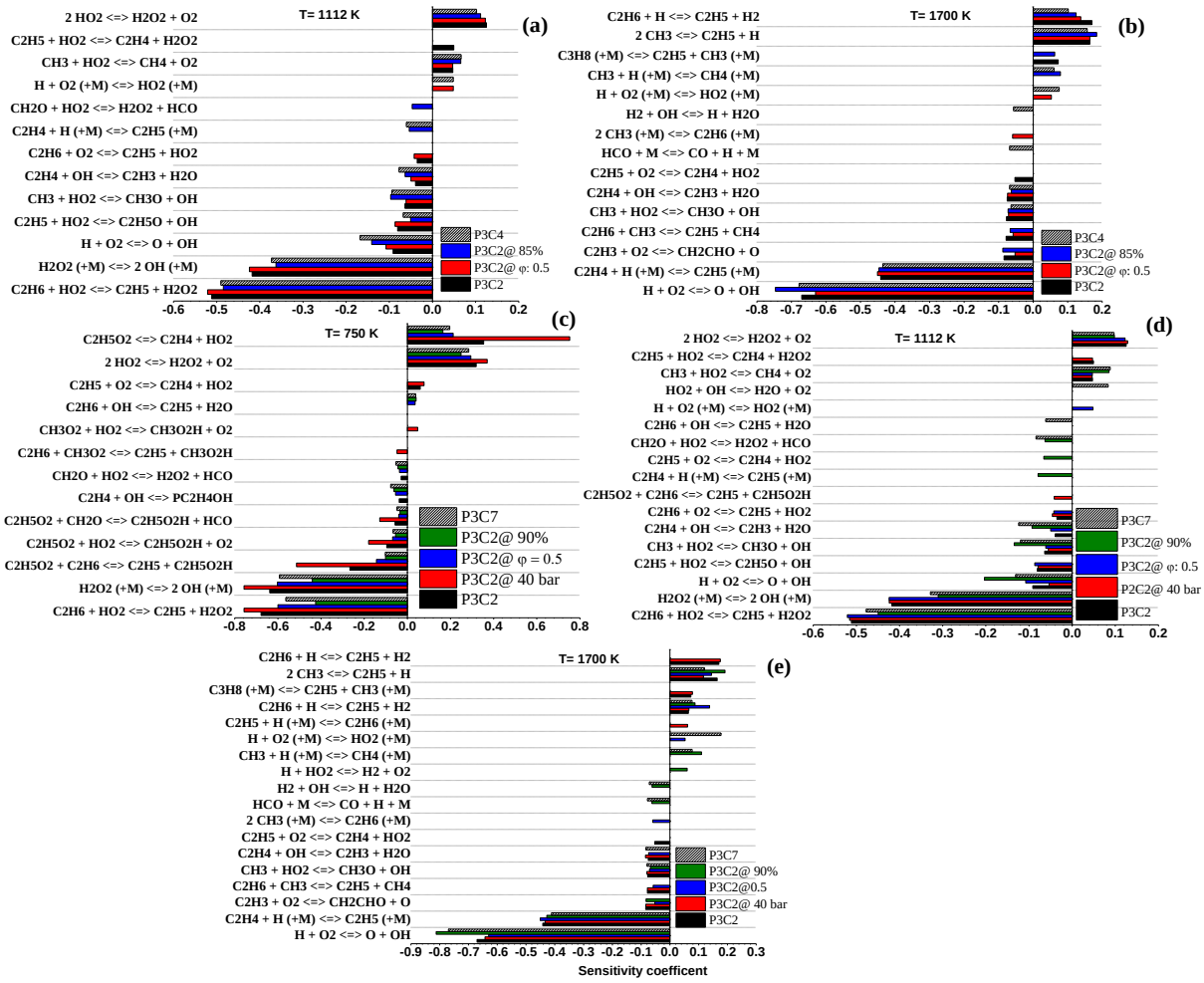

Figure S106. Brute force sensitivity analysis of IDT corresponding to lines (1–3) in Figures 8(b,d).

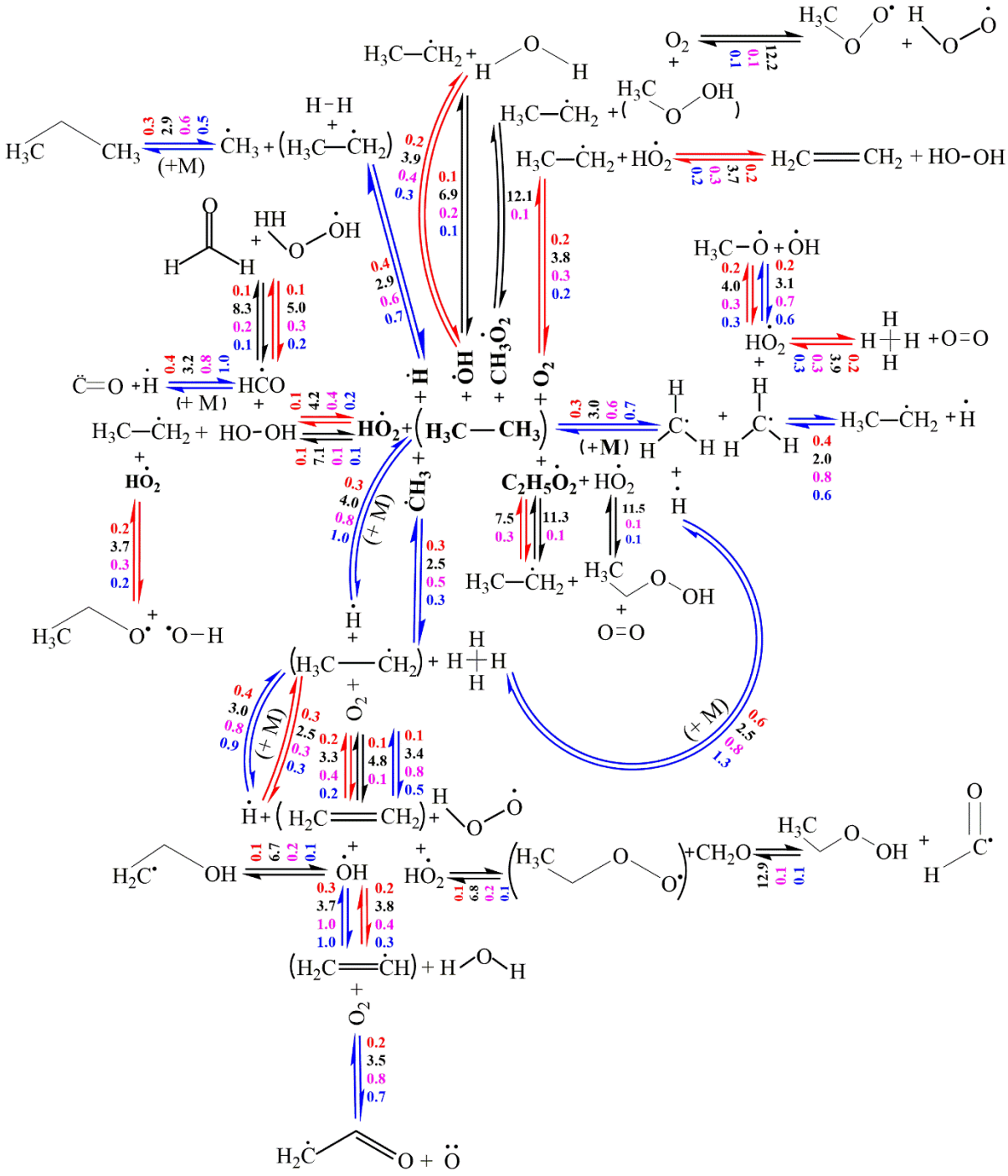

Figure S107. Normalized flux analysis (based on the flux analysis of P3C2 base case when 20% of ethane (fuel) is consumed) of some important reactions shown in Figures S99–106 corresponding to Figures 8(b,d); the blue line: case (1), T = 1700 K, the red line: case (2), T = 1112 K, and the black line: case (3), *T* = 750 K; the red number: effect of dilution, the black number: effect of pressure, the magenta number: effect of equivalence ratio, and the blue number: combined effects (P3C7). (For better interpretation of the colours, the reader is referred to the web version of this article)

12 Correlations

In this section, all the correlations and their relevant parameters derived individually for methane, ethylene, and ethane mixtures over a wide range of pressure, temperature, equivalence ratio, and

dilution (based on the C^3–NUIG comprehensive mechanism) have been presented in Table S26 to Table S36, respectively.

Table S26. Evaluated coefficients for correlation of the simulated IDTs for low–temperature methane mixtures.

$0.25 \leq \varphi \leq 3.0$ $75 \leq Dilution \leq 95\%$	$20 \leq p_{5,c} \leq 50$ /atm $800 \leq T_{5,c} \leq 1000$ /K
A	-6.671 ± 0.0439
B	14971.6 ± 73.50
C	-0.6812 ± 0.0031
D	-0.2510 ± 0.00455
E	-0.0784 ± 0.00934
R^2	0.98418
χ^2	0.00422

Table S27. Evaluated coefficients for correlation of the simulated IDTs for fuel–lean, low pressure methane mixtures.

$0.25 \leq \varphi \leq 1.0$ $75 \leq Dilution \leq 95\%$	$1 \leq p_{5,c} < 2$ /atm	
	$1000 \leq T_{5,c} < 1400$ /K	$1400 \leq T_{5,c} \leq 2000$ /K
A	-7.213 ± 0.033	-10.238 ± 0.007
B	17393.913 ± 63.785	26290.948 ± 20.224
C	0.2636 ± 0.0053	0.4025± 0.0013
D	-1.664 ± 0.007	-1.341 ± 0.002
E	0.3001 ± 0.007	0.2033 ± 0.0024
R^2	0.9940	0.9992
χ^2	5.7E-4	3.83E-9

Table S28. Evaluated coefficients for correlation of the simulated IDTs for fuel–lean methane mixtures.

$0.25 \leq \varphi \leq 1.0$ $75 \leq Dilution \leq 95\%$	$2 \leq p_{5,c} < 18$ /atm		$18 \leq p_{5,c} \leq 50$ /atm	
	$1000 \leq T_{5,c} < 1400$ /K	$1400 \leq T_{5,c} \leq 2000$ /K	$1000 \leq T_{5,c} < 1400$ /K	$1400 \leq T_{5,c} \leq 2000$ /K
A	-7.509 ± 0.0269	-10.064 ± 0.0181	-6.151 ± 0.0388	-9.872 ± 0.0141
B	18340.12 ± 61.24	25519.76 ± 61.30	14203.23 ± 72.16	24515.61 ± 43.09
C	0.4181 ± 0.0043	0.3268 ± 0.00301	-0.3979 ± 0.00546	0.2702 ± 0.00216
D	-1.704 ± 0.0052	-1.2890 ± 0.00357	-1.275± 0.0086	-1.439 ± 0.0026
E	0.2342 ± 0.0056	0.2143 ± 0.00299	0.3804 ± 0.01321	0.3329 ± 0.00381
R^2	0.99625	0.997	0.98213	0.99713
χ^2	0.0015	2.81549E-9	1.40601E-5	5.00059E-11

Table S29. Evaluated coefficients for correlation of the simulated IDTs for fuel–rich, low–pressure methane mixtures.

$1.0 < \varphi \leq 3.0$ $75 \leq Dilution \leq 95\%$	$1 \leq p_{5,c} < 2$ /atm	
	$1000 \leq T_{5,c} < 1400$ /K	$1400 \leq T_{5,c} \leq 2000$ /K
A	-6.653 ± 0.035	-11.011 ± 0.007
B	15797.165 ± 63.8	27930.373 ± 19.066
C	0.189 ± 0.0063	0.2931 ± 0.0019
D	-1.650 ± 0.007	-1.386 ± 0.002

E	0.3795 ± 0.0083	0.3908 ± 0.0018
R^2	0.9821	0.9993
χ^2	0.01015	2.09E-8

Table S30. Evaluated coefficients for correlation of the simulated IDTs for fuel–rich methane mixtures.

$1 < \varphi \leq 3.0$	$2 \leq p_{5,c} < 18$ /atm		$18 \leq p_{5,c} \leq 50$ /atm	
$75 \leq Dilution \leq 95\%$	$1000 \leq T_{5,c} < 1400$ /K	$1400 \leq T_{5,c} \leq 2000$ /K	$1000 \leq T_{5,c} < 1400$ /K	$1400 \leq T_{5,c} \leq 2000$ /K
A	-7.802 ± 0.0199	-10.865 ± 0.0144	-4.738 ± 0.0376	-10.271 ± 0.0080
B	18448.14 ± 44.92	27588.99 ± 48.57	12466.82 ± 60.25	25468.16 ± 24.41
C	0.3263 ± 0.00452	0.2843 ± 0.00332	-0.0697 ± 0.0102	0.2424 ± 0.0019
D	-1.830 ± 0.0046	-1.350 ± 0.0034	-1.873 ± 0.0103	-1.554 ± 0.0019
E	0.3785 ± 0.00477	0.3619 ± 0.00228	0.2624 ± 0.01547	0.4447 ± 0.00218
R^2	0.99742	0.99808	0.97586	0.99899
χ^2	0.00858	1.12508E-8	5.62546E-5	1.34144E-10

Table S31. Evaluated coefficients for correlation of the simulated IDTs for low–temperature ethylene mixtures.

$0.25 \leq \varphi \leq 3.0$	$1 \leq p_{5,c} \leq 50$ /atm
$75 \leq Dilution \leq 95\%$	$800 \leq T_{5,c} < 1000$ /K
A	-10.492 ± 0.0263
B	19936.06 ± 48.24
C	-0.8030 ± 0.00149
D	-0.0624 ± 0.00209
E	0.0331 ± 0.00221
R^2	0.99639
χ^2	0.00269

Table S32. Evaluated coefficients for correlation of the simulated IDTs for fuel–lean ethylene mixtures.

$0.25 \leq \varphi \leq 1.0$	$1 \leq p_{5,c} < 18$ /atm		$18 \leq p_{5,c} \leq 50$ /atm	
$75 \leq Dilution \leq 95\%$	$1000 \leq T_{5,c} < 1250$ /K	$1250 \leq T_{5,c} \leq 2000$ /K	$1000 \leq T_{5,c} < 1500$ /K	$1500 \leq T_{5,c} \leq 2000$ /K
A	-13.637 ± 0.1978	-7.422 ± 0.0072	-10.321 ± 0.0125	-9.219 ± 0.0181
B	26956.76 ± 460.66	10029.53 ± 24.17	19335.80 ± 26.90	13917.03 ± 49.31
C	-0.0857 ± 0.01535	-0.2327 ± 0.00228	-0.7194 ± 0.00142	-0.2288 ± 0.00356
D	-0.6622 ± 0.01892	-0.6570 ± 0.00296	-0.1085 ± 0.00179	-0.5751 ± 0.00454
E	0.3652 ± 0.01448	-0.0288 ± 0.00285	0.1582 ± 0.00265	0.2716 ± 0.00674
R^2	0.91273	0.9969	0.99884	0.98511
χ^2	2.97089E-6	6.58757E-13	4.85452E-9	3.40205E-14

Table S33. Evaluated coefficients for correlation of the simulated IDTs for fuel–rich ethylene mixtures.

$1 < \varphi \leq 3.0$	$1 \leq p_{5,c} < 18$ /atm		$18 \leq p_{5,c} \leq 50$ /atm	
$75 \leq Dilution \leq 95\%$	$1000 \leq T_{5,c} < 1400$ /K	$1400 \leq T_{5,c} \leq 2000$ /K	$1000 \leq T_{5,c} < 1650$ /K	$1650 \leq T_{5,c} \leq 2000$ /K
A	-12.533 ± 0.0614	-7.312 ± 0.0259	-9.405 ± 0.0124	-8.773 ± 0.0385
B	24802.68 ± 142.85	9861.48 ± 86.08	17493.71 ± 26.22	13588.02 ± 103.89
C	-0.3634 ± 0.0072	0.1626 ± 0.01446	-0.7408 ± 0.00199	-0.1212 ± 0.01156
D	-0.4497 ± 0.00734	-1.2163 ± 0.01433	-0.1708 ± 0.0021	-0.6130 ± 0.01146

E	0.1464 ± 0.00544	0.0669 ± 0.01161	0.1482 ± 0.00296	0.1286 ± 0.01485
R^2	0.98673	0.95318	0.99827	0.91099
χ^2	3.84547E-7	2.15533E-11	1.61114E-9	2.53478E-13

Table S34. Evaluated coefficients for correlation of the simulated IDTs for low–temperature ethane mixtures.

$0.25 \leq \varphi \leq 3.0$ $75 \leq Dilution \leq 95\%$	$1 \leq p_{5,c} \leq 50$ /atm $800 \leq T_{5,c} < 1000$ /K
A	-10.236 ± 0.0083
B	21737.98 ± 15.20
C	-0.5890 ± 3.68E-4
D	-0.0285 ± 5.16E-4
E	-0.3357 ± 6.29E-4
R^2	0.99976
χ^2	0.00408

Table S35. Evaluated coefficients for correlation of the simulated IDTs of fuel–lean ethane mixtures.

$0.25 \leq \varphi \leq 1.0$ $75 \leq Dilution \leq 95\%$	$1 \leq p_{5,c} < 18$ /atm		$18 \leq p_{5,c} \leq 50$ /atm	
	$1000 \leq T_{5,c} < 1400$ /K	$1400 \leq T_{5,c} \leq 2000$ /K	$1000 \leq T_{5,c} < 1400$ /K	$1400 \leq T_{5,c} \leq 2000$ /K
A	-12.164 ± 0.0544	-8.233 ± 0.0129	-10.137 ± 0.0101	-10.219 ± 0.0237
B	26047.966 ± 194.156	15179.79 ± 38.132	20728.66 ± 21.89	19070.91 ± 69.52
C	-0.13576 ± 0.00777	0.38121 ± 0.00355	-0.6633 ± 0.00107	0.1545 ± 0.00475
D	-0.43406 ± 0.00959	-0.97271 ± 0.0042	-0.0524 ± 0.00133	-0.6044 ± 0.00537
E	-0.12038 ± 0.00772	-0.14879 ± 0.00293	-0.1253 ± 0.00198	0.0826 ± 0.00705
R^2	0.96685	0.99179	0.99937	0.98886
χ^2	1.05E-05	3.35E-12	7.21E-09	6.15E-14

Table S36. Evaluated coefficients for correlation of the simulated IDTs of fuel–rich ethane mixtures.

$1 < \varphi \leq 3.0$ $75 \leq Dilution \leq 95\%$	$1 \leq p_{5,c} < 18$ /atm		$18 \leq p_{5,c} \leq 50$ /atm	
	$1000 \leq T_{5,c} < 1400$ /K	$1400 \leq T_{5,c} \leq 2000$ /K	$1000 \leq T_{5,c} < 1400$ /K	$1400 \leq T_{5,c} \leq 2000$ /K
A	-9.967 ± 0.0265	-8.850 ± 0.0122	-9.966 ± 0.0265	-8.850 ± 0.0122
B	21153.95 ± 60.81	18155.50 ± 26.05	21153.95 ± 60.81	18155.50 ± 26.05
C	-0.2480 ± 0.00672	-0.5261 ± 0.00326	-0.2480 ± 0.00672	-0.5261 ± 0.00326
D	-0.4038 ± 0.00643	-0.2583 ± 0.00318	-0.4038 ± 0.00643	-0.2583 ± 0.00318
E	-0.24603 ± 0.00352	-0.1361 ± 0.00284	-0.2460 ± 0.00352	-0.1361 ± 0.00284
R^2	0.99511	0.99776	0.99511	0.99776
χ^2	8.31E-07	3.20E-09	8.31E-07	3.20E-09

13 References

1. Zhou, C. W.; Li, Y.; Burke, U.; Banyon, C.; Somers, K. P.; Ding, S. T.; Khan, S.; Hargis, J. W.; Sikes, T.; Mathieu, O.; Petersen, E. L.; AlAbbad, M.; Farooq, A.; Pan, Y. S.; Zhang, Y. J.; Huang, Z. H.; Lopez, J.; Loparo, Z.; Vasu, S. S.; Curran, H. J., An experimental and chemical kinetic modeling study of 1,3-butadiene combustion: Ignition delay time and laminar flame speed measurements. *Combust Flame* **2018,** 197, 423-438.

2. Burke, S. M.; Metcalfe, W.; Herbinet, O.; Battin-Leclerc, F.; Haas, F. M.; Santner, J.; Dryer, F. L.; Curran, H. J., An experimental and modeling study of propene oxidation. Part 1: Speciation measurements in jet-stirred and flow reactors. *Combust Flame* **2014,** 161, (11), 2765-2784.
3. Li, Y.; Zhou, C. W.; Somers, K. P.; Zhang, K. W.; Curran, H. J., The oxidation of 2-butene: A high pressure ignition delay, kinetic modeling study and reactivity comparison with isobutene and 1-butene. *Proc Combust Inst* **2017,** 36, (1), 403-411.
4. Zhou, C. W.; Li, Y.; O'Connor, E.; Somers, K. P.; Thion, S.; Keesee, C.; Mathieu, O.; Petersen, E. L.; DeVerter, T. A.; Oehlschlaeger, M. A.; Kukkadapu, G.; Sung, C. J.; Alrefae, M.; Khaled, F.; Farooq, A.; Dirrenberger, P.; Glaude, P. A.; Battin-Leclerc, F.; Santner, J.; Ju, Y. G.; Held, T.; Haas, F. M.; Dryer, F. L.; Curran, H. J., A comprehensive experimental and modeling study of isobutene oxidation. *Combust Flame* **2016,** 167, 353-379.
5. Burke, U.; Metcalfe, W. K.; Burke, S. M.; Heufer, K. A.; Dagaut, P.; Curran, H. J., A detailed chemical kinetic modeling, ignition delay time and jet-stirred reactor study of methanol oxidation. *Combust Flame* **2016,** 165, 125-136.
6. Burke, S. M.; Burke, U.; Mc Donagh, R.; Mathieu, O.; Osorio, I.; Keesee, C.; Morones, A.; Petersen, E. L.; Wang, W. J.; DeVerter, T. A.; Oehlschlaeger, M. A.; Rhodes, B.; Hanson, R. K.; Davidson, D. F.; Weber, B. W.; Sung, C. J.; Santner, J.; Ju, Y. G.; Haas, F. M.; Dryer, F. L.; Volkov, E. N.; Nilsson, E. J. K.; Konnov, A. A.; Alrefae, M.; Khaled, F.; Farooq, A.; Dirrenberger, P.; Glaude, P. A.; Battin-Leclerc, F.; Curran, H. J., An experimental and modeling study of propene oxidation. Part 2: Ignition delay time and flame speed measurements. *Combust Flame* **2015,** 162, (2), 296-314.
7. Metcalfe, W. K.; Burke, S. M.; Ahmed, S. S.; Curran, H. J., A hierarchical and comparative kinetic modeling study of C_1–C_2 hydrocarbon and oxygenated fuels. *Int. J. Chem. Kinet.* **2013,** 45, (10), 638–675.
8. Keromnes, A.; Metcalfe, W. K.; Heufer, K. A.; Donohoe, N.; Das, A. K.; Sung, C. J.; Herzler, J.; Naumann, C.; Griebel, P.; Mathieu, O.; Krejci, M. C.; Petersen, E. L.; Pitz, W. J.; Curran, H. J., An experimental and detailed chemical kinetic modeling study of hydrogen and syngas mixture oxidation at elevated pressures. *Combust Flame* **2013,** 160, (6), 995-1011.
9. Bagheri, G.; Ranzi, E.; Pelucchi, M.; Parente, A.; Frassoldati, A.; Faravelli, T., Comprehensive kinetic study of combustion technologies for low environmental impact: MILD and OXY-fuel combustion of methane. *Combust Flame* **2020,** 212, 142-155.
10. Chemical-Kinetic Mechanisms for Combustion Applications. http://combustion.ucsd.edu
11. Smith, G. P.; Golden, D. M.; Frenklach, M.; Moriarty, N. W.; Eiteneer, B.; Goldenberg, M.; Bowman, C. T.; Hanson, R. K.; Song, S.; Gardiner, W. C.; Lissianski, V. V.; Qin, Z. http://www.me.berkeley.edu/gri_mech/
12. Smith, G. P.; Tao, Y.; Wang, H., Foundational Fuel Chemistry Model Version 1.0 (FFCM-1). In Stanford University, 2016.
13. Aul, C. J.; Metcalfe, W. K.; Burke, S. M.; Curran, H. J.; Petersen, E. L., Ignition and kinetic modeling of methane and ethane fuel blends with oxygen: A design of experiments approach. *Combust Flame* **2013,** 160, (7), 1153-1167.
14. Nakamura, H.; Darcy, D.; Mehl, M.; Tobin, C. J.; Metcalfe, W. K.; Pitz, W. J.; Westbrook, C. K.; Curran, H. J., An experimental and modeling study of shock tube and rapid compression machine ignition of n-butylbenzene/air mixtures. *Combust Flame* **2014,** 161, (1), 49-64.
15. Morley, C. http://www.gaseq.co.uk
16. Burke, U.; Somers, K. P.; O'Toole, P.; Zinner, C. M.; Marquet, N.; Bourque, G.; Petersen, E. L.; Metcalfe, W. K.; Serinyel, Z.; Curran, H. J., An ignition delay and kinetic modeling study of methane, dimethyl ether, and their mixtures at high pressures. *Combust Flame* **2015,** 162, (2), 315-330.
17. Ramalingam, A.; Zhang, K. W.; Dhongde, A.; Virnich, L.; Sankhla, H.; Curran, H.; Heufer, A., An RCM experimental and modeling study on CH_4 and CH_4/C_2H_6 oxidation at pressures up to 160 bar. *Fuel* **2017,** 206, 325-333.
18. Healy, D.; Curran, H. J.; Dooley, S.; Simmie, J. M.; Kalitan, D. M.; Petersen, E. L.; Bourque, G., Methane/propane mixture oxidation at high pressures and at high, intermediate and low temperatures. *Combust Flame* **2008,** 155, (3), 451-461.
19. Healy, D.; Curran, H. J.; Simmie, J. M.; Kalitan, D. M.; Zinner, C. M.; Barrett, A. B.; Petersen, E. L.; Bourque, G., Methane/ethane/propane mixture oxidation at high pressures and at high, intermediate and low temperatures. *Combust Flame* **2008,** 155, (3), 441-448.

20. Yousefian, S.; Quinlan, N. J.; Monaghan, R. F. D., Simulation of turbulent flow in a rapid compression machine: Large Eddy Simulation and computationally efficient alternatives for the design of ignition delay time experiments. *Fuel* **2018,** 234, 30-47.
21. Hemken, C.; Burke, U.; Lam, K. Y.; Davidson, D. F.; Hanson, R. K.; Heufer, K. A.; Kohse-Hoinghaus, K., Toward a better understanding of 2-butanone oxidation: Detailed species measurements and kinetic modeling. *Combust Flame* **2017,** 184, 195-207.
22. TiePie https://www.tiepie.com/en/oscilloscope-software
23. PicoScope https://www.picotech.com/downloads
24. Petersen, E. L.; Rickard, M. J. A.; Crofton, M. W.; Abbey, E. D.; Traum, M. J.; Kalitan, D. M., A facility for gas- and condensed-phase measurements behind shock waves. *Meas Sci Technol* **2005,** 16, (9), 1716-1729.
25. Weber, B. W.; Sung, C. J.; Renfro, M. W., On the uncertainty of temperature estimation in a rapid compression machine. *Combust Flame* **2015,** 162, (6), 2518-2528.
26. Pachler, R. F.; Ramalingam, A. K.; Heufer, K. A.; Winter, F., Reduction and validation of a chemical kinetic mechanism including necessity analysis and investigation of CH_4/C_3H_8 oxidation at pressures up to 120 bar using a rapid compression machine. *Fuel* **2016,** 172, 139-145.
27. Koroglu, B.; Pryor, O. M.; Lopez, J.; Nash, L.; Vasu, S. S., Shock tube ignition delay times and methane time-histories measurements during excess CO_2 diluted oxy-methane combustion. *Combust Flame* **2016,** 164, 152-163.
28. Egolfopoulos, F. N.; Zhu, D. L.; Law, C. K., Experimental and numerical determination of laminar flame speeds: Mixtures of C_2-hydrocarbons with oxygen and nitrogen. *Symposium (International) on Combustion* **1991,** 23, (1), 471-478.
29. Lowry, W.; de Vries, J.; Krejci, M.; Petersen, E.; Serinyel, Z.; Metcalfe, W.; Curran, H.; Bourque, G., Laminar Flame Speed Measurements and Modeling of Pure Alkanes and Alkane Blends at Elevated Pressures. *Proceedings of the Asme Turbo Expo 2010, Vol 2, Pts a and B* **2010**, 855-873.
30. Rozenchan, G.; Zhu, D. L.; Law, C. K.; Tse, S. D., Outward propagation, burning velocities, and chemical effects of methane flames up to 60 ATM. *Proc Combust Inst* **2003,** 29, 1461-1470.
31. Hassan, M. I.; Aung, K. T.; Faeth, G. M., Measured and predicted properties of laminar premixed methane/air flames at various pressures. *Combust Flame* **1998,** 115, (4), 539-550.
32. Vagelopoulos, C. M.; Egolfopoulos, F. N.; Law, C. K., Further considerations on the determination of laminar flame speeds with the counterflow twin-flame technique. *Symposium (International) on Combustion* **1994,** 25, (1), 1341-1347.
33. Vanmaaren, A.; Degoey, L. P. H., Stretch and the Adiabatic Burning Velocity of Methane-Air and Propane-Air Flames. *Combust Sci Technol* **1994,** 102, (1-6), 309-314.
34. Gu, X. J.; Haq, M. Z.; Lawes, M.; Woolley, R., Laminar burning velocity and Markstein lengths of methane–air mixtures. *Combust Flame* **2000,** 121, (1-2), 41-58.
35. Kochar, Y.; Vaden, S.; Lieuwen, T.; Seitzman, J., Laminar Flame Speed of Hydrocarbon Fuels with Preheat and Low Oxygen Content. In *48th AIAA Aerospace Sciences Meeting Including the New Horizons Forum and Aerospace Exposition*, AIAA: Orlando, Florida, 2010.
36. Jomaas, G.; Zheng, X. L.; Zhu, D. L.; Law, C. K., Experimental determination of counterflow ignition temperatures and laminar flame speeds of C_2–C_3 hydrocarbons at atmospheric and elevated pressures. *Proc Combust Inst* **2005,** 30, (1), 193-200.
37. Shen, X. B.; Yang, X. L.; Santner, J.; Sun, J. H.; Ju, Y. G., Experimental and kinetic studies of acetylene flames at elevated pressures. *Proc Combust Inst* **2015,** 35, 721-728.
38. Rokni, E.; Moghaddas, A.; Askari, O.; Metghalchi, H., Measurement of Laminar Burning Speeds and Investigation of Flame Stability of Acetylene (C_2H_2)/Air Mixtures. *J Energ Resour-Asme* **2015,** 137, (1).
39. Ravi, S.; Sikes, T. G.; Morones, A.; Keesee, C. L.; Petersen, E. L., Comparative study on the laminar flame speed enhancement of methane with ethane and ethylene addition. *Proc Combust Inst* **2015,** 35, 679-686.
40. Lokachari, N.; Burke, U.; Ramalingam, A.; Turner, M.; Hesse, R.; Somers, K. P.; Beeckmann, J.; Heufer, K. A.; Petersen, E. L.; Curran, H. J., New experimental insights into acetylene oxidation through novel ignition delay times, laminar burning velocities and chemical kinetic modelling. *Proc Combust Inst* **2019,** 37, (1), 583-591.
41. Hassan, M. I.; Aung, K. T.; Kwon, O. C.; Faeth, G. M., Properties of laminar premixed hydrocarbon/air flames at various pressures. *J Propul Power* **1998,** 14, (4), 479-488.

42. Kumar, K.; Mittal, G.; Sung, C.; Law, C., An experimental investigation of ethylene/O_2/diluent mixtures: Laminar flame speeds with preheat and ignition delays at high pressures. *Combust Flame* **2008,** 153, (3), 343-354.
43. Konnov, A. A.; Dyakov, I. V.; De Ruyck, J., Measurement of adiabatic burning velocity in ethane–oxygen–nitrogen and in ethane–oxygen–argon mixtures. *Exp Therm Fluid Sci* **2003,** 27, (4), 379-384.
44. Aung, K. T.; Tseng, L. K.; Ismail, M. A.; Faeth, G. M., Response to comment by S.C. Taylor and D.B. Smith on "laminar burning velocities and Markstein numbers of hydrocarbon/air flames". *Combust Flame* **1995,** 102, (4), 526-530.
45. Bosschaart, K. J.; de Goey, L. P. H., The laminar burning velocity of flames propagating in mixtures of hydrocarbons and air measured with the heat flux method. *Combust Flame* **2004,** 136, (3), 261-269.
46. Dyakov, I. V.; De Ruyck, J.; Konnov, A. A., Probe sampling measurements and modeling of nitric oxide formation in ethane plus air flames. *Fuel* **2007,** 86, (1-2), 98-105.
47. Le Cong, T.; Bedjanian, E.; Dagaut, P., Oxidation of Ethylene and Propene in the Presence of CO_2 and H_2O: Experimental and Detailed Kinetic Modeling Study. *Combust Sci Technol* **2010,** 182, (4-6), 333-349.
48. Jallais, S.; Bonneau, L.; Auzanneau, M.; Naudet, V.; Bockel-Macal, S., An experimental and kinetic study of ethene oxidation at a high equivalence ratio. *Ind Eng Chem Res* **2002,** 41, (23), 5659-5667.
49. Lopez, J. G.; Rasmussen, C. L.; Alzueta, M. U.; Gao, Y.; Marshall, P.; Glarborg, P., Experimental and kinetic modeling study of C_2H_4 oxidation at high pressure. *Proc Combust Inst* **2009,** 32, 367-375.